Ph. D. Thesis

# Study of the Symmetry-Breaking Physics at JLC

Hitoshi Murayama

Department of Physics, University of Tokyo
Bunkyo-ku, Tokyo 113, Japan

(1) ＪＬＣにおける対称性を破る物理の探究

UT-580
March, 1991

Ph. D. Thesis

# Study of the Symmetry-Breaking Physics at JLC

Hitoshi Murayama*

*Department of Physics, University of Tokyo*
*Bunkyo-ku, Tokyo 113, Japan*

*Adress after Apr., 1991: Dept. of Physics, Tohoku Univ., Sendai, 980 Japan

**Abstract**

We study various weak boson and top quark production processes at the Japan Linear Collider (JLC), a TeV $e^+e^-$ collider being planned at KEK. We evaluate the matrix elements of all the relevant processes exactly at the tree-level up to order $\alpha^4$. For this purpose, we first develope a systematic method to evaluate numerically the matrix elements of arbitrary tree-level Feynman diagrams, and we prepare an efficient parametrization of the phase space variables to deal with processes with severe $t$-channel singularities. Distributions of final state particles are discussed from the view point of the collinear singularities, and schematic figures of the typical kinematical configurations are presented for all the processes. The most dominant reaction in $e^+e^-$ collisions above 1 TeV is found to be the single weak boson production processes, $e^+e^- \to e^\pm\nu_e(\bar{\nu}_e)W^\mp$, $e^+e^-Z$ and $\nu_e\bar{\nu}_eZ$. Details of these distributions are useful as means of a possible luminosity monitoring and also as backgrounds for certain signals of the Higgs boson if its mass is around the weak boson masses. Effect of the Higgs boson exchange in the final states $W^+W^-Z$ and $ZZZ$ is found to be significant only when its production and decay into a weak boson pair are both kinematically allowed. The S/N ratio can be improved substantially by introducing a longitudinally polarized electron beam. The final state $t\bar{t}Z$ is affected little by the Higgs boson and its Yukawa coupling to the top quark. The detection of the top quark Yukawa coupling requires not only the "lucky" situation $2m_t < m_H < \sqrt{s} - m_Z$ but also the measurement of the top quark helicities. The $W$-fusion production of the Higgs boson leads to a large effect in the final states $\nu_e\bar{\nu}_eW^+W^-$, $\nu_e\bar{\nu}_eZZ$ and $\nu_e\bar{\nu}_et\bar{t}$. The effects of virtual Higgs boson exchanges can be significant in these reactions, which may allow us to study symmetry breaking physics in a more general ground. The process $e^+e^- \to e^\pm\nu_e(\bar{\nu}_e)W^\mp Z$ gives rise to a serious background to the final states $\nu_e\bar{\nu}_eW^+W^-$ and $\nu_e\bar{\nu}_eZZ$, whose total cross section is roughly three-times as that of $\nu_e\bar{\nu}_eW^+W^-$ in the worst case. However we can expect to remove it in the hadronic decay modes by distinguishing $Z$- from $W$-boson in the di-jet invariant mass spectrum.

# Contents

# Chapter 1

# Introduction

Feasibility of an $e^+e^-$ linear collider reaching the energy region of TeV has been discussed seriously in recent years [1,2,3]. Though there are projects of super $pp$ colliders (LHC and SSC) which can reach several tens of TeV, the importance of a TeV $e^+e^-$ collider has been repeatedly emphasized, especially because of its cleaner environment. Furthermore, there is a general expectation that an $e^+e^-$ collider at the c.m. energy 1–2 TeV is promising enough to compete with or even supercede the capabilities of the super $pp$ colliders. Although it has been pointed out that the advantage of a clean environment at $e^+e^-$ colliders will diminish at very high energies due to the beamstrahlung effect, the studies in Refs. [1–4] have shown that the effect does not destroy the advantage of the $e^+e^-$ colliders, which will still be able to provide us with high precision measurements.

In Japan, there has been serious studies on the physics capability of an $e^+e^-$ linear collider JLC (the Japan Linear Collider) [3,4], which has been considered as a future high energy project at KEK (National Laboratory for High Energy Physics, Tsukuba). According to the recent study [4], JLC is aiming at three phases of the colliding $e^+e^-$ energies, 0.5 TeV (JLC-I), 1 TeV (JLC-II) and 1.5 TeV (JLC-III) with the luminosity $3\text{–}6\times10^{33}\text{cm}^{-2}\text{s}^{-1}$. These parameters are based mainly on the feasibility studies of the accelerator physics, and no serious studies on the particle physics requirements for the collider parameters have been presented so far. In fact, we found that even the tree-level cross sections of the most important processes at TeV $e^+e^-$ colliders are not known, without which no serious study of the physics capability of such a collider is possible.

In this paper, we develope a technique to evaluate cross sections of all the relevant reactions exactly in the tree-level, and present distributions of all the relevant processes up to order $\alpha^4$. We believe that the exact cross sections of all the following processes are new: $e^+e^- \to e^\pm\nu_e(\bar{\nu}_e)W^\mp$, $e^+e^-Z$, $\nu_e\bar{\nu}_e Z$ (Chap. 4), $t\bar{t}Z$ (Chap. 6), $\nu_e\bar{\nu}_e ZZ$, $\nu_e\bar{\nu}_e t\bar{t}$, $e^+e^-t\bar{t}$, $e^+e^-ZZ$, $e^\pm\nu_e(\bar{\nu}_e)W^\mp Z$ (Chap. 7). We present for completeness discussions of all the essential processes of order $\alpha^2$, $\alpha^3$ and $\alpha^4$, at a TeV $e^+e^-$ collider. When presenting distributions, we chose the proposed JLC energies, 0.5 TeV, 1 TeV or 1.5 TeV. However, the contents of this report should be useful for the studies of any $e^+e^-$ colliders at the TeV energy range.

In order to discuss physics capability of future $e^+e^-$ linear colliders, we should first

consider what kinds of physics are expected at TeV energies.

## 1.1 Very Quick Review of Particle Physics Today

In this section, we review the most essential part of our present knowledge on the physics of elementary particles *very* quickly.

We know that there are four vector bosons which transmit interactions among leptons and quarks:

$$\gamma,\ Z,\ W^{\pm}, g. \tag{1.1}$$

The gluon $g$ mediate the strong QCD interaction which confines the quarks inside the hadrons at its long wave-length. The photon $\gamma$ mediate the electro-magnetic interaction, whose theory (QED) is surprizingly successful in describing the anomalous magnetic moment of the electron or muon [5]. Both QCD and QED possess gauge invariance, which ensures the universality of the coupling between the vector boson and the fermion fields.

We further know that $W$- and $Z$-bosons as well satisfy a high degree of universality of the coupling with the fermion fields. We quote a quantity shown by Sirlin [6]

$$|V_{ud}|^2 + |V_{us}|^2 + |V_{ub}|^2 = 0.9970 \pm 0.0016, \tag{1.2}$$

where the error comes mostly from the complexity of the nuclear physics. The remarkable agreement of the above quantitiy with *unity* shows that the charged current coupling between the $W^{\pm}$-boson and the fermion fields are highly universal both in lepton and quark sector.

This is the end of our very quick review.

## 1.2 Physics Behind the Universality

We, at present, can think of only *two* possiblities to explain the high degree of universality mentioned in the previous section.

The first one is the $SU(2)_L \times U(1)_Y$ gauge symmetry, like that of QED and QCD. The gauge symmetry, however, should be broken since the vector bosons $W^{\pm}$ and $Z$ are massive. Some dynamics is necesary to generate the order parameter,[1] where the dynamics has not been experimentally accessible so far. In fact, all the mass terms of quarks, leptons, $W^{\pm}$-bosons and $Z$-boson are prohibited by the gauge symmetry. These masses will be generated by coupling the fields to the order parameter of the symmetry-breaking.

The second one is the compositeness, where the quarks, leptons and the vector bosons have the same constituents, or *preons*, and their coupling can be universal in analogy to the idea of the vector meson dominance in low-energy dynamics of the hadrons. The

[1] We generically call the vacuum condensate of some operator which breaks $SU(2)_L \times U(1)_Y$ symmetry as 'order parameter'.



preons should be confined[2] inside the quark/lepton/vector particles due to some unknown dynamics. All the masses should be explained by this unknown dynamics.

Let us discuss what kind of the signals of the physics behind the universality may appear at TeV $e^+e^-$ linear colliders for the two scenarios separately.

### 1.2.1 $SU(2)_L \times U(1)_Y$ Gauge Theory

The gauge theory forces us to start with strictly massless vector bosons, since their mass terms are forbidden due to the gauge invariance. However, we know that $W^{\pm}$- and $Z$-bosons are massive. The only mechanism which can give masses to the gauge bosons is the Higgs mechanism.

We assume that the $SU(2)_L \times U(1)_Y$ symmetry will be broken down to $U(1)_{\rm QED}$, with some order pararmeter, where the symmetry breaking of the continuous symmetry will produce massless Goldstone bosons. Here the number of the generators is reduced from four to one, thus there will be three Goldstone bosons. The Goldstone bosons can fully mix with the gauge bosons since they are both massless, and the mixing produces three *massive* vector bosons. The mass scale comes from that of the order parameter of the symmetry-breaking. Since all the masses of quarks, leptons, $W^{\pm}$ and $Z$ bosons are generated from coupling of these fields to the order parameter, the heavier particles couple stronger to the order parameter, hence more sensitive to the physics of symmetry-breaking.

There are two scenarios how the Higgs mechanism is operating. Hereafter we call the particles and interactions which generate the order parameter generically as "Higgs sector".

#### Weakly Coupled Higgs Sector

The order parameter arises from the self-interaction of the seemingly elementary scalar particle, where its potential has the minimum where the scalar field has non-zero value. Thus the potential should have the famous "wine-bottle" shape, and the scalar field condenses in the vacuum to have non-zero vacuum expectation value. This vacuum expectation value of the scalar field $v$ is the order parameter of the symmetry-breaking, and has a dimension of mass. The shape of the potential allows the "radial" fluctuations around the vacuum with the broken symmetry. This "radial" mode, often referred to as Higgs boson, acquires mass from the curvature of the potential near the minimum, which means that the mass of the Higgs boson is a measure how strongly it couples with itself due to the $\phi^4$ potential. If we call the self-coupling constant $\lambda$, there will be the relation

$$m_H^2 \sim \lambda v^2, \tag{1.3}$$

where the precise normalization is fixed once we write down the explicit form of the potential. Thus the heavy Higgs boson means that the coupling with itself is strong.

In the scenario of the weakly coupled Higgs sector, we assume that the perturbation theory is good, just like in QED and QCD at hard processes. The weakness of the coupling

[2] Here we do not use the word 'confine' in its strict sense as in QCD. We merely mean that the preons are still not liberated at the low-energy experiments.

leads to light Higgs boson from the above discussion. The validity of the perturbation theory will break down if the higher order terms are comparable to the lowest order term. If the prediction of the lowest order calculation is near to the unitarity limit on the $S$-matrix, then we know that the higher order terms should be comparable to the lowest order one to ensure the unitarity of the $S$-matrix at the full order. Thus the requirement of the 'good' perturbative expansion prohibit the lowest order prediction to be near the unitarity limit. One may require that the lowest order amplitude on the vector boson scattering processes does not exceed the limit

$$-\frac{1}{2} < \mathrm{Re}\mathcal{A} < \frac{1}{2}, \tag{1.4}$$

where $\mathcal{A}$ is a partial wave amplitude, which leads to a limit on the mass of the Higgs boson [7]

$$m_H \leq 780\mathrm{GeV}. \tag{1.5}$$

The most important aspect of the mass of the Higgs boson is that it tells us the scale of new physics. Since the scalar self-coupling is asymptotic non-free, the coupling constant will blow up at some scale if we follow the renormalization group flow. One can draw the conclusion that there should appear new particles or new interactions *before* we reach the scale where the scalar self-coupling will blow up. For example, if we find the mass of the Higgs boson to be around 400 GeV, then we will know that there should be an 'intermediate' scale between the weak scale and the Planck scale. If we find the mass of the Higgs boson lighter than 200 GeV or so, the blow up of the scalar self-coupling will not occur below the Planck scale, which may lead to an exciting possibility that our $SU(3)_{\mathrm{QCD}} \times SU(2)_L \times U(1)_Y$ gauge theory will remain to be valid up to the Planck scale! In fact, supergravity models with only doublet and singlet Higgses predict that the lightest Higgs boson should be lighter than 150 GeV [8].

### Strongly Coupled Higgs Sector

We assume that the breakdown of the $SU(2)_L \times U(1)_Y$ symmetry occurs *dynamically*. Since the dynamical breakdown of the symmetry is a non-perturbative effect, we need some strong interaction. The scenario is based on the analogy with the BCS theory of superconductivity, whose idea is introduced to the field theory by Nambu and Jona-Lasinio [9]. Here, the strong interaction causes condensation of the particles, which breaks the symmetry. The 'radial' mode will not be necessarily present. The Higgs bosons need not exist in general. A well-known model along this scenario is the technicolor model [10], though it has not been phenomenologically successful so far.

In this scenario, we expect that the coupling between the quanta of the Higgs sector is non-perturbative. Since the longitudinal components of the $W^{\pm}$- and $Z$-bosons originate from the Goldstone bosons of the Higgs sector, we can expect non-perturbative couplings between them. Furthermore, top quark is now known to be heavier than 90 GeV [11], and we expect that top quark is as sensitive to the physics of the symmetry breaking as the $W^{\pm}$- or $Z$-bosons. Thus we will be able to draw information on the strongly coupled Higgs



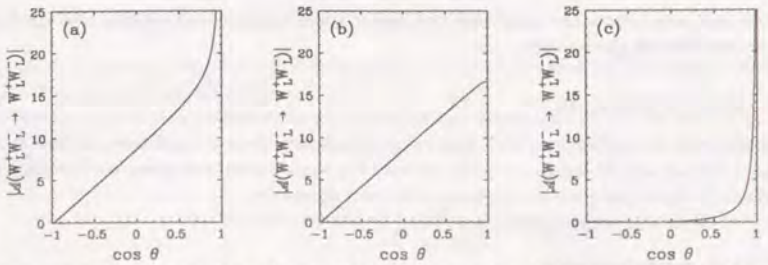


Figure 1.1: The angular dependence of the absolute value of the amplitude for the process $W_L^+W_L^- \to W_L^+W_L^-$, at c.m. energy 1 TeV. (a) Without the Higgs exchange amplitudes. (b) The Higgs exchange amplitudes with $m_H = 100$ GeV. (c) Total amplitude with Higgs exchange.

sector by investigating the couplings between

$$W^{\pm},\ Z,\ t. \tag{1.6}$$

Note that we know the energy scale where they start to couple non-perturbatively. Recall the discussion on the mass of the Higgs boson from the lowest order amplitude. We know if the lowest order prediction of the amplitude approach the bound from the unitarity like (1.4), the interaction will be non-perturbative. Thus, we can estimate the scale where the non-perturbative nature will show itself in the couplings between the three particles above in the absence of the Higgs bosons. The authors of Ref. [7] give the value $m_{WW} = 1.2$ TeV where the non-perturbative nature of their interaction will appear.

One important remark is that we can prove this scenario without establishing the non-perturbative nature directly. If we know that the gauge invariance is present, and if we further know that there is no Higgs boson at all, we can conclude that the Higgs sector breaks the symmetry *without* producing the Higgs boson. Then we know that the Higgs sector is indeed strongly coupled. To demonstrate this point, we show the absolute value of the amplitude for the $W$-boson scattering $W^+W^- \to W^+W^-$ in Fig. 1.1 at $m_{WW} = 1$ TeV. Here all the $W$-bosons are taken to be longitudinally polarized. The Fig. 1.1(a) shows the amplitude without the Higgs boson exchange. The forward peak is the Coulomb pole due to the $t$-channel photon exchange solely from the low-energy physics, hence not our concern. One observes large contribution of the $J = 0$ and $J = 1$ partial waves like $1 + \cos\theta$, which actually grow like $G_F s$ at high enough energy. This part will violate the unitarity limit (1.4) above 1.2 TeV. However, if there exists a light Higgs boson, the amplitudes of the Higgs boson exchange cancel this part completely. The Fig. 1.1(b) shows the amplitude of the Higgs boson exchange, which behaves as $1 + \cos\theta$ just like that of Fig. 1.1(a). This amplitude has in fact the different sign as the non-Higgs amplitude which will cancel each other. The Fig. 1.1(c) shows the amplitude after cancellation, where only the forward peak is left. Thus, the *absence* of the Higgs boson is directly related to the *increasing* lowest-order

amplitude, and somewhere the amplitudes of higher order or some new interactions should appear as we increase the energy.

### 1.2.2 Compositeness

Another scenario to explain the high degree of universality is to assume quarks, leptons, $W^{\pm}$- and $Z$-bosons are all composite particles with the same constituent preons. The preons are confined in these particles due to some unknown dynamics.

The models in this scenario are constrained by the conditions:

1. $U(1)_{\rm QED}$ gauge invariance,
2. $SU(2)$ (?) global symmetry,
3. single pole dominance at low-energy.

From the conditions 2. and 3., the $ff'V$ vertex will satisfy universality at low energy (here we are talking about "low" energy compared to the multi-TeV scale). Furthermore, the following constraint should be imoposed on the scenario:

4. approximate unbroken chiral symmetry,

to ensure the "lightness" of the fermions compared to the scale of compositeness, and the (almost) massless fermions must satisfy the anomaly matching condition [12]. One interesting model which satisfies these constraints is the "strongly coupled Standard Model" [13] where one should assume that the $SU(2)$ gauge theory has the confining, though chirality conserving phase.

We expect the deviation from the $SU(2)_L \times U(1)_Y$ gauge theory at high energy. Recall that in the Yang-Mills theory, the coupling between the gauge bosons is completely fixed from the gauge invariance and renormalizability as that in the three-vector boson vertex shown in App. A. In particular, the vertex is totally antisymmetric under the exchange of the three vector bosons which is the consequence of the anti-symmetry of the structure constant in the compact Lie algebra. However in the composite scenario, the only gauge boson is photon, and neither $SU(2)_L \times U(1)_Y$ gauge invariance nor the renormalizability are imposed. We cannot talk about the "symmetry" between photon and other "vector mesons" since they are completely different objects. Thus we expect that there will be substantial deviation of the three vector boson coupling from the Yang-Mills ones. For example, we expect the interactions like

$$\mathcal{L}_{\rm eff} \sim \Delta\kappa W^+_\mu W^-_\nu F^{\mu\nu} + \frac{\lambda}{m_W^2} W^{+\nu}_\mu W^{-\rho}_\nu F_\rho{}^\mu + \cdots \tag{1.7}$$

in the $W^+W^-\gamma$ vertex. Once we find anomalous couplings between the vector bosons or form factor suppression, we will acquire a very important clue, *i.e.*, the scale where the composite dynamics will show itself.



## 1.3 Where to look for?

To prove or disprove the scenarios discussed in the previuos section, it is quite clear what kind of processes should be studied.

If the gauge theory describes the real world, Higgs mechanism should be operating. Thus the search for the Higgs boson is the most urgent task. The search for the Higgs boson can be made at the processes

$$\begin{aligned} e^+e^- &\to ZH, && (1.8)\\ &\to \nu_e\bar{\nu}_e H, && (1.9)\\ &\to e^+e^- H, && (1.10) \end{aligned}$$

which are the main concern of this paper.

If the Higgs boson is lighter than twice the $W$-boson mass, it decays mainly into $b\bar{b}$ with very narrow width. However if it is heavier, it will decay mainly into $W^+W^-$, $ZZ$ or $t\bar{t}$. Then the Higgs boson may have very large width compared to its mass; the Higgs boson in the minimal Standard Model of mass $m_H = 600$ GeV has a width $\Gamma_H = 100$ GeV, where the ratio $\Gamma_H/m_H$ is already as large as that of $\rho$-meson! Thus the production processes of the relatively heavy Higgs boson should be discussed including its decay.

Then the processes we should study will be

$$\begin{aligned} e^+e^- &\to W^+W^-Z, && (1.11)\\ &\to ZZZ, && (1.12)\\ &\to t\bar{t}Z, && (1.13) \end{aligned}$$

for the process (1.8),

$$\begin{aligned} e^+e^- &\to \nu_e\bar{\nu}_e W^+W^-, && (1.14)\\ &\to \nu_e\bar{\nu}_e ZZ, && (1.15)\\ &\to \nu_e\bar{\nu}_e t\bar{t}, && (1.16) \end{aligned}$$

for the process (1.9), and

$$\begin{aligned} e^+e^- &\to e^+e^- W^+W^-, && (1.17)\\ &\to e^+e^- ZZ, && (1.18)\\ &\to e^+e^- t\bar{t}, && (1.19) \end{aligned}$$

for the process (1.10).

If the gauge theory is correct though there is no Higgs boson, or in other words the Higgs sector is strongly coupled, then we should disprove the existence of any Higgs boson and study the vector boson scattering processes. Their scattering can be studied in the same processes as that of the Higgs search, and additionally at

$$e^+e^- \to e^\pm\nu_e(\bar{\nu}_e)W^\mp Z. \tag{1.20}$$

If the composite scenario is the correct one, then we should measure the couplings between the vector bosons in the processes

$$e^+e^- \rightarrow W^+W^-, \tag{1.21}$$
$$\rightarrow e^\pm\nu_e(\bar{\nu}_e)W^\mp, \tag{1.22}$$
$$\rightarrow \nu_e\bar{\nu}_eZ. \tag{1.23}$$

Thus in all scenarios, what we should study are the the processes where the $W$-, $Z$-bosons or the top quark are produced.

## 1.4 Organization of the Paper

The aim of this paper is to study the processes which are relevant for the study discussed in the previous section. Though the systematic study is required to discuss the signal as well as the backgrounds, even the total cross sections have not been known for most of the processes so far. Therefore what is required at present is *not* the detailed study of cuts and detector simulations. We should *understand* these processes first. The total cross sections and qualitative understanding of the distributions are of the first priority to be discussed. No study including the event generation is made in this paper.

We categorized the processes into several classes, and discuss them separately in the later chapters. For the purpose, we need a systematic method to evaluate all the differential distributions for many processes. We first present our method we used in our study in Chap. 2.

The first class we discuss includes the processes where the final state is two-body.[3] They are discussed in the Chap. 3. Though these processes are already well-understood, we try to explain their distributions from the view point of the collinear singularity. This view point proves to be effective in understanding the processes of later chapters.

Though the two-body production processes have been the most dominant ones at the $e^+e^-$ colliders, they cease to be dominant at sub-TeV energy where the single $W/Z$ production processes will have much larger cross section. Chap. 4 discusses this class of processes, where the main interests in them are that they can be important backgrounds due to their large cross sections. However, they serve a useful place to acquire intuitions on the distributions, since all types of the collinear singularities except the two-photon type one appear in these processes, and we discuss them in detail.

We discuss the Higgs production processes in Chap. 5 with the zero-width approximation for the Higgs boson. Though the discussions in this chapter should be regarded as qualitative one due to the approximation, it will be useful to understand the typical distributions of the Higgs production.

We study in Chap. 6 the processes where the Higgs boson exchange is present like in $ZH$ production. Thus the processes necessarily include the $Z$-boson in the final state. Here we discuss various cuts to make the Higgs boson signal clearer. The role of the longitudinal

[3]We do not consider the decays of $W$- and $Z$-bosons throughout this paper, to make physics clearer.



polarization in the electron beam is shown to be important in the studies of relatively heavy Higgs boson.

The processes relevant to the search for the Higgs boson via (1.9) or (1.10) are discussed in Chap. 7. The total cross sections of all processes are presented. The discussions are not as thorough as the ones in the other chapters, though we believe they are already worth to include. Chap. 8. is devoted to conclusions.

The appendices deal with some technicalities. App. A describes briefly the method we used to evaluate the helicity amplitudes, which is summarized in the HELAS system. The phase space integrations are done with the variables defined in App. B. An interesting selection rule for helicity of the final state vector boson is discussed in App. C which was found empirically while studying the various processes.

# Chapter 2

# Method

One of the reasons that systematic study on the physics at linear $e^+e^-$ collider has been minor so far is that there is no systematic method to obtain the cross sections and the distributions of the multi-body processes. In particular, the singularities appearing in the processes with the $t$-channel photon exchange should be treated very carefully. The effective particle approximations are quite useful to avoid this problem. They are however sometimes mis-used in the literature, where small-$p_T$ distributions are not given correctly. Furthermore, the collinear approximation fails to deal with the high-$p_T$ tails of the photon exchange, which will be essential in dealing with the single weak boson production processes as backgrounds of the Higgs hunting.

We describe briefly the methods we used in this paper. More details are presented in the appendices. The aim of this chapter is to present the rough idea of our methods.

## 2.1 Helicity Amplitudes

The most conventional way to obtain the cross sections and distributions has been to use the trace technique [14]. The advantage of the technique is two-fold. First, it proceeds in a manifestly Lorentz invariant way. We fix the frame only after obtaining the spin-summed invariant amplitudes. Second, it is completely free of convention, in the sense that we do not have to specify whether we work in the Pauli-Dirac representation, Majorana-representation or Weyl-representation of the Clifford algebra.

Despite the advantages, it is not as useful as it has been for the processes we discuss in this paper. The reason is that the number of the Feynman diagrams grows very fast as the number of the final state particles increases, and the traces we have to take grow like the *square* of the number of the diagrams. For example, in the process $e^+e^- \to \nu_e\bar{\nu}_e W^+W^-$, there are 28 Feynman diagrams for the $t$-channel type alone in the lowest order, and therefore $28\cdot(28+1)/2 = 406$ independent traces. In the process $e^+e^- \to e^+e^-W^+W^-$ which is known as the *two-photon* background to the above process, there are 49 Feynman diagrams, giving 1225 independent traces. It is clear from these examples that we cannot proceed in this way.



Since the number of the digrams grow rapidly, it will be much better to compute the *amplitudes* directly as complex numbers, and simply sum them up to give the total amplitudes. Then we have to sum only 28 complex numbers for $e^+e^- \to \nu_e\bar{\nu}_e W^+W^-$, and 49 complex numbers for $e^+e^- \to e^+e^-W^+W^-$. To compute the amplitudes, however, we need to fix the spin states of the external lines, often taken to be the helicity eigenstates. Thus we are led to discuss the helicity amplitudes.

There is another advantage of the helicity amplitudes in electroweak physics. Since the $V-A$ interaction distinguishes the negative helicity particles from the positive one, the different helicity states behave quite differently in the real physics. For example, though it seems first that we have $2\times2\times3\times3$ different helicity combinations in the process $e^+e^- \to \nu_e\bar{\nu}_e W^+W^-$, the positive helicity electron and the negative helicity positron do not contribute at all due to the $V-A$ interaction, and we are left with only 9 different helicity combinations. Even for $e^+e^- \to e^+e^-W^+W^-$, 20 diagrams drop due to the $V-A$ interaction for the positive chirality sector.

Though the Lorentz invariance is not explicit in the course of computation, it is still an advantage, since it supplies a very non-trivial method to check the final results.

To describe our method to evaluate helicity amplitudes, let us discuss the single weak boson production processes as examples. We show in Figs. 2.1(a) to (c) Feynman diagrams for the processes

$$e^-e^+ \to e^-\bar{\nu}W^+, \tag{2.1}$$

$$\to e^-e^+Z, \tag{2.2}$$

$$\to \nu_e\bar{\nu}_eZ, \tag{2.3}$$

respectively. The three processes have both $e^+e^-$ annihilation (diagrams s1 to s5 in Fig. 2.1) and $t$-channel vector boson exchange (diagrams t1 to t5 in Fig. 2.1) contributions. The annihilation contributions, part of which can be expressed as the production of vector boson pairs ($W^+W^-$, $ZZ$ and $\gamma^*Z$) and their subsequent decays into leptons ($W^- \to e^-\bar{\nu}$, $Z \to e^-e^+$, $\nu_e\bar{\nu}_e$ and $\gamma^* \to e^-e^+$), give cross sections which decrease as $1/s$, with $\sqrt{s}$ being the center of mass energy of the colliding $e^+e^-$ system. On the other hand, the non-annihilation contributions with $t$-channel vector boson exchange give rise to cross sections which do not decrease with rising beam energies and they dominate the single weak boson production processes at asymptotic energies. Interference effects between the annihilation and the non-annihilation amplitudes are expected to be relevant only below the vector boson pair production threshold.

The diagrams listed in Fig. 2.1 suggest that all the amplitudes can be evaluated in terms of a few common subamplitudes. We follow the basic technique [15,16] of evaluating helicity amplitudes numerically. In this paper, we present a generalization of the subamplitudes and the crossing relations that were introduced in Ref. [16], which systematize the evaluation of arbitrary tree amplitudes with massive fermions and nonconserved currents. We first present the complete helicity amplitudes keeping all the external and internal fermion masses finite, and then explain the simplification which can be made to evaluate cross sections up to corrections of order $m_e^2/s$. The exact expressions are found to be no more complicated

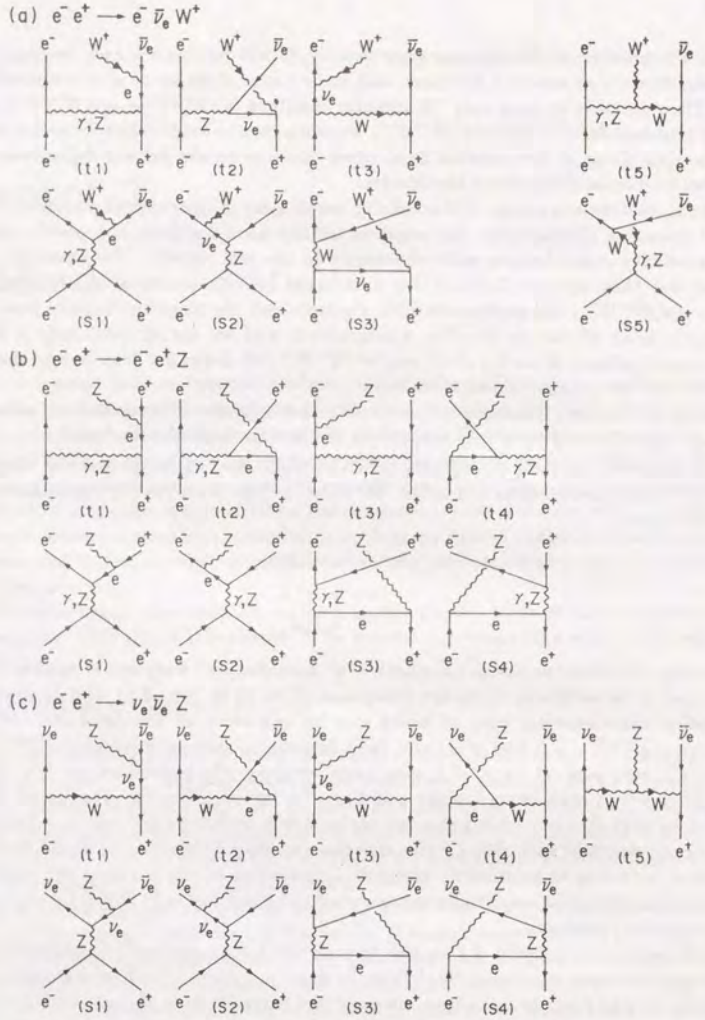


Figure 2.1: Feynman diagrams of the single weak boson production processes. (a) $e^+e^- \to e^-\bar{\nu}_e W^+$, (b) $e^+e^- \to e^+e^- Z$, (c) $e^+e^- \to \nu_e\bar{\nu}_e Z$.



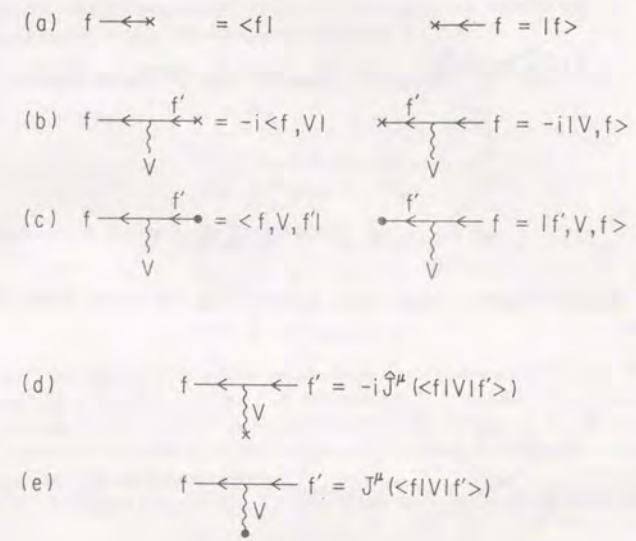














Figure 2.2: HELAS Feynman rules. Basic subamplitudes for the $FF \to V$ and $FV \to F$ vertices

than the corresponding massless expressions, the only practical difference being twice the computing time needed for their evaluation, and we introduce a notation which allows straightforward replacements of the subamplitudes with massless fermions and those with massive fermions. The exact amplitudes can be used for testing the order $m_e^2/s$ contributions or with a suitable modification, for associated production of a heavy fermion pair and a weak boson.

In Figs. 2.2, 2.3 and 2.4 we show the basic subamplitudes in terms of which all the amplitudes discussed in this paper can be obtained. All we need is to express these subamplitudes in terms of the external particle four-momenta and helicities in a closed form. Our notations for fermion and vector boson wave functions and for the subamplitudes of Figs. 2.2, 2.3 and 2.4 are summarized in Appendix A.

In the framework Ref. [17], the HELAS basis, helicity amplitudes for an arbitrary tree diagram are calculated as follows. First, all the external wave functions of fermions and vector bosons are calculated in terms of their four-momenta and helicties, according to the convention of Refs. [15,16]. Second, these external lines (either scalar, spinor or vector lines) are combined with a basic vertex of the theory to give an off-shell line. These off-shell

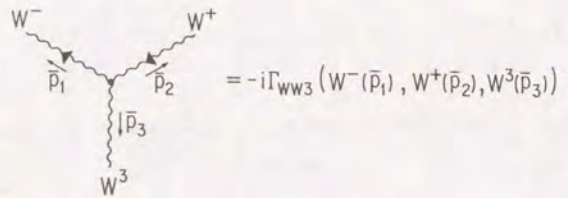


Figure 2.3: HELAS Feynman rule. Basic subamplitude for vector boson three-point self-coupling.

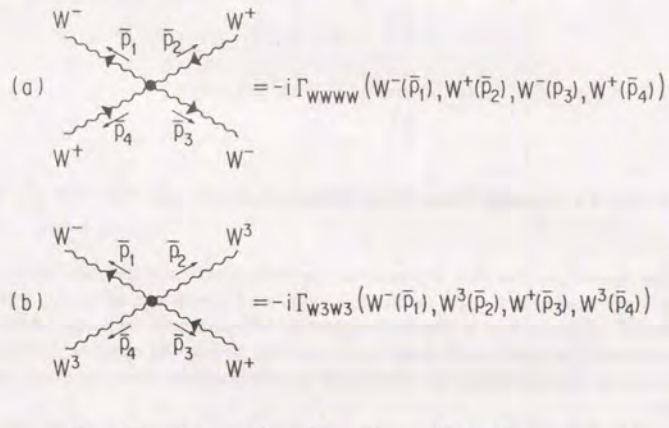


Figure 2.4: HELAS Feynman rules. Basic subamplitudes for vector boson four-point self-couplings. The vertex includes the four-point contact diagram as well as the vector boson exchange diagram via two three-point vertices. (a) Vertex of four $W^{\pm}$-bosons. (b) Vertex of two $W^{\pm}$-bosons and two $W^3$-bosons.



lines can again be combined by another vertex to make a new off-shell line. This process ends when all the off-shell lines meet, and we obtain a complex number for the amplitude.

We show examples of the procedure in the process

$$e^-(k_1,\sigma_1) + e^+(k_2,\sigma_2) \to e^-(p_1,\lambda_1) + \bar{\nu}_e(p_2,\lambda_2) + W^+(p_W,\lambda_W). \tag{2.4}$$

We have two initial spinors

$$\begin{aligned} |e_1\rangle &= |e(k_1,\sigma_1,+)\rangle_\alpha, \\ \langle e_2| &= \langle e(k_2,\sigma_2,-)|_\alpha, \end{aligned} \tag{2.5}$$

and two spinors and a vector in the final states

$$\begin{aligned} \langle e_3| &= \langle e(p_1,\lambda_1,+)|_\alpha \\ |\nu_4\rangle &= |\nu_e(p_2,\lambda_2,-)\rangle_\alpha, \\ W^\mu &= \bar{\epsilon}^\mu(p_W,\lambda_W,+). \end{aligned} \tag{2.6}$$

The spinor and the polarization vector conventions are summarized in App. A. The sign factors distinguish a particle (+) from an antiparticle (−) in case of a fermion, and an outgoing (+) from an incoming (−) particle in case of a vector boson. Each spinor consists of two Weyl spinors with different chiralities ($\alpha = \pm 1$). Hence, both spinor and vector wave functions have four complex components.

The HELAS Feynman rules of Fig. 2.2 then allow us to make an off-shell fermion line

$$|e, W, \nu_4\rangle, \tag{2.7}$$

and off-shell vector lines

$$J^\mu(\langle e_3|A|e_1\rangle),\ \ J^\mu(\langle e_3|Z|e_1\rangle), \tag{2.8}$$

that appear in the diagram (t1) of Fig. 2.1a. These off-shell lines are evaluated numerically by eqs. (A21) and (A.26) of the Appendix A. They can again be used as inputs of the HELAS Feynman rules in Fig. 2.2. For example, the off-shell spinor (2.7) and the initial positron spinor $\langle e_2|$ of (2.5) can be combined by the rule Fig. 2.2d to make off-shell vector lines

$$\hat{J}^\mu(\langle e_2|A|e, W, \nu_4\rangle),\ \ \hat{J}^\mu(\langle e_2|Z|e, W, \nu_4\rangle). \tag{2.9}$$

A truncated off-shell vector line ($\hat{J}$) is chosen simply to avoid a double counting of the vector boson propagator factor in the amplitude (t1) of Fig. 2.1a,

$$-\sum_{V=\gamma,Z} J(\langle e_3|V|e_1\rangle)\cdot\hat{J}(\langle e_2|V|e, W, \nu_4\rangle), \tag{2.10}$$

which is simply made of contractions of the off-shell vector currents, (2.8) and (2.9). The diagrams (t2), (t3), and (s1) to (s3) have a similar structure.

In order to evaluate the diagrams (t5) and (s5) with the three weak boson couplings, we find it convenient to introduce the $W^3$ current such as

$$J^\mu(\langle e_3|W^3|e_1\rangle) = \cos\theta_W J^\mu(\langle e_3|Z|e_1\rangle) + \sin\theta_W J^\mu(\langle e_3|A|e_1\rangle). \tag{2.11}$$

The diagram of (t5) is then simply expressed as

$$-\Gamma_{WW3}\left(J(\langle e_2|W|\nu_4\rangle),W,J(\langle e_3|W^3|e_1\rangle)\right), \tag{2.12}$$

according to the HELAS Feynman rule of Fig. 2.3, with eqs. (A.34), (A.35) of the Appendix A.

With these preparation, it is straightforward to express the amplitudes that are listed in Figs. 2.1a, b, c. The helicity amplitudes for the process $e^-e^+ \to e^-\bar{\nu}_e W^+$ (Fig. 2.1a) are expressed as

$$M(e^-e^+ \to e^-\bar{\nu}_e W^+) = M_{NA} - M_A \tag{2.13}$$

where the amplitudes are splitted into two classes, one with the initial $e^-e^+$ annihilation depicted as $M_A$ ($s$-channel $\gamma$ or $Z$ exchange diagrams (s1) to (s3) and (s5) of Fig. 2.1a) and the other depicted as $M_{NA}$ without annihilation (diagrams (t1) to (t3) and (t5) with $t$-channel $\gamma$, $Z$ or $W$ exchange in Fig. 2.1a). They are expressed as

$$\begin{aligned} M_{NA} = & \sum_{V=\gamma,Z} J(\langle e_3|V|e_1\rangle)\cdot\hat{J}(\langle e_2|V|e,W,\nu_4\rangle) \\ & + J(\langle e_3|Z|e_1\rangle)\cdot\hat{J}(\langle e_2,W,\nu,|Z|\nu_4\rangle) \\ & + J(\langle e_2|W|\nu_4\rangle)\cdot\hat{J}(\langle e_3|W|\nu,W,e_1\rangle) \\ & + \Gamma_{WW3}\left(J(\langle e_2|W|\nu_4\rangle),W,J(\langle e_3|W^3|e_1\rangle)\right), \end{aligned} \tag{2.14}$$

$$\begin{aligned} M_A = & \sum_{V=\gamma,Z} J(\langle e_2|V|e_1,\rangle)\cdot\hat{J}(\langle e_3|V|e,W,\nu_4\rangle) \\ & + J(\langle e_2|Z|e_1\rangle)\cdot\hat{J}(\langle e_3,W,\nu|Z|e_2\rangle) \\ & + J(\langle e_3|W|\nu_4\rangle)\cdot\hat{J}(\langle e_2,W,\nu|W|e_1\rangle) \\ & + \Gamma_{WW3}\left(J(\langle e_2|W|\nu_4\rangle),W,J(\langle e_2|W^3|e_1\rangle)\right). \end{aligned} \tag{2.15}$$

A direct application of the HELAS Feynman rules Figs. 2.2 and 2.3 gives $i$ times the transition amplitude $M$. The relative sign factor between $M_{NA}$ and $M_A$ is due to the anti-commutation of the fermion operators, which should be fixed by hand.

Helicity amplitudes for the $CP$ conjugate process $e^+e^- \to e^+\nu_e W^-$ are obtained similarly. Under $CP$ invariance, helicity amplitudes of $CP$-conjugated processes differ only by an overall phase. For example, the identity

$$\begin{aligned} & \left|M(e^-(k_1,\sigma_1),e^+(k_2,\sigma_2),e^-(k_3,\sigma_3),\bar{\nu}(k_4,\sigma_4),W^+(q,\lambda))\right| \\ & = \left|M(e^-(k_1,-\sigma_2),e^+(k_2,-\sigma_1),e^+(\tilde{k}_3,-\sigma_3),\nu(\tilde{k}_4,-\sigma_4),W^-(\tilde{q},-\lambda)\right| \end{aligned} \tag{2.16}$$

holds under $CP$ invariance, where $\tilde{p} = (p_0,-\boldsymbol{p})$ is the parity conjugate momentum of $p = (p_0,\boldsymbol{p})$, and use has been made of the fact that $\tilde{k}_1 = k_2$, $\tilde{k}_2 = k_1$ in the $e^-e^+$ c.m. frame. Such identities are useful in checking the numerical programs.



Similarly the helicity amplitudes for the processes $e^-e^+ \to e^-e^+Z$ (Fig. 2.1b) and $e^-e^+ \to \nu_e\bar{\nu}_e Z$ (Fig. 2.1c) are also classified into the contributions of diagrams with ($M_A$) and without ($M_{NA}$) initial $e^-e^+$ annihilation. For the process $e^-e^+ \to e^-e^+Z$ (Fig. 2.1b), we find

$$\begin{aligned} M_{NA} = & \sum_{V=\gamma,Z} J(\langle e_3|V|e_4\rangle)\cdot\left[\hat{J}(\langle e_2|V|e,Z,e_4\rangle)+\hat{J}(\langle e_2,Z,e|V|e_4\rangle)\right] \\ & + \sum_{V=\gamma,Z} J(\langle e_2|V|e_4\rangle)\cdot\left[\hat{J}(\langle e_3,Z,e|V|e_1\rangle)+\hat{J}(\langle e_3|V|e,Z,e_1\rangle)\right], \end{aligned} \tag{2.17}$$

$$\begin{aligned} M_A = & \sum_{V=\gamma,Z} J(\langle e_2|V|e_1\rangle)\cdot\left[\hat{J}(\langle e_3|V|e,Z,e_4\rangle)+\hat{J}(\langle e_3,Z,e|V|e_4\rangle)\right] \\ & + \sum_{V=\gamma,Z} J(\langle e_3|V|e_4\rangle)\cdot\left[\hat{J}(\langle e_2,Z,e|V|e_1\rangle)+\hat{J}(\langle e_2|V|e,Z,e_1\rangle)\right]. \end{aligned} \tag{2.18}$$

For the process $e^+e^+ \to \nu_e\bar{\nu}_e Z$ (Fig. 2.1c), we find

$$\begin{aligned} M_{NA} = & J(\langle\nu_3|W|e_1\rangle)\cdot\left[\hat{J}(\langle e_2|W|\nu,Z,\nu_4\rangle)+\hat{J}(\langle e_2,Z,e|W|\nu_4\rangle)\right] \\ & + J(\langle e_2|W|\nu_4\rangle)\cdot\left[\hat{J}(\langle\nu_3,Z,\nu|W|e_1\rangle)+\hat{J}(\langle\nu_3|W|e,Z,e_1\rangle)\right] \\ & + \Gamma_{WW3}(J(\langle e_2|W|\nu_4\rangle),J(\langle\nu_3|W|e_1\rangle),\cos\theta_W Z), \end{aligned} \tag{2.19}$$

$$\begin{aligned} M_A = & J(\langle e_2|Z|e_1\rangle)\cdot\left[\hat{J}(\langle\nu_3|Z|\nu,Z,\nu_4\rangle)+\hat{J}(\langle\nu_3,Z,\nu|Z|\nu_4\rangle)\right] \\ & + J(\langle\nu_3|Z|\nu_4\rangle)\cdot\left[\hat{J}(\langle e_2,Z,e|Z|e_1\rangle)+\hat{J}(\langle e_2|Z|e,Z,e_1\rangle)\right]. \end{aligned} \tag{2.20}$$

The compact expressions (2.15)–(2.16), (2.18)–(2.21) and (2.23) give complete helicity amplitudes of the single weak boson production processes of (2.1) to (2.4), representing the Feynman diagrams of Figs. 2.1. The differential cross sections for unpolarized beams are then obtained as

$$\mathrm{d}\sigma = \frac{1}{2s\beta}\,\frac{1}{2}\,\frac{1}{2}\sum_{\sigma_i,\lambda_f}|M|^2\mathrm{d}\Phi \tag{2.21}$$

with $\beta = (1-4m_e^2/s)^{1/2}$ and the invariant phase space factor

$$\mathrm{d}\Phi = (2\pi)^4\delta^4(k_1+k_2-p_1-p_2-p_X)\prod_{f=1,2,X}\frac{\mathrm{d}^3p_f}{(2\pi)^3 2E_f}. \tag{2.22}$$

Efficient parametrizations of the above invariant phase space are presented in App. B. A more general distribution for arbitrary polarized $e^+e^-$ beams is found in Ref. [16] in the massless electron limit.

The compactness of the helicity amplitude expressions in the HELAS basis as presented above greatly reduces the chance of making errors in the numerical programs. We have nevertheless performed the following checks of the programs.

First, the same Feynman amplitude can have several different expressions in the HELAS basis, which serves as a nontrivial test. For instance, the diagram of Fig. 2.1a (t1) expressed above as eq. (2.10) can also be written as

$$-\sum_{V=\gamma,Z}\langle e_2, J(\langle e_3|V|e_1\rangle)|e, W, \nu_4\rangle, \tag{2.23}$$

which is now made of scalar products of two spinors, $\langle e_2, J(\langle e_3|V|e_1\rangle)|$ and $|e, W, \nu_4\rangle$. The equivalence of the two expressions is a good test of an amplitude for each Feynman diagram.

Secondly, $CP$ invariance of the amplitudes such as the identity (2.17) has been tested for all the helicity amplitudes. The test has been found to be especially powerful for $CP$ self-conjugate processes, $e^+e^- \to e^+e^-Z$, $\nu_e\bar{\nu}_eZ$.

Thirdly, gauge invariance of the amplitudes are tested by making use of the BRS identity [18]

$$\langle phys;\ \text{out}|\ (\partial^\mu V_\mu - \xi_V m_V \chi_V)\ |phys;\ \text{in}\rangle = 0, \tag{2.24}$$

where $\xi_V$ is the covariant renormalizable gauge parameter and $\chi_V$ the Goldstone mode associated with the vector boson $V$. It follows from the anticomutation relation of the BRS charge [19] and the anti-ghost operator

$$\{Q_{BRS}, \bar{c}_V\} = \partial^\mu V_\mu - \xi_V m_V \chi_V, \tag{2.25}$$

and the physical state conditon

$$Q_{BRS}\ |phys;\ \text{in}\rangle\ =\ \langle phys;\ \text{out}|\ Q_{BRS} = 0. \tag{2.26}$$

The identity (2.24) leads to an exact relationship between the $S$-matrix elements of the four-divergence of the vector boson and those of the associated Goldstone boson

$$\langle phys,\ V_S;\ \text{out}|phys;\ \text{in}\rangle\ =\ -\langle phys,\ \chi_V;\ \text{out}, |phys;\ \text{in}\rangle, \tag{2.27}$$

where $V_S$ denotes the "scalar" component of the vector boson. Eq. (2.27) relates an amplitude with a $V_S$ emisision, which is obtained from the vector boson emission amplitude with the replacement

$$\bar{\epsilon}_V^\mu(p_V, \lambda_V, S_V) \to \frac{\bar{p}_V^\mu}{m_V}, \tag{2.28}$$

to that with the associated Goldstone boson $\chi_V$ emission. The amplitudes with a Goldstone boson emission are often very simple and can easily be evaluated numerically in the HELAS system [17], or in some cases even analytically. The test of the identity (2.27) turns out to be very useful in checking the numerical accuracy of the program for those amplitudes with a longitudinally polarized vector boson emission, which contains at very high energies ($\sqrt{s} \gg m_V$) a numerical cancellation associated with the identity. In case of the $Z$ boson emission processes, $e^-e^+ \to e^-e^+Z$ and $\nu_e\bar{\nu}_eZ$, the right hand side of the identity (2.27) turns out to be proportional to the electron mass, which is reproduced exactly by the numerical program.



The above three independent tests of the numerical programs leave only the overall normalization of the amplitudes to be tested. Those of the $s$-channel annihilation amplitudes, $M_A$'s in eqs. (2.16), (2.19) and (2.21), are tested easily by the associated vector boson pair production cross sections ($e^+e^- \to W^+W^-$ and $e^+e^- \to ZZ$) times the relevant branching fractions. Normalization of the $t$-channel vector boson exchange amplitudes, $M_{NA}$'s in eqs. (2.14) and (2.17) are tested by comparing the exct cross sections and those obtained by the equivalent real particle (photon or electron, dependent on the process) approximations. It is straightforward to replace the external $Z$ boson by a real photon in the numerical programs. The amplitudes of the processes $e^+e^- \to \nu_e\bar{\nu}_eZ$ and $\gamma\gamma Z$ are tested against the known cross sections of the process $e^+e^- \to \nu_e\bar{\nu}_e\gamma$ [20].

We have chosen the unitarity gauge for the gauge sector. One may wonder why we have chosen a gauge with 'bad high-energy behaviour'. There are three reasons. First one is from physics. Since our main concern is to study the symmetry breaking sector, we wish to vary the mass of the Higgs boson, even up to infinite. However, the Higgs mass is directly related to the scalar self-coupling constant, which diverges in the limit of infinite mass Higgs boson. In the renormalizable gauges, we have to include all the Goldstone boson diagrams, and indeed the scalar self-coupling may appear. In these gauges, the limit of the infinite mass Higgs boson is taken by cancelling the scalar self-coupling and the Higgs mass squared in the denominator of the Higgs propagator. In the unitary gauge, all the Goldstone bosons have formally infinite mass, and there is no need to worry about this problem. The infinite mass Higgs simply means that we omit the Higgs exchange diagram. Second one is of technical reason. The number of diagrams in the unitary gauge is much less that that in the renormalizable gauges. Thirdly, the 'bad' high-energy behaviour does not become important for most of the processes, since the gauge bosons are usually connected to the fermion current, which conserve in the vanishing fermion mass limit. Thus the 'bad' high-energy behaviour comes always proportional to the fermion masses, which will not be important except the top quark. In fact, we have found no numerical problems with the choice of the unitarity gauge.

Furthermore, the previous discussion on the BRS identity in checking the amplitudes can be used in the unitarity gauge as well. The BRS identity Eq. (2.24) involves the gauge parameter $\xi_V$ explicitly, where the unitarity gauge is defined by the formal limit $\xi_V \to \infty$. However, the relation between the matrix elements Eq. (2.27) does not include the gauge parameter $\xi_V$ explicitly, hence does not change in this limit.

There is one point we have to be careful in the choice of the gauge when we have collinear photons. The naive Feynman rule gives the off-shell photon wavefunction which approaches the *pure gauge* in the collinear limit. We treat this problem by changing the gauge of the photon wavefunction, as discussed in the App. A. This procedure is justified by another BRS identity

$$\langle phys;\ \text{out}|\ \partial^\mu A_\mu\ |phys;\ \text{in}\rangle = 0, \tag{2.29}$$

where $A_\mu$ is the photon field. This identity is proved again by the anti-commutation relation

$$\{Q_{BRS},\ \bar{c}_A\} = \partial^\mu A_\mu. \tag{2.30}$$

For the process which involve only one $t$-channel photon, for example in the process

$e^+e^- \to e^-\bar{\nu}_e W^+$, the $t$-channel photon exchange diagrams (t1) and (t5) can be rearranged into the form

$$\langle \bar{\nu}_e W^+; \text{ out}|A_\mu|e^+; \text{ in}\rangle J^\mu, \tag{2.31}$$

where the current $J^\mu$ is the off-shell photon wavefunction (2.8). We change the gauge of the current by subtracting a vector proportional to its four-momentum $q^\mu$ :

$$J^\mu \to J^\mu - \frac{J^0}{q^0} q^\mu. \tag{2.32}$$

Thus, this change will subtract a term proportional to

$$\langle \bar{\nu}_e W^+; \text{ out}|A_\mu|e^+; \text{ in}\rangle q^\mu, \tag{2.33}$$

which vanish from the BRS identity as far as the initial positron, final anti-neutrino and the $W^+$ boson remain on-shell physical states.

For the processes where $t$-channel photon is exchanged twice, we need only a little algebra

$$\begin{aligned} &\partial^\mu A_\mu(x)\, \partial^\nu A_\nu(y) \\ &= \{Q_{BRS},\ \bar{c}_A(x)\}\{Q_{BRS},\ \bar{c}_A(y)\} \\ &= Q_{BRS}\bar{c}_A(x)Q_{BRS}\bar{c}_A(y) + \bar{c}_A(x)Q_{BRS}\bar{c}_A(y)Q_{BRS} + Q_{BRS}\bar{c}_A(x)\bar{c}_A(y)Q_{BRS}, \end{aligned} \tag{2.34}$$

where we made use of the nilpotency of the BRS charge $Q_{BRS}^2 = 0$. This identity ensures that the double gauge transformation does not cause any harm as far as the external lines are all on-shell, since the BRS charges at the left-most or right-most annihilates the out- or in-state respectively. Thus the use of the gauge transformation eq. (2.32) of the off-shell photon wavefunction is completely justified.

All the distributions in this paper are obtained from the helicity amplitudes using HELAS.

## 2.2 Phase Space

To obtain the total cross sections and distributions, we should perform the phase space integrations on the final state particles. Since most multi-body final state does not allow us to make the integration analytically, we need some efficient method to perform the integration numerically.

For the two-body final states as discussed in the Chap. 3, the only non-trivial degrees of freedom is the polar angle. We can perform this one-dimensional integration using the Simpson formula, after carefully choosing the angular variable. The choice of the angular variable, however, is a non-trivial point which is the main concern in App. B. We find it often convenient to use rapidity-like variables.

For the multi-body final state discussed in Chap. 4, 5, 6 and 7, the situation will be much more complicated. In fact, we cannot choose good variables without knowing the



singularities running in the multi-dimensional phase space. We should *understand* the regions and strengths of the singularities *before* we do the actual numerical integrations. For this purpose, we discuss in Chap. 3 the 'strengths' of the collinear singularities. Only after getting rough ideas on the singularities, we can choose good phase space variables which are discussed in App. B. They proved to be useful in all processes we discuss in this paper.

In the processes $e^+e^- \to e^-\bar{\nu}_e W^+$ and $e^+e^- Z$ discussed in the previous section, $t$-channel photon exchange appeared. In fact, naive application of HELAS breaks down for these processes, due to severe numerical cancellations especially in the denominator of the $t$-channel photon propagator. We treat this singularity with a special care, as discussed in App. A, which are already incorporated in the HELAS system. The essence lies in that we take $\cos(\theta/2)$ and $\sin(\theta/2)$ rather than the conventional $\cos\theta$ as the inputs to compute the off-shell photon wavefunctions. Thus, we need suitable phase space variables which are directly related to $\cos(\theta/2)$ and $\sin(\theta/2)$. The rapidity-like variables defined in App. B are made to satisfy this requirement. The combination of special subroutines in the HELAS system explained in App. A and the use of the phase space variables of App. B make the quantitative study of the singular processes possible.

Once we know the correct choice of the phase space variables, we utilize the important sampling method of Monte-Carlo integration, conveniently summarized in the FORTRAN77 package BASES25, an updated version of the BASES package [21]. All the histrograms and scatter plots are made by BASES25.

## 2.3 Parameters

The set of electroweak parameters we used in this paper is as follows:

$$\alpha = 1/128, \tag{2.35}$$
$$\sin^2\theta_W = 0.23, \tag{2.36}$$
$$m_Z = 91.17 \text{ GeV}, \tag{2.37}$$
$$m_W = 80.0 \text{ GeV}, \tag{2.38}$$
$$\Gamma_Z = 2.5 \text{ GeV}, \tag{2.39}$$
$$\Gamma_W = 2.0 \text{ GeV}. \tag{2.40}$$

Though the use of the Thomson limit $\alpha = 1/137$ is more appropriate in some cases, we stick to the use of the fine structure constant at the weak scale throughout the paper.

We have not included the effects of beamstrahlung, since we wish to present the cross sections and distributions which do not depend on the details of the collider parameters. Thus our results can be useful for any TeV $e^+e^-$ colliders.

# Chapter 3

# Two-Body Production

In this chapter, we discuss the processes where the initial electron and positron annihilates to produce two-body final states.

This class of processes at $e^+e^-$ collider have been the most familiar ones, such as the lepton/quark pair production at PEP/PETRA/TRISTAN, $Z$-boson production and its two-body decay at SLC/LEP, and $W$-pair production expected at LEP-II. At TeV linear colliders like JLC, this class of processes will remain to be the most important ones, especially its discovery potential of new particles with masses up to $\sqrt{s}/2$, or even to $\sim \sqrt{s}$ for several cases like excited electron etc.

The essential difference from the lower energy colliders is two-fold. One is that the cross section decreases with energy like $1/s$, which is a simple consequence of the partial wave unitarity. Thus, both the signal and the background decreases with energy, though S/N ratio will remain to be $O(1)$ if only the $s$-channel processes are concerned. On the other hand, the single weak boson production processes, though being higher order in the coupling constants, have non-decreasing cross section due to the $t$-channel vector boson exchange. Thus the two-body production processes do not remain to be the dominant processes above $\sqrt{s}$ ~500 GeV. The other $t$-channel processes, such as $e^+e^- \to e^+e^-W^+W^-$ will also have the cross sections of $O(1)$ pb.

The decrease of the cross section of the $s$-channel processes requires larger luminosity at higher energies. The integrated luminosity of the order of 10 fb$^{-1}$/yr will be the minimum requirement for the TeV linear colliders. This point is the strongest restriction to the design of the accelerator.

The second difference is that the number of the final state jets is much larger than the lower energy colliders, due to the copious production of the weak bosons and top quarks. The weak bosons[1] mainly decay into two jets, and the final state will have four-jets structure. The top quarks will decay in a cascade; $t \to bW^+$ followed by $W^+ \to$ two jets. Thus the event has six jets at least! The hadron calorimentry with good energy and angular resolution is required.

[1]We refer to the $W$ and $Z$ bosons as the "weak bosons" throughout the paper.



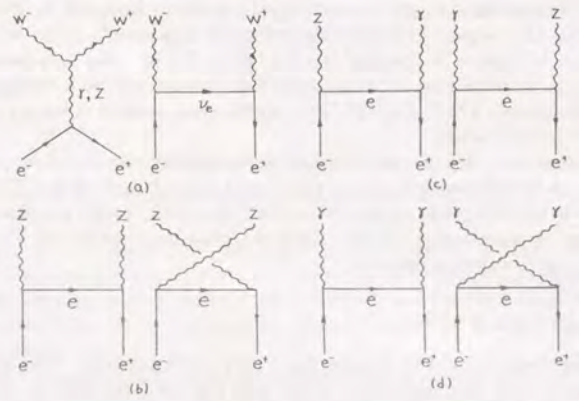


Figure 3.1: Feynman diagrams for the two vector boson production processes. (a) $e^+e^- \to W^+W^-$, (b) $e^+e^- \to ZZ$, (c) $e^+e^- \to Z\gamma$ and (d) $e^+e^- \to \gamma\gamma$.

## 3.1 Physics Interests in the Processes

All the processes have different interests from the physics point of view. We will discuss the interests in each processes separately.

### 3.1.1 $e^+e^- \to W^+W^-$

The pair-production of the $W$-boson will be first observed at LEP-II. The precise measurement of the mass and the width will be made there. The TeV linear colliders will have no advantages in the measurements of the mass and the width compared with LEP-II. The Feynman diagrams of this process are shown in Fig. 3.1(a).

The interest in the $W$-pair production at TeV linear collider concerns the detailed study of the interactions of the $W$-bosons. One of the interest lies in the study of the gauge boson self-interactions with photon and $Z$ boson which appear in the first Feynman diagram. The self-interactions are completely determined by the Yang-Mills structure of the $SU(2)_L \times U(1)_Y$ gauge theory, though they are expected to deviate from the Yang-Mills type couplings if the $W$ and $Z$ bosons are composite objects with inner structures. The capablitiy of the JLC in studying the anomalous couplings like anomalous magnetic moment or electric quadrupole moment of $W$-boson will be discussed in the Ref. [28]. Another interest lies on the interaction of the $W$-boson with themselves, which appear as the final state interactions after its pair production. The effect of the strongly interacting Higgs

sector or the contribution from techni-$\rho$ like resonances are discussed by Iddir *et al.* [22]. The re-scattering in the strongly-interacting case was also discussed by Hikasa [23].

There is another aspect in which this process is important. Since many new physics signals contain $W$-bosons in the final state, $e^+e^- \to W^+W^-$ can be a serious background due to its large cross section. For example, this process will be a background for Higgs hunting in the process $e^+e^- \to \nu_e\bar{\nu}_e W^+W^-$, where some portion of energy may be lost due to the beamstrahlung effect.

Another interest in this process arises as the luminosity monitor of the machine. As will be discussed in the following sections, the largest contribution of the $W$-pair production comes from the forward peak, which will be little affected by exotic physics, such as anomalous couplings or rescattering effects. Thus the total cross section of $W$-pair production may be useful as luminosity monitor.

### 3.1.2 $e^+e^- \to ZZ$

The Feynman diagrams of this process are shown in Fig. 3.1(b). This process, in itself, has no interesting physics, since there appear only the couplings between the $Z$-boson with the electron which is already well-tested at LEP. Furthermore the re-scattering effect is small, since the final $Z$ bosons are dominantly transversely polarized, hence not sensitive to possible strongly-interacting Higgs sector. However, this process is important in that it constitutes the largest background to the Higgs production via $e^+e^- \to ZH$.

The lack of new physics signals enables this process to serve as the luminosity monitor. It will be also important to use this process for the calibration of the hadron clorimentry. For this purpose, we should have longitudinal polarization of the electron beam to select out the positive chirality sector to reduce the large background from $e^+e^- \to W^+W^-$.

### 3.1.3 $e^+e^- \to Z\gamma,\ \gamma\gamma$

The Feynman diagrams of these processes are shown in Fig.3.1(c) and (d). There appear only the well-tested coupling of $eeZ$ and $ee\gamma$. We therefore expect no interesting physics in these processes at the tree-level. However, it is claimed that the charged current radiative correction to the process $e^+e^- \to Z\gamma$ is as large as $-25\%$ [24].

### 3.1.4 $e^+e^- \to t\bar{t}$

The top quark is expected to be discovered at Tevatron or LHC before any TeV linear colliders start operation. Thus we will know the rough value of its mass at that time.

The study of the threshold region of the top quark pair production will be one of the main goals at first stage $e^+e^-$ linear collider [25,26,27]. The threshold behavior of the top quark production will be very different from the familiar charm or bottom production, where many sharp resonances like $J/\psi$ or $\Upsilon$ with typical width of the order keV are observed. Since the top quark is known to be heavier than the $W$-boson [11], it decays into *real* $W$ unlike the decay into *virtual* $W$ of charm or bottom quark. The width of the top quark is



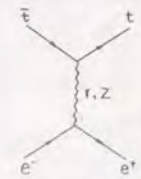


Figure 3.2: Feynman diagram of the process $e^+e^- \to t\bar{t}$.

very large, typically of the order of GeV, which makes the formation of sharp $\Theta$ resonances impossible. Thus the threshold region of $t\bar{t}$ production has an interesting interplay between the electroweak physics (top decay) and QCD ($t\bar{t}$ potential), and the theoretical analysis can be done fairly confidently due to the applicability of perturbative QCD to the short-distance part of the $t\bar{t}$ potential.

The interests in the study of the threshold behavior lies on precise measurements of the mass of the top quark, the width or $|V_{tb}|$ from the width of the would-be resonances, the QCD strong couplings constant $\alpha_s$ from the spectra, and even the Higgs-boson exchange potential. In particular, the measurement of the Kobayashi-Maskawa matrix element $|V_{tb}|$ has a high discovery potential. If it is much less than unity, it signals the existence of the fourth generation. If it is larger than unity, it signals an exotic decay channel, like the decay into a charged Higgs boson via $t \to bH^+$, or into the superpartner $t \to \tilde{t}\tilde{\gamma}$ which may be much lighter than the top quark itself. This threshold behavior of the top-pair production will not be discussed further in this paper.

There are many interests in the open top-pair production. The main interest is the measurement of the vector and axial vector coupling of the top quark to the $Z$-boson from total production rate and the forward-backward asymmetry (Fig. 3.2). The axial vector coupling may deviate largely from the tree-level coupling when the Higgs sector, which generates the mass of the top quark, is strongly interacting. Vertex corrections from the Higgs exchange or extended technicolour interactions may be observable. The study of its decay $t \to bW^+$ is interesting here again, since the effect of the strongly interacting sector may show up in the ratio $\Gamma(t \to bW_L^+)/\Gamma(t \to bW_T^+)$.

## 3.2 Cross Sections and Distributions

We first concentrate on the vector boson two-body production processes. The $t\bar{t}$ production will be discussed in the sequel.

The energy dependence of the total cross sections is shown in Fig. 3.3. Here the "point" cross section $\sigma_{\rm pt}$ is shown for comparison. The sharp peak of the cross section of the process $e^+e^- \to Z\gamma$ just above the threshold is due to the soft singularity in the limit where the energy of the photon goes to zero $E_\gamma \to 0$. In fact, the cross section diverges in this limit since the denominator of the $t$-channel electron propagator will vanish. The

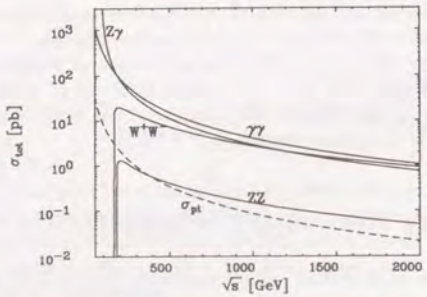


Figure 3.3: Energy dependence of the two-body production cross sections. The point cross section defined in eq. (3.1) is shown for comparison as the dashed line. The fine structure constant is fixed to be $\alpha = 1/128$ for all processes except for $\sigma_{\rm pt}$. Electroweak parameters of eqs. (2.36–38) are used.

singularity should be handled by the summation over the multi-photon emission processes to "exponentiate" the singularity; hence the curve shown here should not be taken seriously very near the threshold $\sqrt{s} \sim m_Z$. The 'point' cross section $\sigma_{\rm pt}$ is shown for comparison, where it is *defined* to be

$$\sigma_{\rm pt} = 86.8 \text{ fb TeV}^2/s. \tag{3.1}$$

At all energies much above $m_W$ and $m_Z$, the angular distribution for the $W^+W^-$, $Z\gamma$, $ZZ$ and $\gamma\gamma$ production is strongly peaked in the collinear region due to the $t$-channel electron or neutrino propagator. Since the treatment of the collinear singularities is essential in dealing with the processes in the later sections, let us discuss the 'strengths' of the collinear singularities briefly. The point is that one can estimate the typical angles in the forward region as follows.

For the processes involving photons, $e^+e^- \to \gamma\gamma$ and $Z\gamma$, the denominator of the electron propagator behaves like

$$\begin{aligned}(p_{e^-} - p_\gamma)^2 - m_e^2 &= -2p_{e^-}\cdot p_\gamma \\ &= -2E_{e^-}E_\gamma(1-\beta\cos\theta) \\ &\sim -2E_{e^-}E_\gamma(1-\cos\theta+\frac{2m_e^2}{s})\end{aligned} \tag{3.2}$$

in the collinear ($\cos\theta \to 1$) region, where $E_\gamma = E_{e^-}$ in $\gamma\gamma$ case and $E_\gamma = E_{e^-}(1-m_Z^2/s)$ in $Z\gamma$ case. On the other hand, there is a universal selection rule that the emitted vector boson has dominantly the helicity of the same sign as that of the electron in the collinear limit. One can check this easily by evaluating the helicity amplitudes. See App. C for further details. We show one example for the case $e^+e^- \to Z\gamma$ in Fig. 3.4, where the initial electron beam is longitudinaly polarized to have negative helicity. This example clearly exhibits the



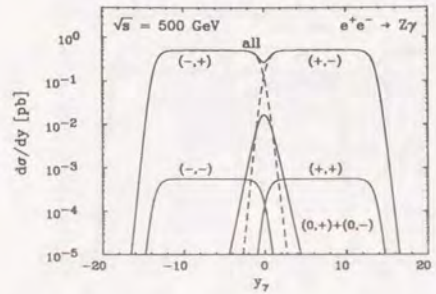


Figure 3.4: Pseudo-rapitidy distribution of the final photon in the process $e^+e^- \to Z\gamma$. The elctron beam is left-handed. The contribution from various helicity combinations are shown separately. The helicities are labeled in the order $(Z,\ \gamma)$. The positive $z$-direction is taken to be the same as the direction of $e^-$ beam.

above selection rule. This rule prohibits the emission of a vector boson in *strictly* collinear direction $\cos\theta = 1$, where the amplitude vanishes like $\sin(\theta/2)$ due to the conservation of angular momentum. Thus the cross section behaves in the collinear region like

$$\frac{d\sigma}{d\cos\theta} \sim \frac{1-\cos\theta}{(1-\cos\theta+\Delta)^2}, \tag{3.3}$$

where $\Delta = 2m_e^2/s$ in this case. Thus the singularity in the collinear region persists to the angles where $1-\cos\theta \sim \Delta$, and there appears a flat region (plateau) in the pseudo-rapidity distribution.

In the weak boson pair production processes $e^+e^- \to W^+W^-$ and $ZZ$, the singularity is much 'weaker' due to the large weak boson mass. The denominator of the $t$-channel neutrino/electron propagator behaves like

$$\begin{aligned}(p_{e^-} - p_V)^2 - m_e^2 &= -2p_{e^-}\cdot p_V + m_V^2 \\ &= -2E_{e^-}E_V(1-\beta_V\beta_e\cos\theta) \\ &\sim -2E_{e^-}^2\left(1-\frac{2m_V^2}{s}\right)(1-\cos\theta+\frac{2m_V^4}{s^2})\end{aligned} \tag{3.4}$$

neglecting the electron mass and expanding in the powers of $m_V^2/s$ in the last line. Here, $V$ is either $W$ or $Z$. Thus the 'strength' of the collinear singularity here is described by $\Delta = 2m_V^4/s^2$.

The pseudo-rapidity distribution at $\sqrt{s} = 500$ GeV is shown in Fig. 3.5 to illustrate the above discussion. Here, the pesudo-rapidity is defined as usual by

$$y = \frac{1}{2}\log\left(\frac{1+\cos\theta}{1-\cos\theta}\right). \tag{3.5}$$

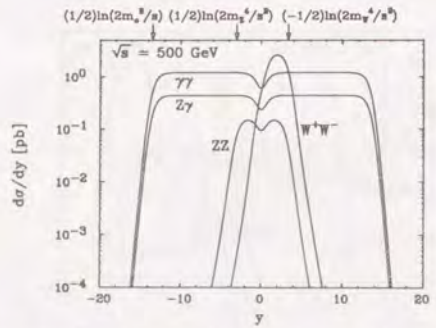


Figure 3.5: Pseudo-rapidity distributions of the two-body production processes. The curves for $\gamma\gamma$ and $ZZ$ should be integrated only over the region $0 \leq \cos\theta \leq 1$ to avoid double counting.

One can see the wide plateau for the photon emission processes, which gives the logarithmic enhancement factor to the total cross section. The wide plateau suggests that the picture of the equivalent electron approximation is valid here, in which the off-shell electron after the emission of the collinear photon can be regarded as *on-shell*. This is indeed the essence of the treatment of the initial state radiation of the photons from the electron beam. The typical rapidity $y = \pm(1/2)\log\Delta$ is shown by the arrows in the top of the figure. We see that the 'strength' of the collinear singularity is indeed described by the $\Delta$'s obtained above. The structure of the plateaux is hardly visible for $W^+W^-$ and $ZZ$ final state; which can be understood by the large weak boson masses, and the plateau indeed appears above $\sqrt{s}$ >5 TeV or so. The remarkable flatness of the distribution, especially for the photon case, is useful in dealing with the collinear singularities for the higher order processes, where the rapidity-like variable defined in the App. B is really a good choice for the phase space variable.

Though the plateaux in the pseudo-rapidity distribution is still not clearly visible for the weak boson production, the selection rule for the helcities can be seen clearly for the $W^+W^-$ final state as well. We show the $\cos\theta$ distribution for each helicity combination separately. One can see that the helicity state $(-,+)$, where the first one corresponds to the $W^-$ and the second to $W^+$, dominates the cross section in the collinear region. Recalling that the collinear singularity comes from the $t$-channel propagator of the Feynman diagram Fig. 3.1(a)(1), and that the diagram is absent for the positive chirality electron, we see that the collinear singularity comes solely from the negative chirality electron, where the initial $e^-$ has negative helicity $-1/2$ and $e^+$ has $1/2$. Thus the selection rule holds here as well. One can observe similar selection rule for $ZZ$ production; however we should longitudinally polarize the electron beam to separate out the contribution from different chiralities to observe the selection rule.

There is one more remark for the helicity combinations in the $W$-pair production process.



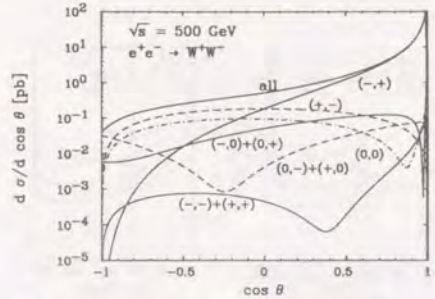


Figure 3.6: Angular distribution of the process $e^+e^- \to W^+W^-$. The contributions of various helicity combinations are shown separately. The helicites are labeled in the order $(W^-,\ W^+)$.

We are expecting that most new physics signals come from longitudinally polarized $W$-bosons ($W_L$), since they originate from the Goldstone bosons which are direct products of the symmetry-breaking. For the non-gauge theories like composite $W/Z$-boson scenarios, the anomalous couplings between the vector bosons show up most strongly for $W_L$'s. One can see from the Fig. 3.6 that the $W_L$ contribution is sizable for the *backward* region, though it is negligible in the forward region where the $(-,+)$ helicity combination dominates because of the selection rule mentioned above. In fact, one sees that the effect of the anomalous couplings show up in the angular distribution at the backward region [28]. The forward peak is completely insensitive to new physics, and may even be used for one of the luminosity monitors.

We show the transverse momentum ($p_T$) distribution in Fig.3.7 for $\sqrt{s} = 500$ GeV and $\sqrt{s}$ =1 TeV. The sharp peak in the large $p_T$ region is purely kinematical Jacobian peak. The small $p_T$ region reflects the dynamics of each processes, with peaks with typical $p_T$ of the order $O(m_e)$ for the photon emission processes and $O(m_V^2/E_{e^-})$ for the weak boson production processes. Note that this typical $p_T$ is just the typical 'mass' of the virtual particle exchanged in the $t$-channel, where 'mass' of a virtual particle is defined by the square root of the denominator of its propagator.

Summarizing this chapter, we show the 'typical' kinematical configuration in the Fig. 3.8 where the cross section is dominated. Here the readers are warned not to confuse these figures as Feynman diagrams. In particular, we cannot select out one Feynman diagram only as the representative to claim that particular one is dominant, since such an artificial treatment will break gauge invariance. However, it is often true that the intuition from the 'typical' Feynman diagram gives the correct qualitative, even quantitative, understanding of the exact results which can be obtained only after adding the whole set of the Feynman diagrams. In this sense, though these figures should be understood as only schematic ones, we can read off the 'typical' $p_T$ or angular distributions. We show similar figures for all the

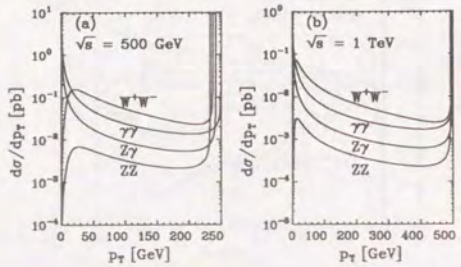


Figure 3.7: Transverse momentum distributions of twobody production processes at c.m. energy of (a) 500 GeV and (b) 1 TeV.

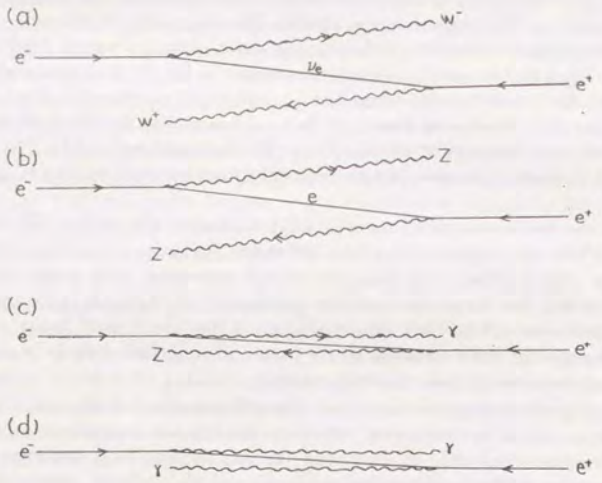


Figure 3.8: Typical kinematical configurations for the twobody production processes. (a) $e^+e^- \to W^+W^-$. (b) $e^+e^- \to ZZ$. (c) $e^+e^- \to Z\gamma$. (d) $e^+e^- \to \gamma\gamma$. The arrows in the figures show the energy flow, not the fermion number.



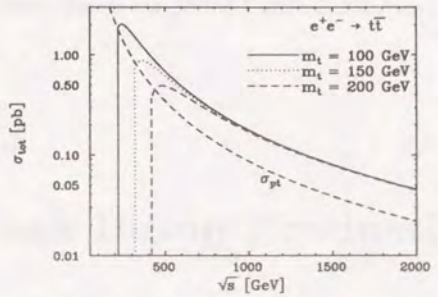


Figure 3.9: Total cross section of the $t\bar{t}$ production for $m_t = 100$, 150 and 200 GeV.

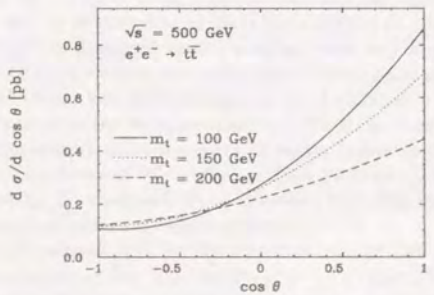


Figure 3.10: Angular distribution in the $t\bar{t}$ pair production at c.m. energy of 500 GeV, for $m_t = 100$, 150 and 200 GeV.

processes discussed in this paper.

Now we come to the top quark. Here we deal only with the tree-level amplitudes without QCD corrections. The corrections from QCD to a rapidly decaying particle like top quark is a non-trivial problem, since the naive inclusion of the width into the top quark propagator will violate the QCD gauge invariance. We stick to the tree-level predictions here.

The total cross section of the $t\bar{t}$ open production is shown in Fig. 3.9. Much larger cross section than the 'point' cross section $\sigma_{\rm pt}$ is a consequence of the constructive $\gamma - Z$ interference above the $Z$-boson pole.

The angular distributions of the $t\bar{t}$ production are shown in the Fig. 3.10. One observes that the forward-backward asymmetry is quite large. At the TeV linear colliders, the contributions from photon exchange and the $Z$-boson exchange are comparable, and the effect of the interference will remain very large. At very high energies well beyond the $Z$-boson pole, the forward-backward asymmetry reaches its asymptotic value. The energies

we discuss here in this paper, 500 GeV to 1.5 TeV, are already nearly in the asymptotic region.



# Chapter 4

# Single Weak Boson Production

At TeV energies, the cross sections of all $s$-channel processes like those discussed in the previous chapter drop as $1/s$ up to some logarithms. Thus the typical cross section at TeV $e^+e^-$ linear colliders will be of the order of $O(1)$ fb to $O(100)$ fb. However, the single weak boson production processes discussed in this chapter have very large cross section at TeV region of the order of $O(1)$ pb or even up to $O(10)$ pb! Their cross section is non-decreasing with $s$, since there are vector bosons exchanged in the $t$-channel.

The copious production of the weak bosons from this class of processes will be a serious background to the Higgs search or to the study of vector boson scattering if we look for the leptonic mode of the weak bosons, $W \to e^\pm\nu_e$ or $Z \to \nu\bar{\nu}$ mode. For example, the process $e^+e^- \to ZH$, followed by $Z \to \nu\bar{\nu}$ and $H \to b\bar{b}$ suffers from the backgrounds to which all the single $W/Z$ production processes will contribute.

Though this class of processes will be the dominant ones at TeV linear colliders, systematic study has not been made so far. The process $e^+e^- \to e^\pm\nu_e(\bar{\nu}_e)W^\mp$ was studied from the interest in the anomalous $WW\gamma$ vertex [29]. The process $e^+e^- \to e^+e^-Z$ has been studied only from equivalent photon approximation [30]. No study on the process $e^+e^- \to \nu_e\bar{\nu}_eZ$ is made as far as we know. The difficulty in the study stems from the $t$-channel singularities, which renders the naive numerical evaluation of the exact matrix elements unreliable. The detailed study can be made only by a systematic method treating the $t$-channel singularities both for the amplitudes and the phase space, like the one discussed in App. A and B.

## 4.1 Physics Interests in the Processes

Although the main interests in this class of the processes are that they can consitute important backgrounds for various studies due to their large cross sections, they do have some intrinsically interesting aspects. We discuss them separately.

### 4.1.1 $e^+e^- \to e^\pm\nu_e(\bar{\nu}_e)W^\mp$

As noticeable from the Feynman diagrams shown in Fig. 2.1(a), there appear three-point vector boson self-couplings. The detailed study of the anomalous $WW\gamma$ vertex is possible

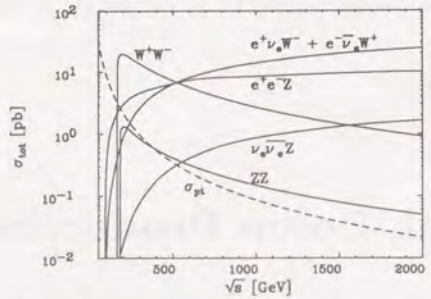


Figure 4.1: Total cross sections for the single weak boson production processes. The cross sections for $W$-pair and $Z$-pair production as well as the point cross section are shown for comparison.

thanks to the large cross section, which has been the main concern in the past literatures.

Aside from the interests in the anomalous vector boson couplings, the process is indeed the most dominant one at $e^+e^-$ collider above 600 GeV except for the small angle Bhabha scattering. Thus this process serves as an ideal place for the calibration of hadron calorimetry on the $W$-boson, which will turn out to be essential in the study of the vector boson fusion processes.

### 4.1.2 $e^+e^- \to e^+e^-Z$

In the Feynman diagrams Fig. 2.1(b), we see that there appear only the familar couplings $ee\gamma$ and $eeZ$ vertices. Thus there will be no new physics signal unless the electron itself shows its composite structure. If this occurs, we may expect a peak in $eZ$ invariant mass corresponding to an excited electron, or large angle events due to $t$-channel excited electron exchange, etc.

### 4.1.3 $e^+e^- \to \nu_e\bar{\nu}_e Z$

The Feynman diagrams are shown in Fig. 2.1(c). There appears $WWZ$ coupling in the diagrams (t5), while other diagrams have only the familiar $ffV$ vertices. Thus this process measures the coupling between $W$ and $Z$ bosons exclusively, where the process $e^+e^- \to W^+W^-$ measure a certain combination of the $WW\gamma$ and $WWZ$ vertices. The sensitivity to the anomalous couplings expected in the composite models will be discussed in Ref. [28].

## 4.2 Cross Sections and Distributions

The total cross sections are shown versus the c.m. energy of the initial $e^+e^-$ in Fig. 4.1.



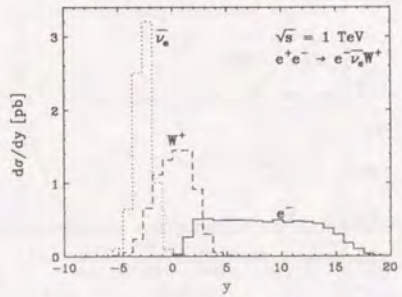


Figure 4.2: Pseudo-rapidity distributions of final state particles in the process $e^+e^- \to e^-\bar{\nu}_e W^+$ at c.m. energy 1 TeV.

One observes the cross-over where the $s$-channel processes, whose cross sections drop like $1/s$, cease to be the dominant processes, and the single weak boson production will be the most dominant processes at $e^+e^-$ collider. The cross-over occurs around 600 GeV, where the cross section for the single $W$ production will dominate others, except for the small angle Bhabha scattering.

In order to see the structure of the collinear singularities of these processes, we show the pseudo-rapidity distributions of the final $e^+$, $e^-$, $\nu_e$, $\bar{\nu}_e$ and the weak bosons in the Figs. 4.2, 4.5 and 4.10 for $\sqrt{s} = 1$ TeV.

Let us discuss the case $e^+e^- \to e^-\bar{\nu}_e W^+$ first. The wide plateau of the pseudo-rapidity distribution of the scattered $e^-$ is just the one expected, which shows that the process is indeed dominated by the $t$-channel photon exchange. The 'strength' of the singularity as discussed in the previous chapter is estimated by the $t$-channel photon propagator:

$$\begin{aligned}(p_{e^-}^{\text{initial}} - p_{e^-}^{\text{final}})^2 &= 2m_e^2 - 2E_{\text{beam}}^2 x(1 - \beta_i\beta_f\cos\theta) \\ &= -\frac{s}{2}x\beta_i\beta_f(1 - \cos\theta + \Delta(x)),\end{aligned} \tag{4.1}$$

where $x$ is the energy fraction of the final $e^-$ viz. $E_{e^-}^{\text{final}} = xE_{\text{beam}}$, and

$$\Delta(x) = 2\frac{m_e^2}{s}\frac{(1-x)^2}{x^2} + O\left(\frac{m_e^2}{s}\right)^2. \tag{4.2}$$

Here, $x$ can become as large as

$$x_{\max} = 1 - \frac{m_W^2}{s}, \tag{4.3}$$

which leads to a very small number $\Delta(x_{\max}) = 2\times10^{-17}$ at $\sqrt{s} = 1$ TeV! This $\Delta(x)$, indeed, describes the end of the plateau in the pseudo-rapidity distribution if $x$ is fixed. The edge of the plateau will be smeared after the integration over $x$ due to the $x$-dependence of the $\Delta(x)$.

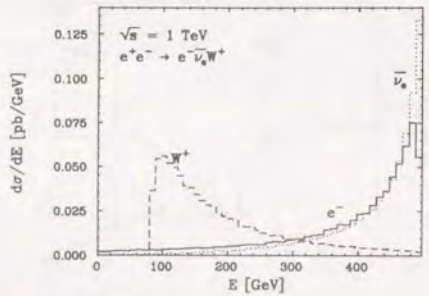


Figure 4.3: The energy distribution in the process $e^+e^- \to e^-\bar{\nu}_e W^+$.

This flat region can be handled with equivalent photon approximation quite accurately, which approximates the other parts of the matrix elements as constant while integrating over $\cos\theta$ in the above singular region. If this approximation is valid up to a larger angle $1-\cos\theta \sim U$, the integration gives the well-known logarithmic factor

$$\frac{\alpha}{2\pi}\frac{1+x^2}{1-x}\left(\log\frac{U+\Delta(x)}{\Delta(x)}-1\right). \tag{4.4}$$

The upper limit $U$ should be chosen carefully in a process-dependent way so that it reproduces the exact results. We refer to Ref. [31] for the detail. In this case, it is appropriate to set $U = m_W^2/s$, which shall be clear after the discussion of the 'mass ordering' rule.

The energy distribution Fig. 4.3 of the final electron clearly supports the above picture, where it behaves like $1/(1-x)$ in the limit $x \to 1$.

The reach of the pseudo-rapidity distribution of the anti-neutrino $\bar{\nu}_e$ can be understood by considering the subprocess $\gamma e^+ \to \bar{\nu}_e W^+$ neglecting the 'mass' of the photon. This subprocess is governed by the $t$-channel $W$-propagator, which gives the singularity with the 'strength':

$$\begin{aligned}(p_\gamma - p_{W^+})^2 - m_W^2 &= -2p_\gamma \cdot p_{W^+} \\ &\sim -\frac{\hat{s}}{2}\left(1+\frac{m_W^2}{\hat{s}}\right)\beta_W\left(1-\cos\hat{\theta}+2\frac{m_W^2}{\hat{s}}\right),\end{aligned} \tag{4.5}$$

where $\hat{s}$ is the invariant mass of the subprocess. Thus, the 'strength' of the singularity is always less than $m_W^2/s$ and the pseudo-rapidity of the scattered anti-neutrino is indeed spread within the width $(1/2)\log(m_W^2/s)$. The peak of this distribution is shifted to the negative direction, due to the Lorentz boost from the c.m. frame of the subprocess to the laboratory frame. The pseudo-rapidity of the $W^+$ is fixed by balancing with the electron and anti-neutrino. We show the 'typical' configuration in Fig. 4.4 to summarize the above discussion. Here, the $t$-channel photon is emitted first form the electron, the electron losing



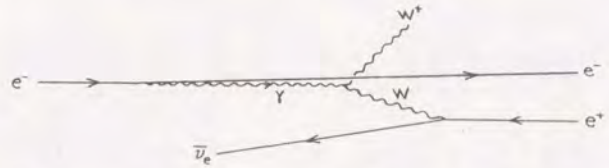


Figure 4.4: Typical kinematical configuration of the process $e^+e^- \to e^-\bar{\nu}_e W^+$.

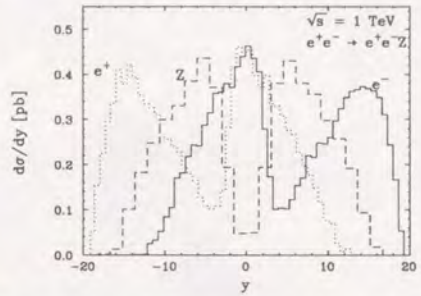


Figure 4.5: Pseudo-rapidity distribution in the process $e^+e^- \to e^+e^-Z$.

little energy. The photon collides with the positron beam, to produce $W^+$ and $\bar{\nu}_e$ by exchanging the $W$-boson in the $t$-channel. This is consistent with the peak in the $E_{\bar{\nu}_e}$ at high energy and softness of the final $W^+$.

The pseudo-rapidity distribution in the process $e^+e^- \to e^+e^-Z$ requires more explanation. The Fig. 4.5 shows that there are *two* singular regions, where the initial electron runs into the forward direction ($y > 0$), or backward direction ($y < 0$). One should look at the scatter plot (Fig. 4.6) to see the situation. Here, the doubly differential distribution $d^2\sigma/dy_{e^-}dy_{e^+}$ is shown, normalized such that the bin with the largest differential cross section has the value 10 (denoted by $*$). We see that both $e^-$ and $e^+$ prefer to run into the same direction (the same sign of the pseudo-rapidity).

This process can be understood in the following "parton" picture, where the electron beam is regarded as a 'composite' object of an electron, photons and $e^+e^-$ pairs, in precise analogy to the quarks in the hard scattering processes. See Fig. 4.7. Here, suppose that the positron beam is the 'probe' of the structure of the 'electron'. First, the initial electron (or positron) emits the $t$-channel photon, revealing its structure as the photon-electron composite. Here the initial electron does not lose much of its energy, and flies away. Then the photon again reveals its deeper 'structure', that it has a component as an $e^+e^-$ pair. The electron, which is the 'constituent' of the photon, will undergo a hard collision with the


Figure 4.6: Scatter plot on the plane $(x,\ y) = (y_{e^-},\ y_{e^+})$ in the process $e^+e^- \to e^+e^-Z$. The plot exhibits the "angular ordering" [32] where all the dominant regions lie below the diagonal $y_{e^-} = y_{e^+}$.



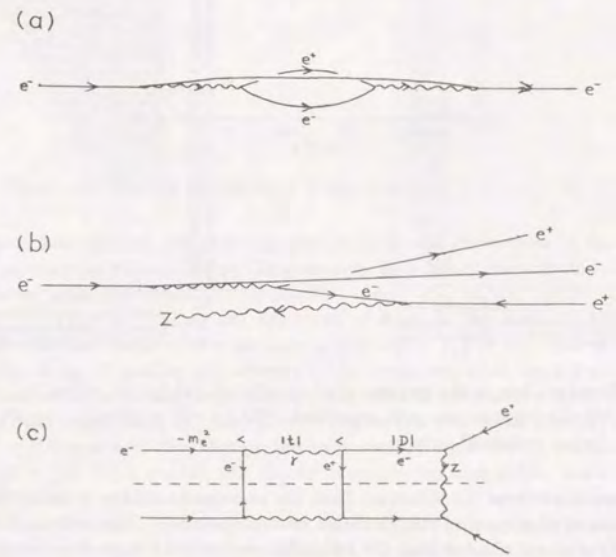


Figure 4.7: The typical configurations in the process $e^+e^- \to e^+e^-Z$. (a) The "structure" of the electron as a composite of the "valence" $e^-$ and "sea" $e^-e^+$ pair. (b) The positron beam collides hard on the "sea" $e^-$ inside the electron beam. (c) The ladder diagram with the "mass ordering" rule.

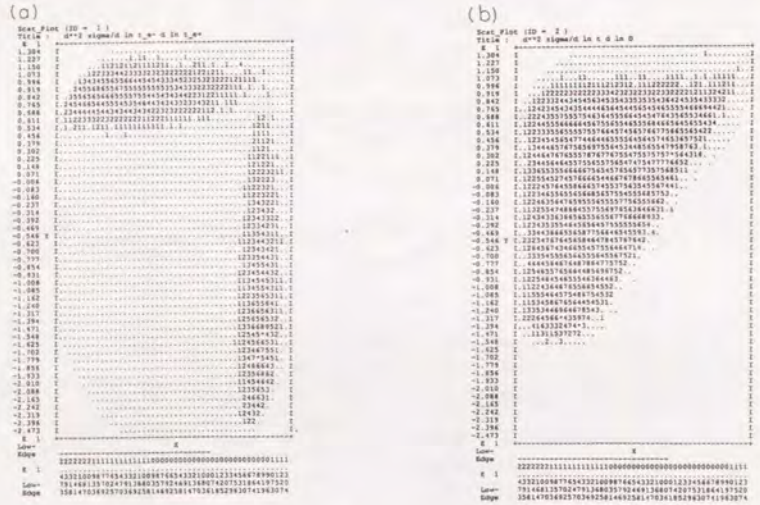


Figure 4.8: Scatter plots in the process $e^+e^- \to e^+e^-Z$. (a) $(x,\ y) = (\log|t_1|,\ \log|t_2|)$ plot, where two singular regions are well separated. (b) $(x,\ y) = (\log|t|,\ \log|D|)$ plot which exhibits the "mass ordering" rule.

positron beam to produce the $Z$ boson. Thus the positron beam has revealed the 'structure' of the electron as composed of two electrons and one positron. The scatter plot shows that the secondary electron created from the $t$-channel photon has always *larger* angles compared to the primary electron which has emitted the photon. This is an example of the "angular ordering" rule where the 'parton' which is produced nearer to the hard process has larger angles.

Now it is the right place to discuss the 'mass' ordering rule. This rule states the dominant kinematical configurations in the successive emission of the collinear particles lies in the region where the 'mass' of the primary one is smaller than the 'mass' of the secondary (or deeper) one, which makes a ladder where the partons will be successively more virtual. In fact, the large logarithms in the leading-log approximation appear from this kinematical region. To check this ordering, we should first know which ($e^-$ or $e^+$) acted as the hard scatterer.

We first show the scatter plot of the momentum transfers, or the 'mass' of the photons, computed from the final electron and positron four-momenta in Fig. 4.8(a). Two singular regions are well-separated, the region spreading horizontally corresponds to the case where the electron has emitted the collinear photon, while the region spreading vertically corresponds to the opposite case. Thus we can distinguish quite well which of the



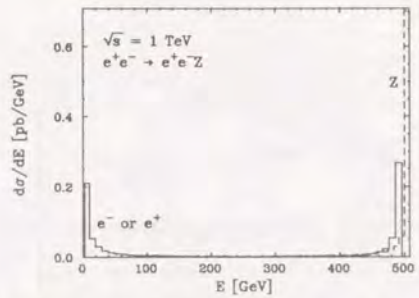


Figure 4.9: Energy distribution in the process $e^+e^- \to e^+e^-Z$.

electron/positron has emitted the collinear photon from the kinematics of the final state particles. Let us suppose without losing the generality that the $e^-$ has emitted the collinear photon. Then we know the 'mass' of the photon, which is a 'parton' inside the electron, to be $|t| = q^2 = -(p_1 - k_1)^2$ using the notations of App. B. We compare this 'mass' of the photon $|t|$ with the 'mass' of the electron $|D| = -(q - p_2)^2 + m_e^2$. We show the two dimensional plot in $\log|t|$ and $\log|D|$, where $t$ is the denominator of the $t$-channel photon, and $D$ is the denominator of the $t$-channel electron, both in the same scale in Fig. 4.8(b). Since $|D|$ is always larger than $m_e^2$, the allowed region lies above the line $|D| = \log(m_e^2)$. The region $|t| < |D|$ is almost flat, though the cross section immediately vanishes when we cross the line $|t| = |D|$. This scatter plot clearly supports the idea of the 'mass ordering'.

Thus, in integrating over the angles of the final electron, the upperbound of the angle is determined from this rule. This rule can be applied quite generally to many processes, and indeed the upperbound $1 - \cos\theta = m_W^2/s$ in the process $e^+e^- \to e^-\bar{\nu}_e W^+$ can be understood from this rule since the absolute value of the denominator of the $t$-channel $W$-boson propagator is larger than $m_W^2$.

The distributions of the energies of final state particles match the above idea (Fig. 4.9). The energy of the electron has a sharp singularity as $x \to 1$, where it behaves like $1/(1-x)^2$, one factor of $1/(1-x)$ coming from the photon luminosity function, and another $1/(1-x)$ from the subprocess. The $Z$ boson has an energy $\sim E_{\rm beam}$, since it is produced by the soft electron, produced from the $t$-channel photon, colliding hard on the other incoming beam.

The last process we discuss here is $e^+e^- \to \nu_e\bar{\nu}_e Z$. We again show the pseudo-rapidity distribution of the final state particles (Fig. 4.10). The reach of pseudo-rapidity can be completely understood just like in $e^-\bar{\nu}_e W^+$, where the $t$-channel $W$-boson exchange leads to a singularity of 'strength' of $m_W^2/s$. Here the spread of the pseudo-rapidity distribution of the final neutrino and anti-neutrino is indeed explained by $(1/2)\log(m_W^2/s)$. The $Z$-boson is produced centrally. This process is a proto-type of the $W$-fusion process, which we encounter again in $e^+e^- \to \nu_e\bar{\nu}_e H$ and vector boson fusion processes. The distribution in the logarithm of the $t$-channel $W$-boson propagator is shown in Fig. 4.11. Since the

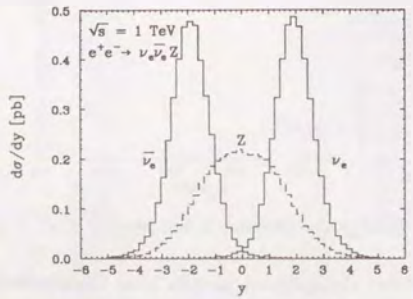


Figure 4.10: Pseudo-rapidity distribution of the process $e^+e^- \to \nu_e\bar{\nu}_e Z$.

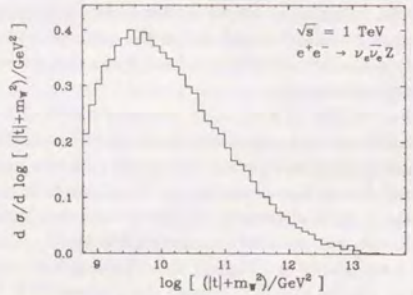


Figure 4.11: The distribution in the logarithm of the denominator in the $t$-channel $W$-boson propagator.



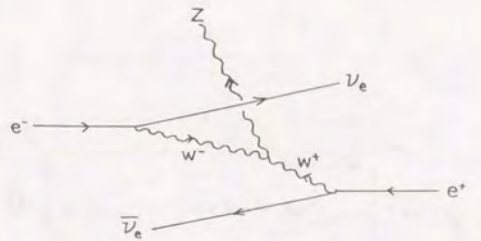


Figure 4.12: Typical kinematical configurations in the process $e^+e^- \to \nu_e\bar{\nu}_e Z$.

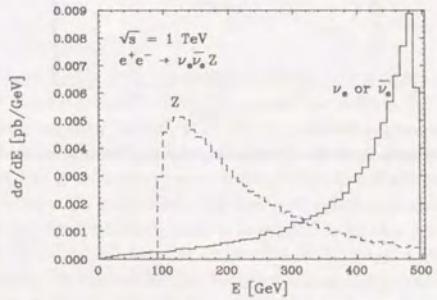


Figure 4.13: Energy distribution of the final particles.

denominator of the $W$-boson propagator always has a larger absolute value than $m_W^2$ (or smaller than $-m_W^2$), the distribution may start at $\log(m_W^2)$. However, it starts with a rising behaviour. This behaviour can be explained if we recall that there is $\sin(\theta/2)$ factor in the matrix element to emit a transverse vector boson. Though there may be longitudinal $W$-bosons to propagate in $t$-channel, the figure shows that this process is dominated by the fusion of transverse $W$'s. The 'typical' configuration is shown in Fig. 4.12. This picture is consistent with the energy distributions of the final state particles in Fig. 4.13.

Now we show several distributions at $\sqrt{s} = 1$ TeV which will be necessary to discuss these processes as backgrounds. The qualitative character is the same at 500 GeV or at 1.5 TeV. The whole curve will be shifted upwards as we raise the c.m. energy.

The first one is the energy distribution of the vector bosons (Fig. 4.14). The general behaviour is just the one discussed above for each processes. The transverse momentum distribution of the vector bosons is shown in Fig. 4.15. The typical $p_T$ for $e^+e^-Z$ is of order electron mass, while it is of order $W$-boson mass for $e^\pm\nu_e(\bar{\nu}_e)W^\mp$ and $\nu_e\bar{\nu}_e Z$. Due to the large cross section of these processes, the large $p_T$ component is still sizable at TeV energies.

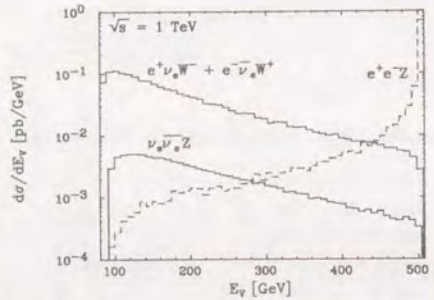


Figure 4.14: Energy distribution of the vector bosons in the single weak boson production processes at c.m. energy 1 TeV.

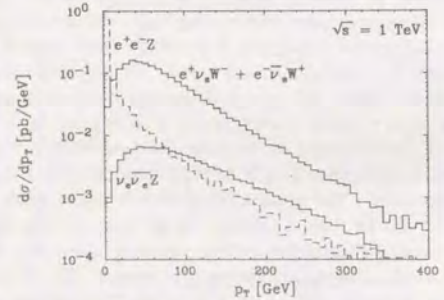


Figure 4.15: Transverse momentum distribution of the vector bosons in the single weak boson production processes at c.m. energy 1 TeV.



# Chapter 5

# Higgs Boson Production

The search for the Higgs boson and the detailed study of its character is, undoubtedly, the main goal of the TeV linear collider. In this chapter, we discuss the production processes of the Higgs boson in the Standard Model, with the zero-width approximation. Though the use of the zero-width approximation cannot be justified for resonances with large widths, it gives us qualitative idea of the production cross section and the distributions of the final state particles when the resonance is produced. For heavy Higgs bosons above 500 GeV, the result using the zero-width approximation should be regarded only as a guide. However, for lighter Higgs bosons, the width is indeed smaller than 10% of its mass, and the approximation can be justified if we are not interested in the detailed threshold behaviours.

The whole process, including the decay of the Higgs boson into $W^+W^-$, $ZZ$ and $t\bar{t}$ is discussed in Chap. 6 and 7. The results in this chapter will be useful when we discuss the cuts which will reject the 'continuum' background while retaining most of the signal. There is one more advantage to know the Higgs boson production process without its decay; one can make the consistency check of the results of the later chapters.

## 5.1 Physics Interests in the Processes

All the discussions on the Higgs production in this chapter is based on two assumptions. (1) The minimal structure of the Higgs sector, and (2) zero-width approximation for the Higgs boson.

The production of the Higgs boson heavily depends on the parameters of the Higgs sector. However, there are some reasons to concentrate on the minimal Higgs sector. First of all, it is the simplest solution to produce gauge boson masses. Secondly, the constraint from the $\rho$-parameter requires that the largest portion of the $SU(2)_L \times U(1)_Y$ breaking order parameter belongs to the representation (2, 1/2). Thus, the assumption of the "doublet" should be, at least, a good approximation. Thirdly, there is a possibility that there are many doublets/singlets which may mix after the symmetry breaking, as expected in the supersymmetric version of the Standard Model. Though it is a very interesting and even exciting possibility, the total cross section to produce *any* kind of Higgs bosons well above their threshold is determined completely from the requirement that they are responsible

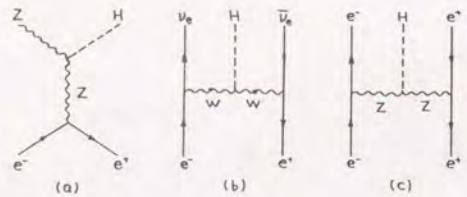


Figure 5.1: Feynman diagrams of the processes (a) $e^+e^- \to ZH$, (b) $e^+e^- \to \nu_e\bar{\nu}_e H$ and (c) $e^+e^- \to e^+e^- H$.

for the weak boson masses $m_W$ and $m_Z$. Thus, we can obtain a good idea even on the non-minimal models by discussing the Higgs boson production in the minimal Standard Model.

### 5.1.1 $e^+e^- \to ZH$

The Higgs hunting for relatively light Higgs bosons will be made mainly using this process. If the Higgs boson is lighter than twice the $W$-boson mass $m_W$, which is called the "intermediate mass" Higgs boson, it mainly decays into a $b\bar{b}$ pair. Thus, the main background will be $ZZ$ if we detect the $Z$ boson by a lepton ($e$ or $\mu$) pair, or both $ZZ$ and $W^+W^-$ if we search through the hadronic mode. If the Higgs boson is heavier than twice the $W$-boson mass, it decays mainly into a $W$-pair, and the continuum production of $W^+W^-Z$ and $ZZZ$ is its main background. This process will be discussed in Chap. 6.

There is only one Feynman diagram (Fig. 5.1(a)) in this process. Since the production occurs via the $s$-channel $Z$-boson exchange, the cross section decreases like $1/s$ as the energy increases. Thus this process is important at relatively low energies. However, its discovery limit for Higgs mass reaches nearly up to $\sqrt{s} - m_Z$ thanks to the two-body phase space.

### 5.1.2 $e^+e^- \to \nu_e\bar{\nu}_e H$

There is again only one Feynman diagram (Fig. 5.1(b)), which is a $t$-channel $W$-boson fusion process. Since the gauge bosons are exchanged in the $t$-channel, it has an increasing cross section as the c.m. energy is increased. The search for the heavy Higgs bosons is mainly done with this process. Since heavy Higgs bosons decay mainly into $W^+W^-$ and $ZZ$, the production of $\nu_e\bar{\nu}_e W^+W^-$, $\nu_e\bar{\nu}_e ZZ$ should be discussed if we go beyond the zero-width approximation. Here, the main background will be $e^+e^-W^+W^-$, $e^+e^-ZZ$, and $e^\pm\nu_e(\bar{\nu}_e)W^\mp Z$. They will be discussed in Chap. 7. If we use the leptonic modes of the $W$, $Z$ decay, the single $W/Z$ production processes discussed in the previous chapter will be serious backgrounds as well.



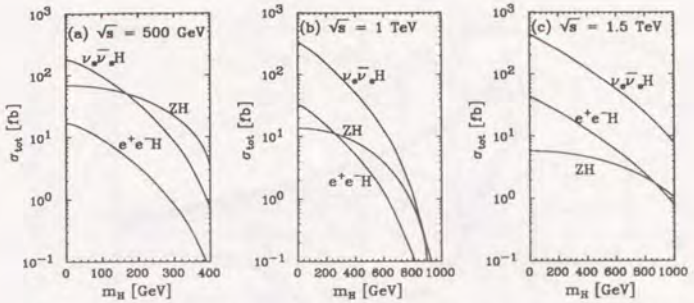


Figure 5.2: Higgs mass dependence of the total production cross sections via the processes $e^+e^- \to ZH$, $\nu_e\bar{\nu}_e H$ and $e^+e^- H$ at c.m. energies (a) 500 GeV, (b) 1 TeV and (c) 1.5 TeV.

### 5.1.3 $e^+e^- \to e^+e^- H$

This process is a $t$-channel $Z$ boson fusion process (Fig. 5.1(c)) where $Z$-boson substitutes the role of the $W$-boson in the previous process. This process has also an increasing cross section at high energy due to the $t$-channel vector boson exchange. If we can tag the electron/positron in the forward region, it will be a quite unambiguous event. The continuum production of $e^+e^-W^+W^-$ and $e^+e^-ZZ$ will be the main (and large!) background.

## 5.2 Cross Sections and Distributions

We first show the total cross section of the processes $e^+e^- \to ZH$, $\nu_e\bar{\nu}_e H$ and $e^+e^- H$ in Fig. 5.2 at three energies, (a) $\sqrt{s} = 500$ GeV, (b) 1 TeV and (c) 1.5 TeV. One general character at all energies is that the $t$-channel processes drop more rapidly than the $ZH$ production as the mass of the Higgs boson is increased. The reason is that the two-body phase space behaves like $\propto \beta$ near the threshold where $\beta$ is the velocity of the final state Higgs boson, while the total cross section of the $\nu_e\bar{\nu}_e H$ and $e^+e^- H$ behave like $\beta^5$ near the threshold where the factor of $\beta^3$ comes from the three-body phase space and another factor of $\beta^2$ from the soft eletron/neutrino wavefunction.

The $ZH$ production has cross sections which decrease with $s$, while $\nu_e\bar{\nu}_e H$ production has increasing cross section. The $\nu_e\bar{\nu}_e H$ cross section is larger for a light Higgs boson already at $\sqrt{s} = 500$ GeV. This light Higgs boson decays into $b\bar{b}$, which resembles to its two-photon production. However, it may be detectable by applying a cut on the transverse momentum of the $b$- and $\bar{b}$-jets [33,34]. The situation will be much better by the introduction of a sophisticated vertex detector by tagging $b$-events. For the heavier Higgs boson which decays into $W^+W^-$, the cross section of $ZH$ production is larger than that of $\nu_e\bar{\nu}_e H$. Thus the Higgs hunting at $\sqrt{s} = 500$ GeV can be performed both by $ZH$ and $\nu_e\bar{\nu}_e H$ production. At higher energy $\sqrt{s} = 1$ TeV, the $\nu_e\bar{\nu}_e H$ cross section is larger for almost all masses of the

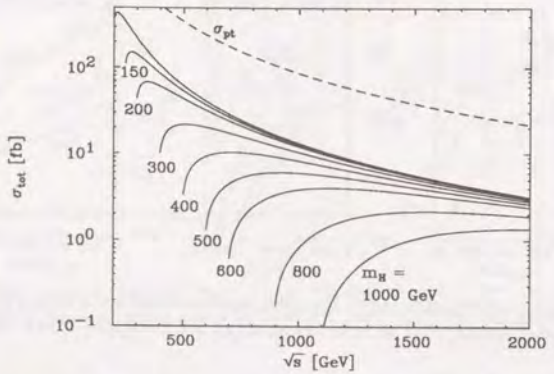


Figure 5.3: Total cross section of the process $e^+e^- \to ZH$ for various mass of the Higgs boson.

Higgs boson. However, even at this energy, the $ZH$ production will play an important role to serve a cross-check to establish the Higgs boson.

Now we discuss the distributions of the final state particles separately.

### 5.2.1 $e^+e^- \to ZH$

As discussed in the beginning of this section, this process is indeed the most important process at a $\sqrt{s} = 500$ GeV collider, and will also be useful at $\sqrt{s} = 1$ TeV.

We show first the energy dependence of the total cross section for various Higgs boson masses in Fig. 5.3. One observes that the cross section reaches the asymptotic curve rapidly above the threshold. The point cross section $\sigma_{\rm pt}$ is shown for comparison. All curves drop like $1/s$ at high energy.

The differential cross section $\mathrm{d}\sigma/\mathrm{d}\cos\theta$ is in Fig. 5.4. We observe that almost all events occur at large angles. The reason is very simple. Recall that the coupling between the $Z$-boson and the Higgs boson comes from the Lagrangian density

$$\mathcal{L} = \frac{1}{2} g_Z m_Z H Z^\mu Z_\mu, \tag{5.1}$$

which has a dimensionful coupling constant $g_Z m_Z$. Here $g_Z$ is defined by $g_Z = e/\sin\theta_W \cos\theta_W$. From the naive dimensional analysis, processes including the dimensionful coupling constant die away very rapidly at high energies. However, this discussion is too naive, and the dimensionful coupling constant can be cancelled by the $1/m_Z$ factor in the $Z$-boson polarization vector only for its longitudinal component. Thus at a high enough energy, almost no transverse $Z$-bosons are produced, following the naive dimensional analysis argument, and only



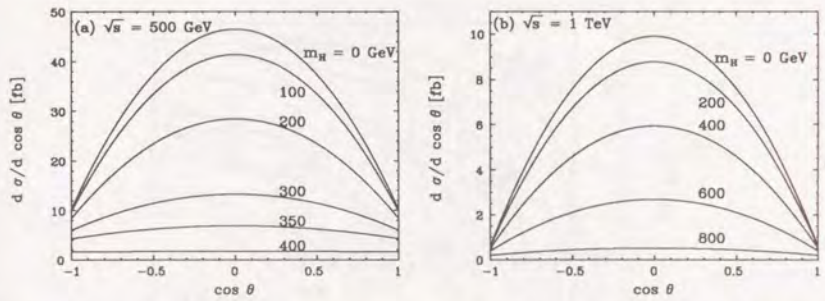


Figure 5.4: Angular distribution in the process $e^+e^- \to ZH$, at c.m. energy (a) 500 GeV and (b) 1 TeV.

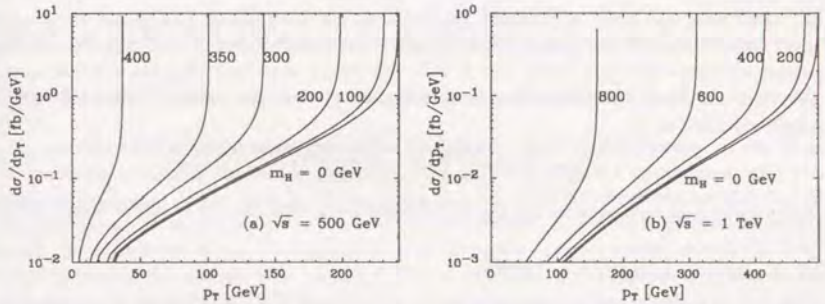


Figure 5.5: Transverse momentum distribution in the process $e^+e^- \to ZH$ at c.m. energy (a) 500 GeV and (b) 1 TeV.

the longitudinal $Z$-bosons remain. Then the final state has zero-helicity, where Higgs boson does not have any helicities and $Z$-boson is longitudinal, which gives a $d$-function proportional to $\sin\theta$. In other words, $Z$ and $H$ cannot be produced into the forward direction due to angular momentum conservation. One can clearly observe this trend comparing the figure at (a) 500 GeV and (b) 1 TeV, where the contribution of the transverse component in the forward region will indeed die away.

The transverse momentum distributions have Jacobian peaks (Fig. 5.5) due to the two-body kinematics. The peak position is easily obtained by simple kinematics:

$$p_T|_{\rm peak} = \frac{\sqrt{s}}{2}\sqrt{1 - 2\,\frac{m_H^2 + m_Z^2}{s} + \frac{(m_H^2 - m_Z^2)^2}{s^2}}\,. \tag{5.2}$$

These Jacobian peaks will be one of the clue to the Higgs hunting. There is one more

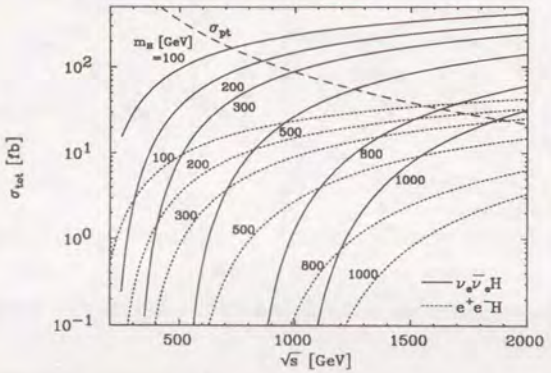


Figure 5.6: Total cross sections of the processes $e^+e^- \to \nu_e\bar{\nu}_e H$ and $e^+e^- H$ for various $m_H$.

important clue from the simple two-body kinematics, that the energy of the $Z$-boson is completely fixed to be

$$E_Z = \frac{\sqrt{s}}{2}\left(1 + \frac{m_Z^2}{s} - \frac{m_H^2}{s}\right), \tag{5.3}$$

which can appear as a peak in the $E_Z$ distribution even with the decay of the Higgs boson.

### 5.2.2 $e^+e^- \to \nu_e\bar{\nu}_e H$ , $e^+e^- H$

As discussed in the beginning of this section, the $\nu_e\bar{\nu}_e H$ production will be the main place to study the Higgs boson production at high energy. We show the energy dependence of the total cross section for various $m_H$ in Fig. 5.6. One observes the increasing cross section.

The cross section of $e^+e^- H$ is always by a factor of 10 smaller than that of the $\nu_e\bar{\nu}_e H$, though the dependence on $m_H$ is almost the same. This can be understood by the smaller coupling of the $Z$-boson to the electron compared to the $W$-boson. The coupling factor for $\nu_e\bar{\nu}_e H$ final state is

$$\left[\left(\frac{g_W}{\sqrt{2}}\right)^2 (g_W m_W)\right]^2, \tag{5.4}$$

since only the left-handed electron and right-handed positron contribute, while for $e^+e^- H$ all helicities contibute to give

$$\left[g_Z^2 (g_Z m_Z)\right]^2 \left[\left(-\frac{1}{2} + \sin^2\theta_W\right)^4 + 2\left(-\frac{1}{2} + \sin^2\theta_W\right)^2 (\sin^2\theta_W)^2 + (\sin^2\theta_W)^4\right]. \tag{5.5}$$



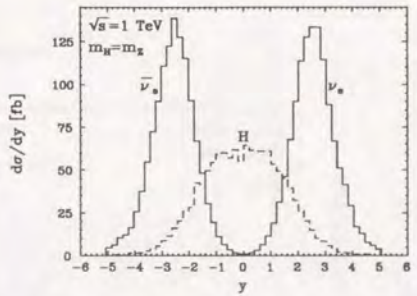


Figure 5.7: Pseudo-rapidity distribution in the process $e^+e^- \to \nu_e\bar{\nu}_e H$ at c.m. energy 1 TeV, where the mass of the Higgs boson is set to be equal to $m_Z$.

There is an additional factor from the $W_L$ and $Z_L$ luminosity functions both from the electron and positron current, which behave like $(s/m_W^2)^2$ and $(s/m_Z^2)^2$ respectively. These factors of the luminosity functions cancel the $WWH$ and $ZZH$ couping constants $g_W m_W$ and $g_Z m_Z$ precisely. Then these factors combine to give the ratio of 9.4, which is roughly correct.

To see the typical event shape, we show the pseudo-rapidity distribution of the final state particles for $\nu_e\bar{\nu}_e H$ for $m_H = m_Z$ and $\sqrt{s} = 1$ TeV in Fig. 5.7 to compare with the process $e^+e^- \to \nu_e\bar{\nu}_e Z$ discussed in the previous chapter. The distributions for the $e^+e^- H$ final state does not show any difference and hence omitted. These distributions show the typical characteristics of the $W$-boson fusion or $Z$-boson fusion process, which are very similar to that of the process $e^+e^- \to \nu_e\bar{\nu}_e Z$ (Fig. 4.10). The typical pseudo-rapidity of the final leptons are of the order $(1/2)\log(s/m_V^2)$, where $m_V = m_W$ or $m_Z$ which does not make any difference. The Higgs boson is produced centrally.

The energy distributions of the final state particles (Fig. 5.8) is consistent with the naive picture of the $W$-fusion as well. Both the final $\nu_e$ and $\bar{\nu}_e$ favour larger energies, while the Higgs is produced with low energy to make the denominator of the $t$-channel $W$-boson as small as possible.

The distribution of the logarithm of the $t$-channel virtuality $|t| + m_W^2$ is shown in the Fig. 5.9. There is one difference with the case $\nu_e\bar{\nu}_e Z$, that the curve immediately starts decreasing at the boundary $\log(m_W^2)$. This fact shows that there does not appear the factor $\sin(\theta/2)$ discussed in Chap. 3 and 4, which was the consequence of the helicity selection rule and the angular momentum conservation. Here, the absence of the $\sin(\theta/2)$ factor is reasonable, since the $W$ or $Z$ bosons exchanged in the $t$-channel is mainly longitudinal, which does not violate the angular momentum conservation even in the strictly forward direction.

The characteristics in the above discussion does not change at all for any value of $m_H$. We show two examples. The first one is the energy $E_H$ distribution, which we show for

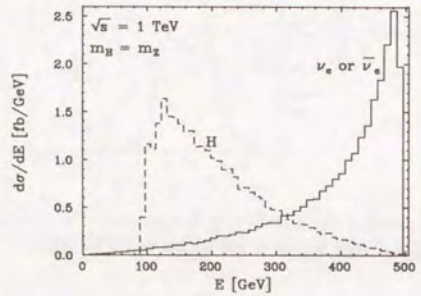


Figure 5.8: Energy distributions in the process $e^+e^- \to \nu_e\bar{\nu}_e H$.

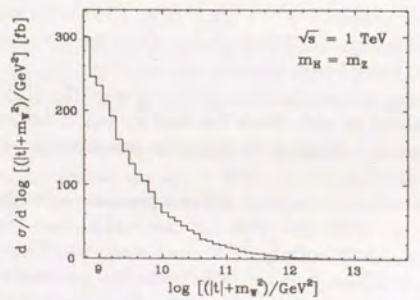


Figure 5.9: Distribution of the logarithm of the denominator in the $t$-channel $W$-boson propagator.



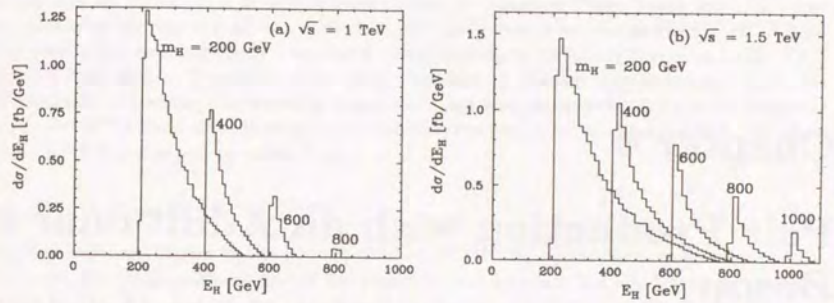


Figure 5.10: $E_H$ distributions in the process $e^+e^- \to \nu_e\bar{\nu}_e H$ at c.m. energy (a) 1 TeV and (b) 1.5 TeV.

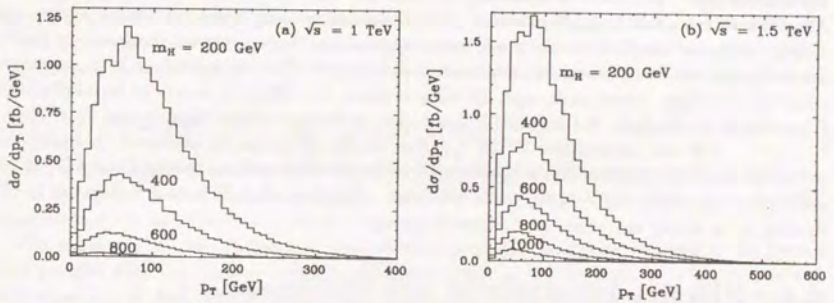


Figure 5.11: Transverse momentum distribuion of the Higgs boson in the process $e^+e^- \to \nu_e\bar{\nu}_e H$ at (a) 1 TeV and (b) 1.5 TeV.

various $m_H$ at $\sqrt{s} = 1$ TeV and 1.5 TeV (Fig. 5.10). The Higgs boson is always produced softly, however with typical $p_T$ of the order $O(m_V)$ as seen below.

The second one is the transverse momentum distribution shown in Fig. 5.11, which demonstrates that the typical $p_T$ is of the order $O(m_V)$. This fact supports the expectation that typical $p_T$ is determined by the 'mass' of the particles exchanged in the $t$-channel, as we discussed in Chap 3. and 4.

Summarizing these distributions, we expect that the decay products have peaks in the energy distribution around $E \sim \sqrt{(m_H/2)^2 + p_T^2}$ with substantial acoplanarity due to the $p_T(H) \sim O(m_W)$.

# Chapter 6

# Pair Production with an Additional $Z$ Boson

We discuss $O(\alpha^3)$ processes in this chapter, with the final state of $W^+W^-Z$, $ZZZ$ and $t\bar{t}Z$. All of these are annihilation processes, which have decreasing cross section at asymptotic energy. However the three-body phase space approaches the asymptotic region very slowly, hence the cross section is maximum at sub-TeV energies. Our main concern is to detect the effect of the Higgs boson exchange. In all processes, the effect is found to be negligible if Higgs boson is off-shell. For on-shell Higgs boson exchange, where Higgs boson is produced by $e^+e^- \to ZH$ and decays into $W^+W^-$, $ZZ$ or $t\bar{t}$, the effect can be observed. Longitudinal polarization of the electron beam significantly improves S/N ratio in the final state $W^+W^-Z$ and $ZZZ$ by a factor of $\sim 100$, while selection of top quark helicities is necessary in $t\bar{t}Z$ final state to study the effect of Yukawa coupling.

## 6.1 Physics Interests in the Processes

All processes in this class have a Higgs boson exchange diagram, where the $ZH$ production is followed by the decay of the Higgs into $W^+W^-$, $ZZ$ or $t\bar{t}$. Recall that the $ZH$ production is the main source of the Higgs boson at $\sqrt{s} = 500$ GeV, and is still important at higher energies. Then the other diagrams will be the main "continuum" background to Higgs hunting, and it is important to understand this "continuum" background completely.

There is a subtlety in the notion of the "continuum". Since the theory of the spontaneously broken gauge theory cannot be perturbatively renormalizable without the Higgs boson, the naive computation omitting the Higgs boson exchanges may lead to some inconsistencies. The famous example is the $WW$ scattering [35], where the tree-level amplitudes will violate the unitarity at high energy if we omit the Higgs boson exchanges. The "continuum" should be regarded as a reference which has a completely safe high-energy limit. Thus, we should understand that the case with massless Higgs boson *is* the "continuum" when we discuss the vector boson fusion processes like $e^+e^- \to \nu_e\bar{\nu}_e W^+W^-$. It is not as clear in the case of the processes discussed in this chapter. We discuss the case first where the Higgs boson exchange is omitted in the unitarity gauge as the "continuum", however



it may not be correct if it is very different from the massless Higgs boson case. It turns out that whether $m_H = 0$ or $m_H = \infty$ does not make any difference to the $W^+W^-Z$ final state, while the massless Higgs boson acts ***constructively*** to the other diagrams in the $ZZZ$ and $t\bar{t}Z$ final states. Thus we can be quite confident to discuss the case $m_H = \infty$ as the "continuum". However, the massless Higgs exchange acts ***desctructively*** to other diagrams in the $W^+W^-Z$ final state if we polarize the electron beam to be right-handed. We show both $m_H = 0$ and $m_H = \infty$ cases there.

### 6.1.1 $e^+e^- \to W^+W^-Z, ZZZ$

There is another interest in the process $e^+e^- \to W^+W^-Z$; this is the lowest order process where the four-point self-coupling of the vector bosons appears. See the Feynman diagrams shown in Fig. 6.1. Indeed, we have found a delicate cancellation between the diagrams for the longitudinal vector bosons. This may serve as another place to study the possible compositeness of the $W/Z$ bosons.

The process $e^+e^- \to ZZZ$ has only the familiar couplings between the electron and the $Z$ boson (Fig. 6.2). There will be no other interests than the Higgs search in this process.

The three vector boson production processes were discussed by Barger, Han and Phillips [36] in detail, though they didn't go further to discuss the observability of the Higgs boson.

### 6.1.2 $e^+e^- \to t\bar{t}Z$

The Feynman diagrams are shown in Fig. 6.3. They fall into three gauge-invariant subsets. One is the initial state $Z$-boson radiation diagrams, the second is the final state $Z$-boson emission, and the last one is the Higgs boson exchange.

The process $e^+e^- \to t\bar{t}Z$ has not been discussed so far. Since this process is the lowest order process with the Yukawa coupling, the sensitivity to the Yukawa coupling is here the main concern. In fact, this is almost the unique place to study the effect of the Yukawa coupling at $\sqrt{s} = 500$ GeV, except the detailed study at threshold region of the $t\bar{t}$ production. For higher energies, combined analysis together with $e^+e^- \to \nu\bar{\nu}t\bar{t}$ and $e^+e^-t\bar{t}$ will be necessary.

## 6.2 Cross Sections and Distributions

The total cross section without the Higgs boson contribution is shown in the Fig. 6.4. All processes are $e^+e^-$ annihilation processes, and hence have decreasing cross section at high energy. Here we took the value of the top quark mass to be $m_t = 100$, 150, and 200 GeV for the demonstration. The three-body phase space reaches the asymptotic (massless) phase space only far above the threshold.

Now we discuss each process separately.

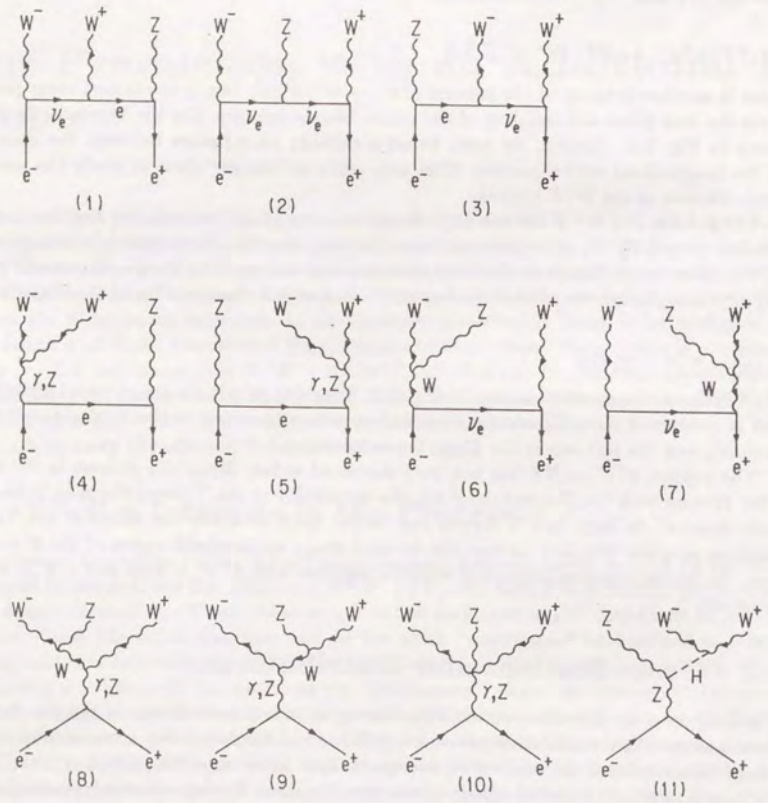


Figure 6.1: Feynman diagrams of the process $e^+e^- \to W^+W^-Z$.



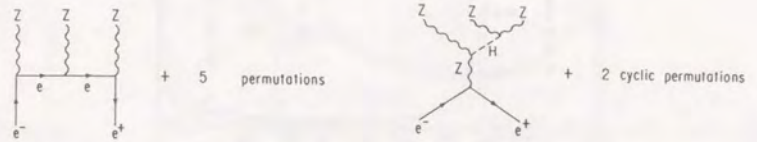


Figure 6.2: Feynman diagrams of the process $e^+e^- \to ZZZ$.

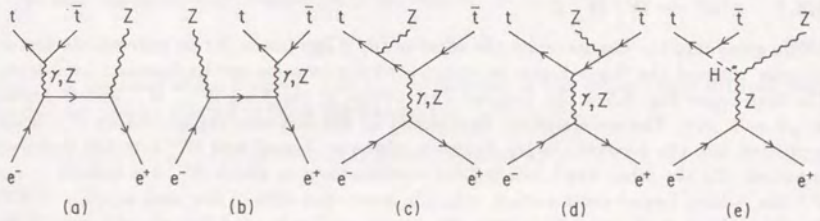


Figure 6.3: Feynman diagrams of the process $e^+e^- \to t\bar{t}Z$.

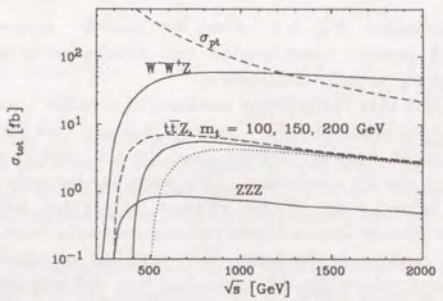


Figure 6.4: Total cross sections of the processees $e^+e^- \to W^+W^-Z$, $ZZZ$ and $t\bar{t}Z$, where the Higgs boson exchange diagrams are omitted.

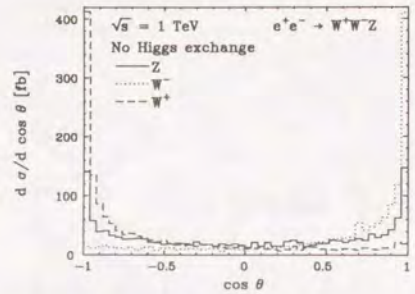


Figure 6.5: Angular distribution in the process $W^+W^-Z$ at c.m. energy 1 TeV. Higgs boson exchange diagrams are omitted.

### 6.2.1 $e^+e^- \to W^+W^-Z$

Before going into the discussion on the effect of the Higgs boson, let us concentrate first on the case without the Higgs boson to understand the 'continuum' background completely. The first figure Fig. 6.5 is the angular distribution of the final $W^+$, $W^-$ and $Z$ bosons at $\sqrt{s} = 1$ TeV. The events occur dominantly in the collinear region, where $W^-$ boson is emitted into the forward (or the direction of the $e^-$ beam) and $W^+$ into the backward direction. On the other hand, the helicity combinations in which $W^-$ has helicity $-$ and $W^+$ has $+$ have largest cross section, which is more than 50% of the total at $\sqrt{s} = 1$ TeV. Recalling the fact that the $W$-bosons can couple to the fermion line directly only if the electron is left-handed, and from the helicity selection rule discussed in Chap. 3 and App. C, we imagine that the dominant configuration is that the $W^-$ is emitted directly from the inital $e^-$, $W^+$ from $e^+$, both collinear. This situation seems to be just the same as in the $W^+W^-$ production.

The energy distribution (Fig. 6.6) of the $W^+$ and $W^-$ shows that they are emitted very energetically. A question arises whether this distribution is consistent with the above picture derived form the angular distribution.

One may anticipate that the collinear emission of a vector boson from the fermion line favours that the vector boson is soft. However, it is not true for massive vector bosons. For the photon emission from an electron line, the soft photon produces the singularity as we encountered in the $Z\gamma$ production. This point can be understood by evaluating the minimum possible value for the off-shell electron propagator, which tells us simply that the soft limit of the photon does not take out any momenta from the electron line, giving completely on-shell electron in the limit. However, this argument does not apply to the massive vector bosons, where the soft limit *does* take out non-zero four-momentum from the electron line to give large virtuality to the off-shell electron line. Let us demonstrate this fact explicitly by evaluating the denominator of the electron propagator as we did in



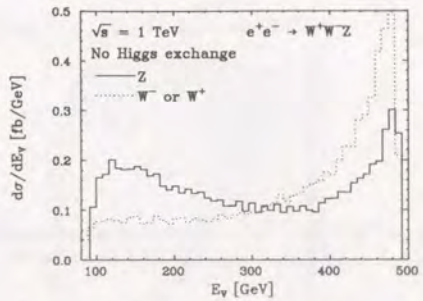


Figure 6.6: The energy distribution.

Chap. 3 and 4.

We take the initial four-momentum of the electron to be

$$k_e^\mu = E(1,\ 0,\ 0,\ 1), \tag{6.1}$$

neglecting the mass of the electron. The four-momentum of the vector boson emitted from the electron can be rotated to lie in the $xz$ plane

$$p_V^\mu = xE(1,\ \beta\sin\theta,\ 0,\ \beta\cos\theta), \tag{6.2}$$

where

$$\beta = \sqrt{1 - \frac{m_V^2}{x^2E^2}}. \tag{6.3}$$

Then the denominator of the electron propagator is [1]

$$\begin{aligned}(k_e - p_V)^2 &= m_V^2 - 2k_e\cdot p_V \\ &= m_V^2 - 2xE^2(1-\beta\cos\theta) \\ &= -2xE^2\beta(1-\cos\theta) - m_V^2\left(\frac{2}{x+\sqrt{x^2 - m_V^2/E^2}} - 1\right).\end{aligned} \tag{6.4}$$

The terms in the last large bracket is a monotonically decreasing function of $x$, which gives the conclusion that the massive vector boson emitted from the electron line favours to be energetic. Since the helicity selection rule will be clearer for the energetic vector boson emissions, the observations on the helicity combination and the energy distribution is completely consistent.

The modest peak in the $E_Z$ distribution at its highest possible energy indicates that the singularity due to the $Z$-boson emission from the initial electron or positron is also

[1] Note that the 'energy fraction' $x$ can be larger than unity in general if the kinematics allows. Indeed, such situations arise in the processes $e^+e^- \to e^+e^-Z$ or $Z\gamma$. However, $x$ is always smaller than unity here.

Figure 6.7: Dalitz plot of the final state $W^+W^-Z$, where the horizontal axis corresponds to $E_Z$ and vertical axis to $E_{W^-}$. The singular region lies along the boundary of the kinematically allowed region. The unit of energy is 100 GeV for both $x$ and $y$ axis.

present, though subdominant. This type of configurations give the small rise in the angular distribution for the backward direction ($W^-$) or forward direction ($W^+$). However, it is clear from the $E_Z$ distribution that the contribution from the lower energy $Z$ boson is much larger than the peak of the energetic $Z$, which is consistent with the much sharper peak of the $E_W$ distribution at its maximum compared to that of the $Z$ boson.

The whole situation is very clear in the Dalitz plot of the final vector bosons (Fig. 6.7), where the dominant configurations appear at the *boundary* of the kinematically allowed region. The three edges correspond to the cases where one of the vector bosons are emitted energetically while the other two forming a small mass running into the same direction with roughly the same energy. The three corners correspond to the cases where two of the vector bosons are emitted energetically from the intial state, and then the two off-shell fermion lines meet to produce a soft vector boson. Both cases are singular from the above discussion on the $t$-channel propagator, and they combine to lie along the boundary in the Dalitz plot.

The typical configuration can be visualized as in the Fig. 6.8. Thus the 'typical' diagrams are just those of the process $e^+e^- \to ZZZ$, which has only the diagrams where the final state vector bosons are attatched to the electron line directly. We can check this point in the next subsection.

The transverse momentum distribution of all three vector bosons is shown in Fig. 6.9.



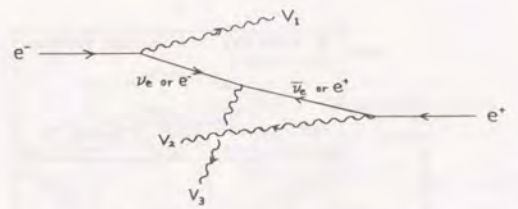


Figure 6.8: Typical configurations in the process $e^+e^- \to W^+W^-Z$, where $V_1$, $V_2$ and $V_3$ corresponds to one of the three vector bosons respectively. Most dominant combination is $V_1 = W^-$, $V_2 = W^+$ and $V_3 = Z$.

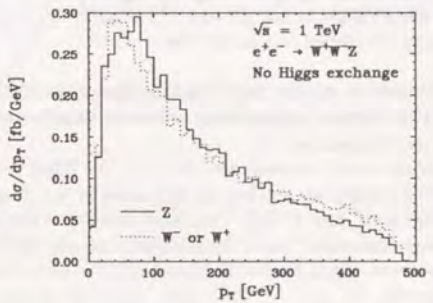


Figure 6.9: Transverse momentum distribution.

The typical $p_T$ is of the order $m_V$, which supports the above picture again since the 'mass' of the $t$-channel electron or neutrino is of the order $m_V^2$.

We discussed in the previous section that there is an interest in this process as the lowest order process which contains the four-point vector boson self-coupling of Fig. 6.1 (8) – (10). In fact, all the diagrams should be included to obtain gauge-invariant results. The correct high-energy behaviour for the longitudinal vector bosons can be assured only after summing all these diagrams where delicate cancellations occur. We show one example in Fig. 6.10, where the $\cos\theta_Z$ distribution is shown for some subsets of the diagrams separately, and their interference term. They are normalized in such a way that they all sum up to give the correct differential cross section. The helicities of the vector bosons are chosen to be all longitudinal to demonstrate the cancellation. The diagrams are separated into three groups. First group includes the diagrams where all three vector bosons are attatched directly to the fermion line (Fig. 6.1 (1) – (3)), which is named AWWZ. The second group A3 includes the diagrams with three-point vector boson self-couplings *with* $t$-channel fermion (Fig. 6.1 (4) – (7)). The last group A4 includes the diagrams Fig. 6.1 (8) – (10), which is summarized as the four-point vertex in the HELAS system. The notations like 'A3/AWWZ'

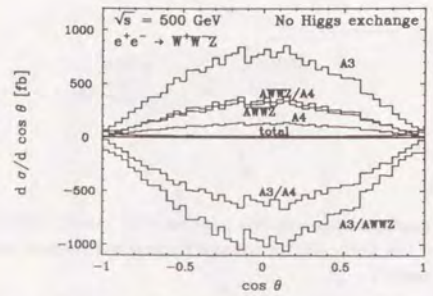


Figure 6.10: $\cos\theta_Z$ distribution in the process $e^+e^- \to W_L^+W_L^-Z_L$, where the contributions from various diagrams are shown separately. See text.

refer to the interference terms. The figure clearly shows the delicate cancellations among the three groups. This delicate cancellation will lead to a large sensitivity to the vector boson self-coupling in this process.

Now we come to the main interest, the effect of the Higgs boson exchange. We show the dependence of the total cross section on the mass of the Higgs boson in Fig. 6.11, at the energy $\sqrt{s} = 500$ GeV and 1 TeV. One first observes that there is almost no effect below the Higgs decay threshold ($m_H < 2m_W$), which means that the off-shell Higgs boson exchange is not important. Even above the threshold, the cross section will not get affected drastically, especially for the $\sqrt{s} = 1$ TeV case. Thus we should find an efficient way to single out the Higgs boson signal by applying cuts.

The angular distribution of $Z$ boson is plotted for various $m_H$ in Fig. 6.12. The forward peak receives little effect from the Higgs boson exchange, while the large angle cross section is substantially increased at $\sqrt{s} = 500$ GeV. This observation is completely consistent with the $ZH$ production discussed in Sect.5.2. We expect that the signal can be made clear by applying a cut on $\cos\theta_Z$. On the other hand, the effect is hardly visible at $\sqrt{s} = 1$ TeV.

The peaks in the $m_{WW}$-distribution (Fig. 6.13) are clearly seen at $\sqrt{s} = 500$ GeV, after applying the cut $|\cos\theta_Z| < 0.85$. We can observe the effect near to its kinematical limit of the Higgs boson production. The situation is much worse for $\sqrt{s} = 1$ TeV. The peak of the Higgs boson below $m_H < 400$ GeV is quite clear, however the peak of 600 GeV Higgs is hardly seen. Here we show the energy distribution of the $Z$ boson as well in Fig. 6.14 since it is experimentally simpler to measure, although it is equivalent to the $m_{WW}^2$ distribution due to the relation

$$E_Z = \frac{\sqrt{s}}{2}\left(1 - \frac{m_{WW}^2}{s}\right) \tag{6.5}$$

The transverse momentum distribution Fig. 6.15 has also the Jacobian peak due to the two-body kinematics of the $ZH$ production, with the same cuts. Here again the peaks at $\sqrt{s} = 1$ TeV is not clear.



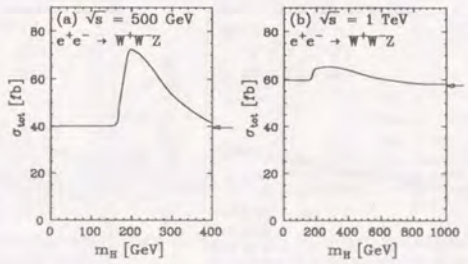


Figure 6.11: Higgs mass dependence of the total cross section at two energies, (a) 500 GeV and (b) 1 TeV. The arrows indicate the cross section where the Higgs exchange diagram is omitted ($m_H = \infty$).

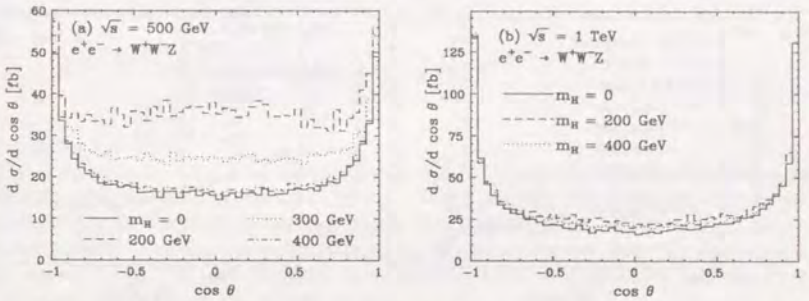


Figure 6.12: $\cos\theta_Z$ distribution with various mass of the Higgs boson at c.m. energy (a) 500 GeV and (b) 1 TeV.

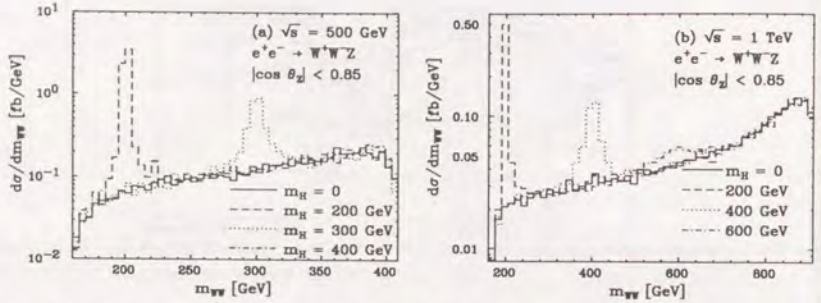


Figure 6.13: The invariant mass distribution of $W^+W^-$ system with various mass of the Higgs bosons at c.m. energy of (a) 500 GeV, (b) 1 TeV. A cut on the angle of $Z$ boson $|\cos\theta_Z| < 0.85$ is applied.

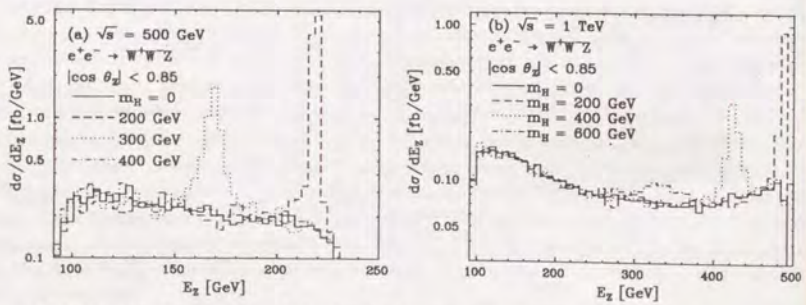


Figure 6.14: Energy distribution of the final $Z$-boson with various mass of the Higgs boson after the $|\cos\theta_Z| < 0.85$ cut, at c.m. energy of (a) 500 GeV and (b) 1 TeV.



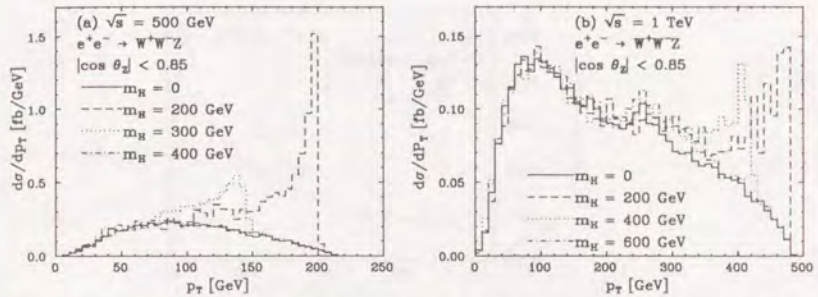


Figure 6.15: Transverse momentum distribution of the $Z$ boson with various mass of the Higgs boson after the $|\cos\theta_Z| < 0.85$ cut, at c.m. energy (a) 500 GeV and (b) 1 TeV.

To make the signal clearer at $\sqrt{s} = 1$ TeV, one may try to cut off the 'typical' continuum production process of Fig. 6.8 where the $W^-$ and $W^+$ are emitted collinearly, by applying cut on the angles of all three vector bosons. However, we have checked that the triple cut does not make the situation better. Since the cross section of the continuum production is huge compared to that of the $ZH$ production, the tails for larger angles are still sizable. Here we propose the following way which is motivated from the understanding on the 'continuum' background obtained above. We can throw away the $W$-boson emission from the electron line, which is the dominant configuration which has nothing to do with the Higgs boson, without loosing much of the signal, by longitudinally polarizing the electron beam to be right-handed. Then the diagrams of Fig. 6.1 (1) – (3) and (6), (7) will be simply absent, while the signal (11) is almost the same! In fact, the $ZH$ production will be reduced only by the factor

$$\frac{\left(-\frac{1}{2}+\sin^2\theta_W\right)^2+(\sin^2\theta_W)^2}{2(\sin^2\theta_W)^2}=1.19 \qquad (6.6)$$

by polarizing the beam.

The distributions of the final state particles will be completely different from the case of the unpolarized beam. Let us again discuss the case without the Higgs boson exchange first. Note that for the positive chirality sector, the Feynman diagrams fall into two gauge-invariant subsets. The first one is the initial state $Z$-boson radiation from the electron line (diagrams of Fig. 6.1 (4) and (5)), and the other is the final state $Z$-boson emission from the $W$-boson (diagrams of Fig. 6.1 (8) – (10)).

From the discussions on the $t$-channel electron propagator at the beginning of this section, we can deduce the final state distributions for the first gauge-invariant subset. Here, the $Z$-boson is emitted from the initial state energetically, and the off-shell electron collides with the other beam to produce the $W^-W^+$ pair. Indeed, the sharp peak in the $E_Z$ distribution Fig. 6.16 at very high energy corresponds to this subset. The $W^+$ and $W^-$

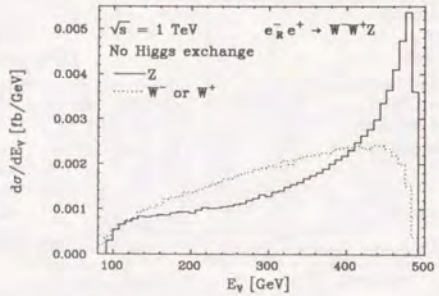


Figure 6.16: Energy distribution of the final vector bosons where the electron beam is longitudinally polarized to be right-handed.

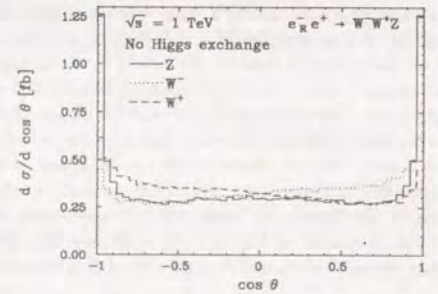


Figure 6.17: Angular distribution when the electron beam is longitudinally polarized to be right-handed.

tends to run into the same direction with a very energetic $Z$-boson in the other side, which can be checked in the scatter plot though we do not show it here. The whole picture is consistent with the angular distribution in the Fig. 6.17, where the forward peak is sharp only for the $Z$-boson, where both $W^+$ and $W^-$ are produced relatively larger angles. The small forward-backward asymmetry seems to be an effect of the $s$-channel process of the second subset.

For the second subset, where the $W^+W^-$ pair creation occurs and the $Z$-boson is emitted from one of them, we discuss its distribution by considering the $s$-channel propagator of the $W$-boson. The denominator of the $W$-boson propagator is simply the invariant mass of the $W/Z$ system minus squared $W$-boson mass, and the amplitude will be maximized if the invariant mass of the $W/Z$ system is minimized. This condition is equivalent to the requirement that the energy of the other $W$-boson is maximum. However this process does



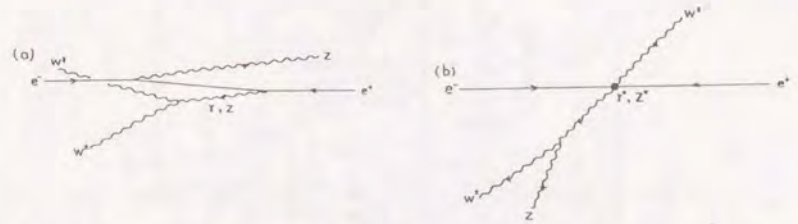


Figure 6.18: Two typical configurations of the process $e^+e^- \to W^+W^-Z$ from right-handed electron beam. The configuration of (a) initial state $Z$-boson emission is dominant, while the configuration of (b) final state emission is subdominant.

not seem to be dominant as seen from the $E_W$ distribution in Fig. 6.16. The contributions from both subsets are summarized in the Fig. 6.18.

The longitudinal polarization selecting the positive chirality sector to kill the initial state radiation of the $W$-bosons is really very effective. We show its dramatic effect in the Fig. 6.19, where the total cross section is plotted again for varying $m_H$. One sees that the effect of the Higgs boson is very clear compared to the unpolarized case. Even a Higgs boson with 600 GeV mass will enhance the cross section substantially.

We show the $m_{WW}$ distribution first in Fig. 6.20, again after the cut on the $\cos\theta_Z$ for several $m_H$. Even the $m_H = 800$ GeV Higgs boson shows its peak in the distribution. The peak of the $m_H = 600$ GeV Higgs is now very clear, compared to the case of the unpolarized beam. The $E_Z$ distribution (Fig. 6.21) is shown with the same cut. Here, we observe that the contribution of the massless Higgs boson is desctructive to the other diagrams, comparing the curves $m_H = 0$ and $m_H = \infty$. We do not have any idea yet whether this cancellation is required from the unitarity.

The Jacobian peaks in the $p_T(Z)$ distribution (Fig. 6.22) is very clear now as well.

### 6.2.2 $e^+e^- \to ZZZ$

We discuss the distributions for the process $e^+e^- \to ZZZ$, though it should be already clear to the careful readers what kind of distributions are expected. Since there are only diagrams where the final $Z$-bosons are directly attached to the electron line, the situation is just the same as the 'typical' diagrams in the case of $e^+e^- \to W^-W^+Z$.

We show first the angular distribution of the $Z$ bosons (Fig. 6.23). Here, the curve is normalized in such a way that the integration over $-1 \le \cos\theta \le 1$ gives three times the total cross section, or in other words, this is the differential cross section for the any $Z$-boson, first, second or third. We see again the forward and backward peaks which shows

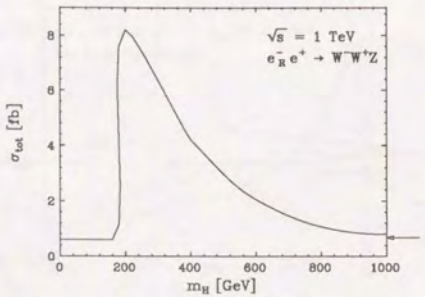


Figure 6.19: Higgs mass dependence of the total cross section from the right-handed electron beam.

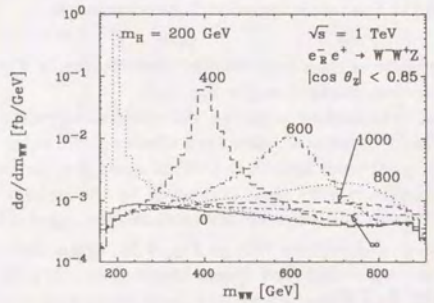


Figure 6.20: Invariant mass distribution of $W^+W^-$ system from the right-handed electron beam. A cut $|\cos\theta_Z| < 0.85$ is applied.

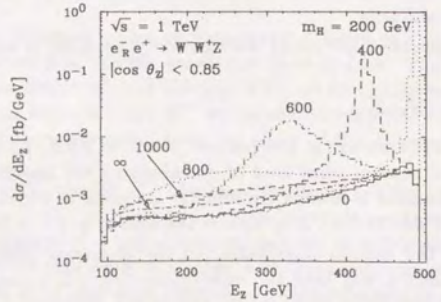


Figure 6.21: Energy distribution of the $Z$ boson after the cut.



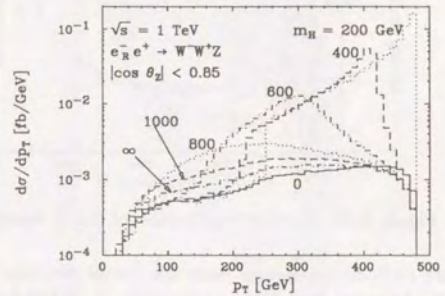


Figure 6.22: Transverse momentum distribution of the $Z$ boson after the cut.

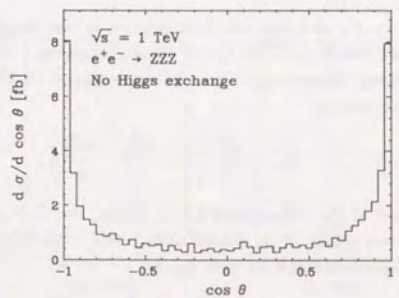


Figure 6.23: Angular distribution of the $Z$ boson in the process $e^+e^- \to ZZZ$.

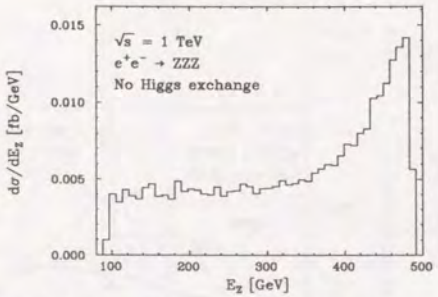


Figure 6.24: Energy distribution of the $Z$ boson.

that the $Z$-bosons are emitted collinearly from the initial electron/positron. The energy distribution (Fig. 6.24) has a peak at high-energy, and a long tail for the lower energies. It is checked that the collinear $Z$ bosons are indeed energetic, and less energetic $Z$-bosons are produced at large angles, by making scatter plots. The helicity combinations favoured are $(+,\ -,\ \pm)$ or $(+,\ -,\ 0)$, where we can interpret that the first two are the $Z$-bosons emitted from the initial state, and the last one is produced softly in the middle. The Dalitz plot (Fig. 6.25) has also dominant region at the boundary of the kinematically allowed region.

Now we come to our main interests, the effect of the Higgs boson exchange. We first show the dependence of the total cross section varying the Higgs boson mass. Thanks (?) to the small cross section of the continuum production, the effect of the Higgs boson is very large (Fig. 6.26). Thus, we expect quite clear peaks in the $m_{ZZ}$, $E_Z$ and $p_T$ distributions after the cuts $|\cos\theta_Z| < 0.85$.

We show the energy $E_Z$ distribution first since it is the simplest to explain. The curves are made after the cuts $|\cos\theta_Z| < 0.85$ for all three $Z$-bosons. The curves shown in Fig. 6.27 have complicated shapes. However, it can be understood in the following way. First, we see the peaks with the energy

$$E_Z = \frac{\sqrt{s}}{2}\left(1 + \frac{m_Z^2}{s} - \frac{m_H^2}{s}\right), \tag{6.7}$$

as discussed at the end of the subsection 5.2.1. Thus, the $Z$-boson with this energy can be regarded as the $Z$-boson which is produced associated with the Higgs boson. Note that the energy of the Higgs boson is fixed as well

$$E_H = \frac{\sqrt{s}}{2}\left(1 + \frac{m_H^2}{s} - \frac{m_Z^2}{s}\right). \tag{6.8}$$

which of course satisfies $E_Z + E_H = \sqrt{s}$.

The other structure is the flat region, which is especially clear in the case $\sqrt{s} = 500$ GeV and $m_H = 200$ GeV. This flat region requires a bit kinematics. Though it is well-known in



Figure 6.25: Dalitz plot of two $Z$ bosons. The unit is in 100 GeV.

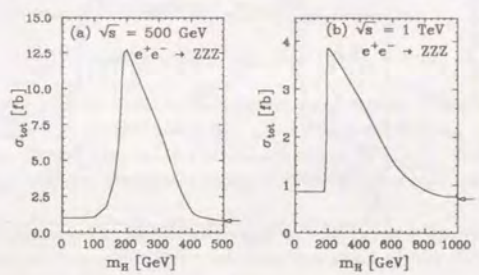


Figure 6.26: Higgs mass dependence of the total cross section at two c.m. energies, (a) 500 GeV and (b) 1 TeV.

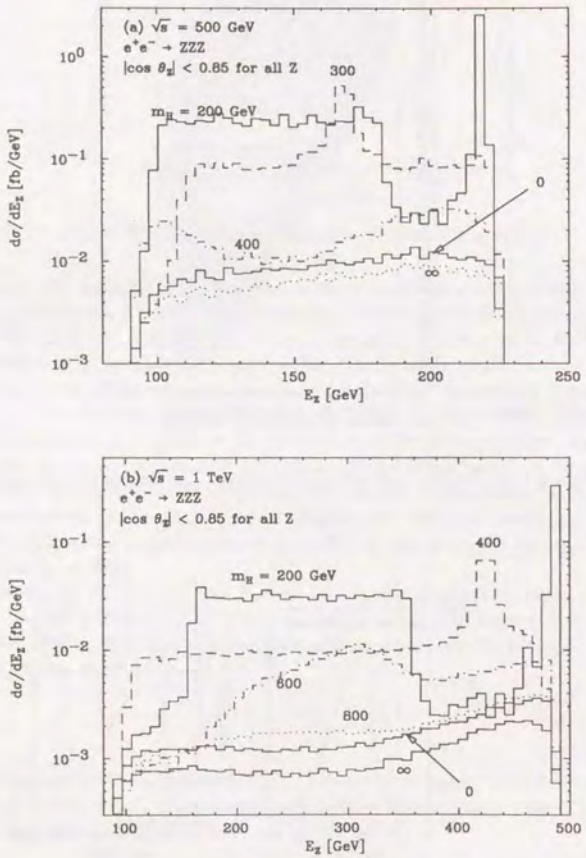


Figure 6.27: Energy distribution of the $Z$ boson after the cut at c.m. energy (a) 500 GeV and (b) 1 TeV. A cut $|\cos\theta_Z| < 0.85$ is applied on all three $Z$ bosons.



the examples like $\tau \to \pi^-\nu_\tau$, let us briefly explain its origin to make the paper self-contained. Recall that both the energies of the $Z$ and $H$ bosons in the $ZH$ production were fixed by the simple kinematics. Then the Higgs decays into two $Z$'s, isotropically in its rest frame, since it carries no spin. The four-momentum of the final $Z$ boson in the Higgs rest frame is

$$\hat{p}_Z^\mu = \hat{E}(1,\ \hat{\beta}\sin\hat{\theta},\ 0,\ \hat{\beta}\cos\hat{\theta}), \tag{6.9}$$

where

$$\begin{aligned} \hat{E} &= \frac{1}{2}m_H \\ \hat{\beta} &= \sqrt{1-\frac{4m_Z^2}{m_H^2}}. \end{aligned} \tag{6.10}$$

The distribution is *flat* in $\cos\hat{\theta}$. Note that $\hat{E}$, $\hat{\beta}$ are both completely fixed by the kinematics. Now we boost the four-momentum to the laboratory frame to give the energy in the laboratory frame

$$E_Z|_{\rm lab} = \gamma\hat{E}(1+\beta\hat{\beta}\cos\hat{\theta}), \tag{6.11}$$

where $\gamma$ and $\beta$ are boost factors

$$\begin{aligned} \gamma &= \frac{E_H}{m_H} \\ \beta &= \sqrt{1-\frac{m_H^2}{E_H^2}}, \end{aligned} \tag{6.12}$$

using $E_H$ defined in eq. (6.8). Since the numbers $\hat{E}$, $\hat{\beta}$, $\gamma$ and $\beta$ are completely fixed above, the only variable is the $\cos\hat{\theta}$, which has a flat distribution. Thus the distribution in $E_Z|_{\rm lab}$ is also flat, since it is only linearly dependent on $\cos\hat{\theta}$, in the region

$$\gamma\hat{E}(1-\beta\hat{\beta}) < E_Z|_{\rm lab} < \gamma\hat{E}(1+\beta\hat{\beta}). \tag{6.13}$$

Now, this structure should be evident to the readers on all curves. They all are composed from a peak and a flat region. In some curves like $\sqrt{s} = 500$ GeV and $m_H = 300$ GeV, they appear at a same region. In the case $\sqrt{s} = 1$ TeV and $m_H = 600$ GeV, both structures are smeared due to the large width. However, the same type of the structures can be seen in all the curves.

We show the invariant mass $m_{ZZ}$ distribution in Fig. 6.28 (a) and (b), again with the cut $|\cos\theta_Z| < 0.85$ for all three $Z$-bosons. Since the invariant mass of two $Z$-bosons is related to the energy of the remaining $Z$-boson $E_Z|_{\rm rem}$ by

$$E_Z|_{\rm rem} = \frac{\sqrt{s}}{2}\left(1+\frac{m_Z^2}{s}-\frac{m_{ZZ}^2}{s}\right), \tag{6.14}$$

the structures discussed above appear here as well.

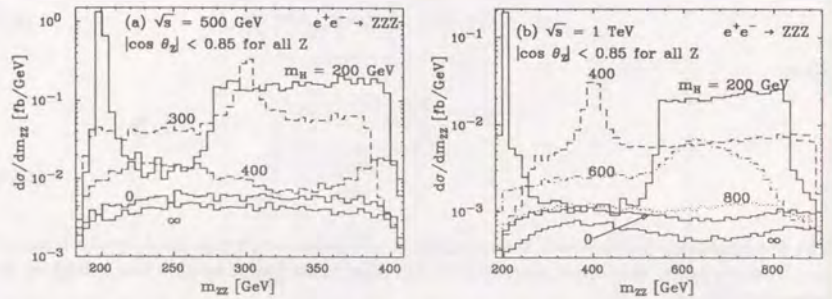


Figure 6.28: Invariant mass $m_{ZZ}$ distribution after the cut at (a) 500 GeV and (b) 1 TeV.

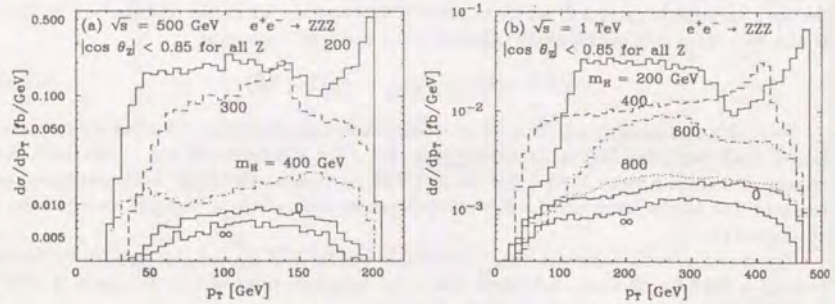


Figure 6.29: Transverse momentum distribution after the cut at (a) 500 GeV and (b) 1 TeV.



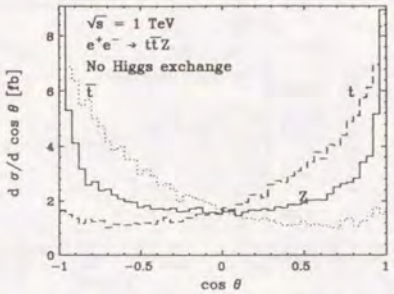


Figure 6.30: Angular distribution for the process $e^+e^- \to t\bar{t}Z$ without the Higgs boson exchange diagram.

The Jacobian peaks in $p_T$ distributions Fig. 6.29 (a), (b) are indeed present. However it may not be as useful as in the case $e^+e^- \to W^-W^+Z$.

Here, one comment follows. Though the search for the Higgs boson through this process $e^+e^- \to ZZZ$ seems to be promising, we should deal with its hadronic decay modes because of the large branching ratio and small total cross section. Then, the background from the continuum $W^-W^+Z$ is also serious here. We cannot expect that the hadron calorimetry may be able to separate the contributions from $W^-W^+Z$ and $ZZZ$, since the cross section of $W^-W^+Z$ is more than one order of magnitude larger than that of $ZZZ$. We should use the possibility discussed in the previous section anyway, to longitudinally polarize the electron beam to be right-handed. We, at present, find no other solutions to this problem.

### 6.2.3 $e^+e^- \to t\bar{t}Z$

We first discuss the general distributions of the final state particles $t$, $\bar{t}$ and $Z$ in the absence of the Higgs boson diagram. Recall that the Feynman diagrams fall into two gauge-invariant subsets, one is the initial state radiation of the $Z$-boson, and the other is the final state emission of the $Z$-boson after the pair-production of the top quark. Careful readers already notice that the situation is just the same as in the $e^+e^- \to W^-W^+Z$ where the electron beam is right-handed. Thus we expect similar distributions.

From the angular distribution Fig. 6.30, we observe the forward and backward peaks in the distribution of the $Z$-boson. We can read off that the gauge-invariant subset of the initial state radiation diagrams is dominant in this region. Here the invariant mass of the $t\bar{t}$ should tend to be low and both $t$ and $\bar{t}$ have a common direction; the energy of the $Z$ boson will be as energetic as possible. This trend is checked in the scatter plot for this subset only. Thus the situation is just the same as the gauge-invariant subset in the $e^+e^- \to W^-W^+Z$ with the right-handed electron beam, where the $Z$-boson is emitted directly from one of the beam, and the off-shell line collides with the other beam to produce a $W^-W^+$ pair.

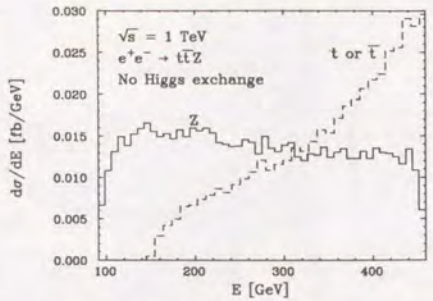


Figure 6.31: Energy distribution.

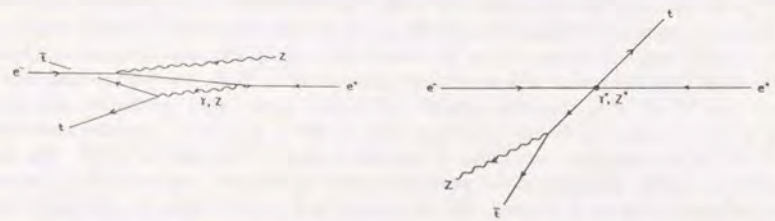

Figure 6.32: Typical configurations for the process $e^+e^- \to t\bar{t}Z$.

However, we see the long tail for the low-energy $Z$-boson in the Fig. 6.31. This part comes from the other gauge-invariant subset of the diagrams with final state $Z$-boson emission. Here, the invariant mass of the $tZ$ or $\bar{t}Z$ will tend to be low to make the denominator of the $s$-channel $t$ (or $\bar{t}$) propagator as small as possible. Thus there appears a peak in the $E_t$ distribution at the highest energy. We can check this idea easily again by making the distributions for the subsets separately. The the forward-backward asymmetry of the top quark in the angular distribution Fig. 6.30 is of the same origin as that of the $t\bar{t}$ production Fig. 3.10, and the magnitude is roughly the same. The situation resembles that of the $e^-e^+ \to W^-W^+Z$ for the right-handed elctron beam again. However, here the contributions from two subsets are comparable, while the initial state $Z$-emission dominated in the $W^+W^-Z$ final state.

Since the effect of the Higgs exchange diagram Fig. 6.3(e) is of our main concern, we show its effect for the total cross section in Figs. 6.33(a) and 6.33(b) for varying Higgs boson mass with three top quark masses $m_t = 100$, 150 and 200 GeV. It is found from the figures that



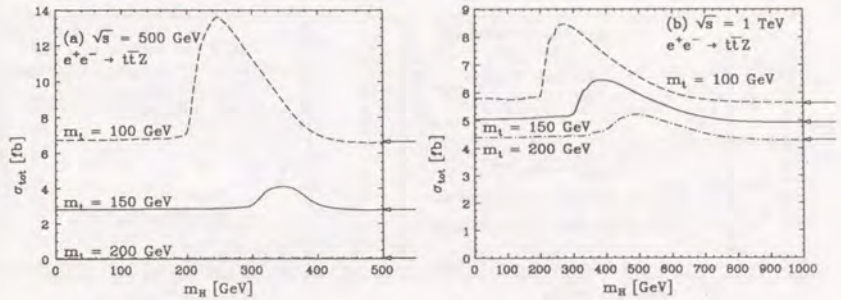


Figure 6.33: Higgs mass dependeces of the total cross section.

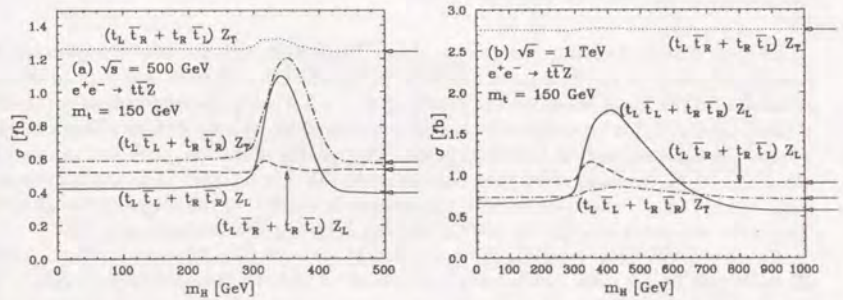


Figure 6.34: Higgs mass dependence of the cross section for various helicity combinations separately. $m_t$ is set to 150 GeV.

its effect is visible only above the $H \to t\bar{t}$ threshold where both the real Higgs production and its subsequent decay into a top quark pair are kinematically allowed. Shown by the arrows are the total cross sections in the absence of the Higgs boson exchange diagram. The virtual effect of the Higgs boson is always negligible. However, it is worth noting that the total cross sections with a light Higgs boson (e.g. $m_H = 0$ values in Figs. 6.33(a) and (b)) are *larger* than those without the Higgs boson shown by the arrows. This indicates that the Higgs boson exchange diagram of Fig. 6.3(e) interferes constructively with the other diagrams above the Higgs pole ($m_{t\bar{t}} > m_H$), while it interferes destructively below the Higgs pole ($m_{t\bar{t}} < m_H$). The effect is, however, negligible quantitatively. Even at $\sqrt{s} = 1$ TeV (Fig. 6.33(b)), the total cross sections with $m_H = 0$ are larger than those without Higgs boson only by the order of 0.1 fb. At $\sqrt{s} = 500$ GeV (Fig. 6.33(a)) for $m_t = 200$ GeV, the Higgs boson effect is nowhere seen because the real production and decay are phase space suppressed.

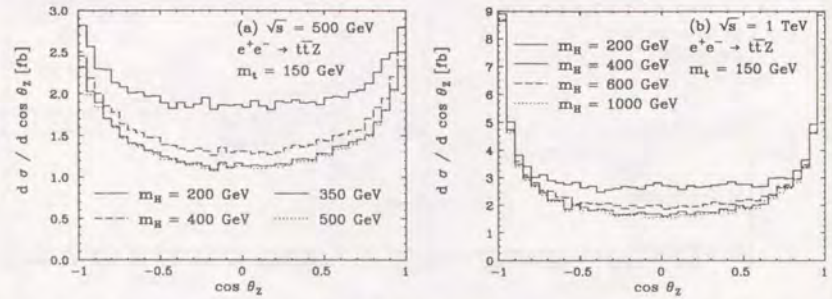


Figure 6.35: Angular distribution of the $Z$ boson with various mass of the Higgs boson at c.m. energy of (a) 500 GeV and (b) 1 TeV.

In Figs. 6.34(a) and (b), the effects of the Higgs-exchange are shown separately for each combination of the final state helicities. Since the effect shows itself only in the real production of the Higgs boson via the process $e^+e^- \to ZH$, only the longitudinal component of the $Z$ boson ($Z_L$) is expected to be sensitive to the effect, at least at high enough energies where $Z_L$ couples strongly to the Higgs boson. The helicity of the top quark and the anti-top quark should be the same since they have to make the $J = 0$ state. Thus the combination $(t_L\bar{t}_L + t_R\bar{t}_R) \cdot Z_L$ is expected to have the largest sensitivity to the Higgs-exchange effect. We fix the top quark mass to be 150 GeV in the following demonstrations.

At $\sqrt{s} = 1$ TeV (Fig. 6.34(b)), the result clearly supports the above expectation. Almost all the Higgs boson mass dependence is confined to the combination $(t_L\bar{t}_L + t_R\bar{t}_R) \cdot Z_L$. The "wrong" combination of the top quark helicities $(t_L\bar{t}_R + t_R\bar{t}_L) \cdot Z_L$ is affected by the Higgs-exchange only through the mixing of the helicities due to the Lorentz-boost from the Higgs boson rest frame (where only the combinations $t_L\bar{t}_L$ and $t_R\bar{t}_R$ can contribute) to the laboratory frame (where all the helicities are defined in the HELAS basis). Its Higgs mass dependence is hence significant only for light enough Higgs bosons where the boost effect is appreciable. The transverse component of the $Z$ boson couples very weakly to the Higgs boson, its dependence on $m_H$ being the same as that of the longitudinal component.

For a lower energy at $\sqrt{s} = 500$ GeV (Fig. 6.34(a)), the sensitivity of the combination $(t_L\bar{t}_L + t_R\bar{t}_R) \cdot Z_T$ is comparable to that of the "right" combination with $Z_L$, $(t_L\bar{t}_L + t_R\bar{t}_R) \cdot Z_L$. The situation can be understood if one examines the kinematics of the $ZH$ production. Here with the Higgs boson heavier than 300 GeV to produce a pair of 150 GeV top quarks, the $Z$ boson is not fully relativistic, and the distinction between its longitudinal and transverse components is not clear in their couplings to the Higgs boson [37].

Since the forward and backward peaks from the initial state $Z$ radiation are not of our main concern, we may apply a cut in $|\cos\theta_Z|$ to make the Higgs boson signal clearer. The fact that only the large angle events have sensitivities to the Higgs-exchange effect is especially clear at the higher energy $\sqrt{s} = 1$ TeV (see Fig. 6.35(b)). A cut $|\cos\theta_Z| < 0.85$



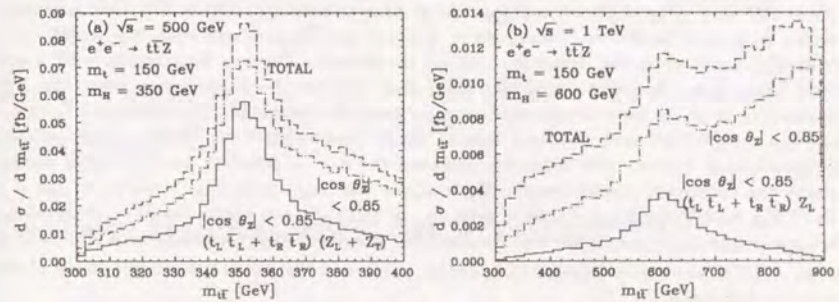


Figure 6.36: The effect of the cuts in $m_{t\bar{t}}$ distributions.

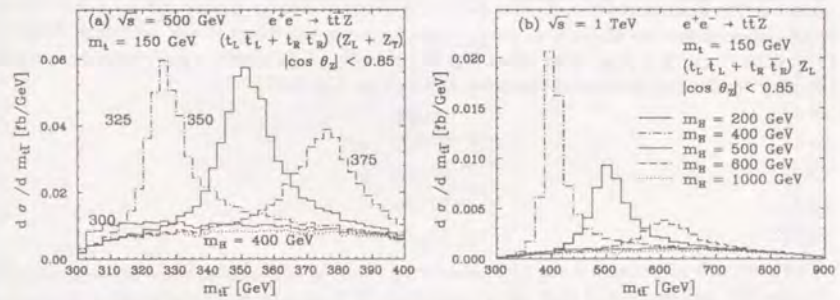


Figure 6.37: Invariant mass distributions of the $t\bar{t}$ system after the cuts.

retains most of the signal while rejecting a major part of the bremsstrahlung $Z$ bosons. This observation is consistent with the $ZH$ production discussed in the previous chapter as well.

From the above considerations, the signal will be made clearer by applying the cut $|\cos\theta_Z| < 0.85$, and simultaneously, by selecting the events with the helicity combinations which are most affected. In Figs. 6.36(a) and (b) we show the effects of these selection criteria for the $m_{t\bar{t}}$ distributions with a Higgs boson contribution. In Fig. 6.36(a) at $\sqrt{s} =$ 500 GeV, the Higgs boson peak with the mass $m_H = 350$ GeV is clearly visible in the distribution, and the peak will be made sharper after the cuts. The situation at a higher energy $\sqrt{s} = 1$ TeV as shown in Fig. 6.36(b) is more drastic, where the peak of the 600 GeV Higgs boson in the total distribution is hardly visible. Only after the selection of the relevant helicities the peak can be made evident.

In Figs. 6.37(a) and (b), $m_{t\bar{t}}$ distributions are shown for various Higgs boson masses after the cut $|\cos\theta_Z| < 0.85$ and the selection of the $t\bar{t}Z$ helicity combinations are applied. At

$\sqrt{s} = 500$ GeV (Fig. 6.37(a)), a Higgs boson with masses 325, 350 or 375 GeV is clearly visible as a peak in the $m_{t\bar{t}}$ distribution, whereas the Higgs boson with $m_H = 300$ GeV is hardly visible since the decay $H \to t\bar{t}$ is not allowed. The $m_{t\bar{t}}$ distribution with a 400 GeV Higgs boson is indistinguishable from that without the Higgs boson since the $ZH$ production is phase space suppressed severely near the threshold. The difference between the $m_H = 400$ GeV and no Higgs case is barely observable if we further single out the longitudinal $Z$ boson. The difference between the $m_H = 300$ GeV and 400 GeV curves shows the constructive interference effects above the Higgs pole ($m_{t\bar{t}} > m_H$). At $\sqrt{s} = 1$ TeV (Fig. 6.37(b)), a Higgs boson of mass below 700 GeV and above the $H \to t\bar{t}$ threshold is appreciable as a peak in the $m_{t\bar{t}}$ distribution. A heavier Higgs boson ($m_H \gtrsim 700$ GeV) is more difficult to observe because of its larger width and the phase space suppression of the $e^+e^- \to ZH$ mode.

It is amusing to note that the positions of the peaks in the $m_{t\bar{t}}$ distributions as shown in Figs. 6.36 and 6.37 are slightly shifted upwards as compared to the real $m_H$. This is a consequence of the destructive interference below the Higgs pole ($m_{t\bar{t}} < m_H$) and the constructive interference above the Higgs pole ($m_{t\bar{t}} > m_H$) between the Higgs boson exchange diagram (Fig. 6.3(e)) and the rest. The effect would probably of academic significance because of the very small cross section of the order of 1 fb (see Fig. 6.33).



# Chapter 7

# Vector Boson Fusion Processes

In this chapter, we discuss the $O(\alpha^4)$ processes where vector bosons are emitted in the $t$-channel from the electron and positron beam, which collide to produce weak bosons or top quarks, in the final state of

$$\begin{aligned} e^+e^- &\to \nu_e\bar{\nu}_e W^+W^-, && (7.1)\\ &\to \nu_e\bar{\nu}_e ZZ, && (7.2)\\ &\to \nu_e\bar{\nu}_e t\bar{t}, && (7.3)\\ &\to e^+e^-W^+W^-, && (7.4)\\ &\to e^+e^-t\bar{t}, && (7.5)\\ &\to e^+e^-ZZ, && (7.6)\\ &\to e^{\pm}\nu_e(\bar{\nu}_e)W^{\mp}Z. && (7.7) \end{aligned}$$

We present total cross sections for all these processes. Our main concern in this chapter is to study the Higgs boson signal and $WW$-scattering in the first two processes. Indeed, we show explicitly that the background from eq. (7.7) can be reduced to the level where we can expect that the hadron calorimetry will be able to separate $\nu_e\bar{\nu}_e W^+W^-$ final state.

## 7.1 Physics Interests in the Processes

The vector boson fusion processes, where photon, $W$ and $Z$ bosons are meant as vector boson, are important processes due to their increasing cross section at high energy. Indeed, we have seen that the cross section of the Higgs production via $W$ boson fusion is indeed increasing with energy, and overcomes that of the lower order process $e^+e^- \to ZH$ below $\sqrt{s} = 1$ TeV. The understanding of the "continuum" is essential in the studies.

The analysis using the exact matrix element have been done only on $e^+e^- \to \nu_e\bar{\nu}_e W^+W^-$ and $e^+e^-W^+W^-$ by Gunion and Tofighi-Niaki [38]. However, even the total cross section has not been known. The other processes have not been discussed at all, except the studies using the effective $W$ approximation.

If the Higgs sector is strongly-interacting, the study of the vector boson scattering is essential to gain information on the sector. These processes serve as the unique place

to study the $J = 0$ sector of the $W^+W^-$ scattering. The process $e^+e^- \to W^+W^-$ can study the $J = 1$ partial wave where techni-$\rho$ like resonances may appear. However, it is possible that there are no light resonances in the $J = 1$ sector, since its existence is not a direct consequence of the Higgs mechanism, and depends on the dynamics of the strongly interacting sector. On the other hand, the $J = 0$, $I = 0$ sector reaches its perturbative unitarity limit very soon, around $m_{WW} \sim 1.2$ TeV. Thus we can expect *some* new physics signal will appear in the $J = 0$ sector below that energy. The $J = 0$ partial waves can be studied at $e^+e^- \to \nu_e\bar{\nu}_e W^+W^-$, $\nu_e\bar{\nu}_e ZZ$, $e^+e^-W^+W^-$ and $e^+e^-ZZ$. Of course, the $J = 1$ partial wave can be studied as well, in the above processes and $e^+e^- \to e^\pm\nu_e(\bar{\nu}_e)W^\mp Z$.

There is one comment in studying the 'continuum' in these processes. It is well known that the vector boson scattering processes do not have the correct high-energy behaviour unless Higgs boson exchange amplitudes are included [35]. Since it is an intriguing possibility, that there do not exist the light Higgs boson at all as in the strongly-interacting scenarios, the effect of the *non-existence* of the light Higgs boson should be regarded as a *signal*, while the case with the light Higgs boson should be regarded as a reference. Thus, we consider the case with the massless Higgs boson as the 'continuum' production, and discuss the effect of the Higgs boson from the difference with the $m_H = 0$ case.

The diagrams of this class of the processes fall into two classes; $s$-channel diagrams and $t$-channel diagrams. Since they are gauge-invariant separately, we can discuss them separately as well. The results in this chapter are obtained only for the $t$-channel diagrams. Most of the $s$-channel processes can be understood as the creation of the vector bosons (including off-shell photon $\gamma^*$) and their subsequent decays into the fermions, like $e^+e^- \to W^+W^-Z$ followed by $Z \to \nu_e\bar{\nu}_e$. Other kinematical regions have very small cross sections, since we are discussing the processes of $O(\alpha^4)$ here, and can be quite safely neglected. Thus our results in this chapter are expected not to get modified much, except the regions of the vector boson productions mentioned above.

### 7.1.1 $e^+e^- \to \nu_e\bar{\nu}_e W^+W^-$, $\nu_e\bar{\nu}_e ZZ$

These processes are the most discussed processes as promising places to study the Higgs boson signal and the $W^+W^-$ scattering process. Both play fundamental roles in studying the physics of the symmetry breaking. The Feynman diagrams are shown in Fig. 7.1 and 7.2. The diagrams cannot be separated into smaller gauge-invariant groups and should be evaluated all together. This problem has been making the study hard.

Among all the processes at TeV $e^+e^-$ collider, the final state $\nu_e\bar{\nu}_e W^+W^-$ is most sensitive to the Higgs boson signal. First, the Higgs boson production via $e^+e^- \to \nu_e\bar{\nu}_e H$ has the largest cross section above 1 TeV as discussed in the Chap. 5, and the Higgs boson has the largest branching ratio into $W^+W^-$ while that into $ZZ$ is its half.

### 7.1.2 $e^+e^- \to \nu_e\bar{\nu}_e t\bar{t}$

This process is expected to be effective in testing the Yukawa couping of the top quark to the Higgs boson. Though the Higgs boson decays mainly into $W^+W^-$ and $ZZ$, the



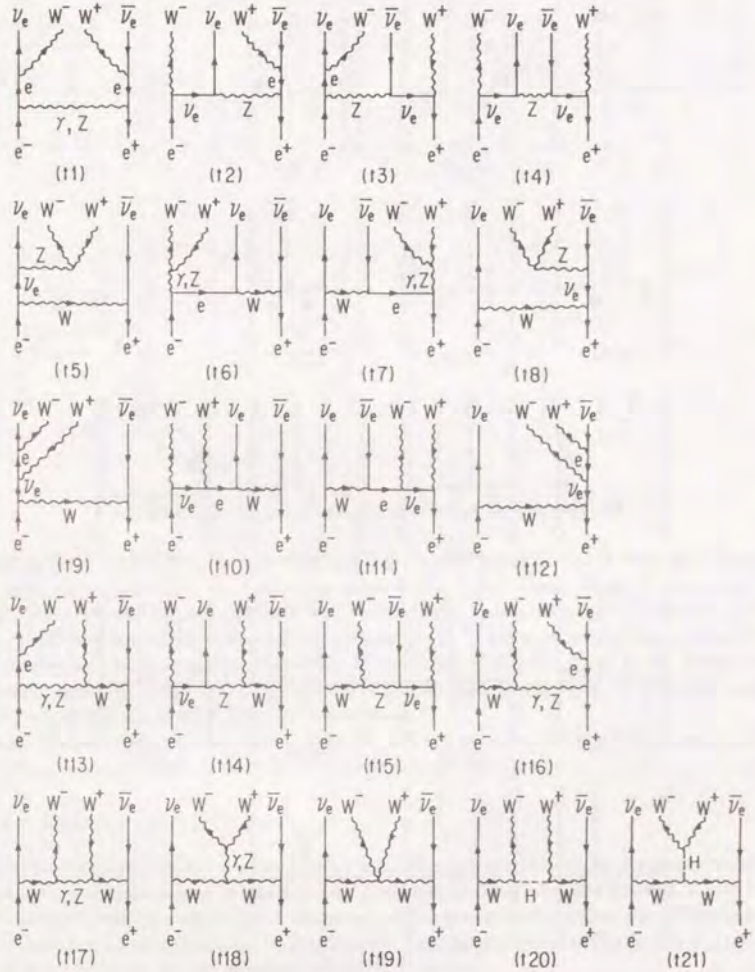


Figure 7.1: Feynman diagrams of the process $e^+e^- \to \nu_e\bar{\nu}_e W^+W^-$.

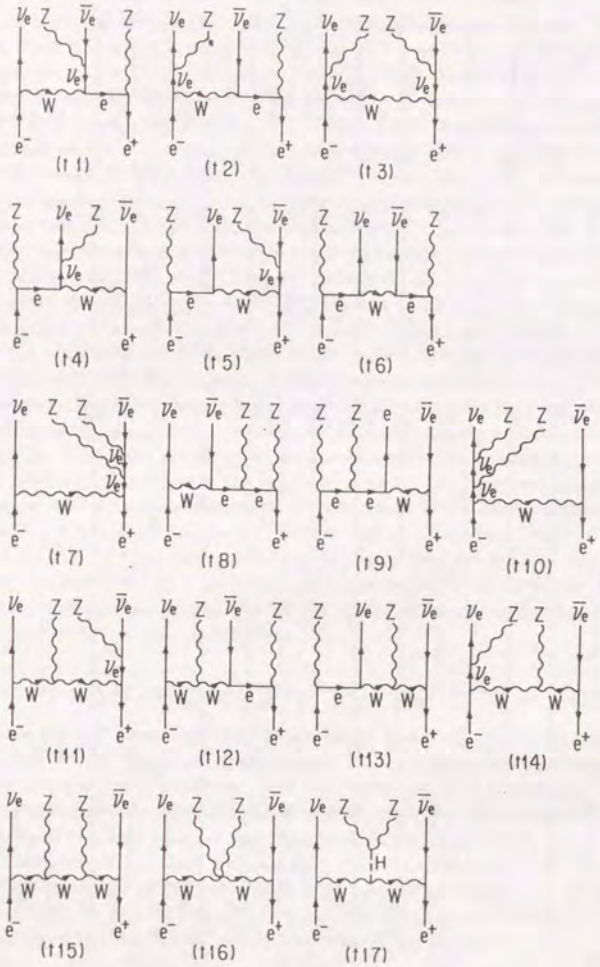


Figure 7.2: Feynman diagrams of the process $e^+e^- \to \nu_e\bar{\nu}_e ZZ$.



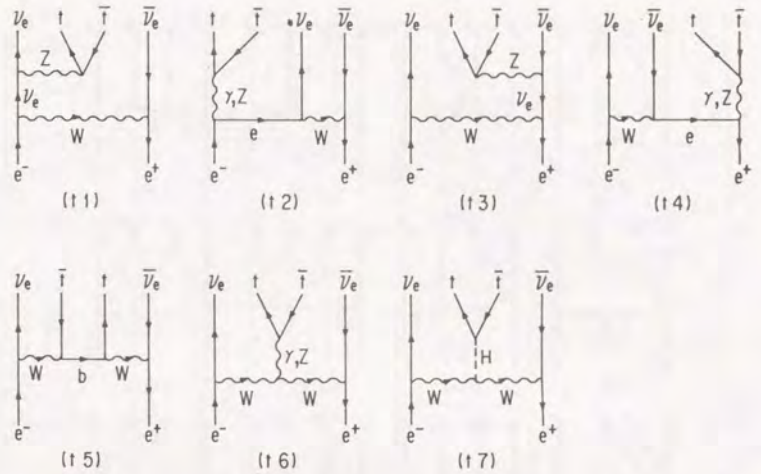


Figure 7.3: Feynman diagrams for the process $\nu_e\bar{\nu}_e t\bar{t}$.

branching ratio into $t\bar{t}$ may be not very small if the top quark is heavy. For the top quark with mass $m_t = 150$ GeV, the branching ratio of the 1 TeV heavy Higgs boson is as large as 7%. Thus we can expect a large effect of the Higgs boson exchange. Since the process $e^+e^- \to t\bar{t}Z$ was not effective enough in measuring the Yukawa coupling, this process is the most promising one in studying the origin of the fermion masses. Even if the Higgs sector is strongly coupled, the $J = 0$ partial wave of the $t\bar{t}$ system will show its strongly coupled nature, which can be studied only in this process.

The Feynman diagrams are shown in Fig. 7.3. They compose a minimum gauge invariant set of the diagrams which cannot be separated into smaller goups.

### 7.1.3 $e^+e^- \to e^+e^-W^+W^-$

The Feynman diagrams are shown in Fig. 7.4. Here again the whole diagrams consitute the minium gauge-invariant set and cannot be separated into smaller groups. Only if the electrons have positive chirality, the diagrams can be grouped to smaller sets. This provides a useful check of the computation by treating the smaller sets separately. However we should deal with all of them for the negative chirality electrons.

This process acts as the "two-photon" background to the final state $\nu_e\bar{\nu}_e W^+W^-$. Since the cross section of this process is huge, we should make an efficient cut to reduce this background. Gunion and Tofighi-Niaki [38], however, showed that this background can be efficiently removed by vetoing the forward electron/positron and a cut on the trasverse

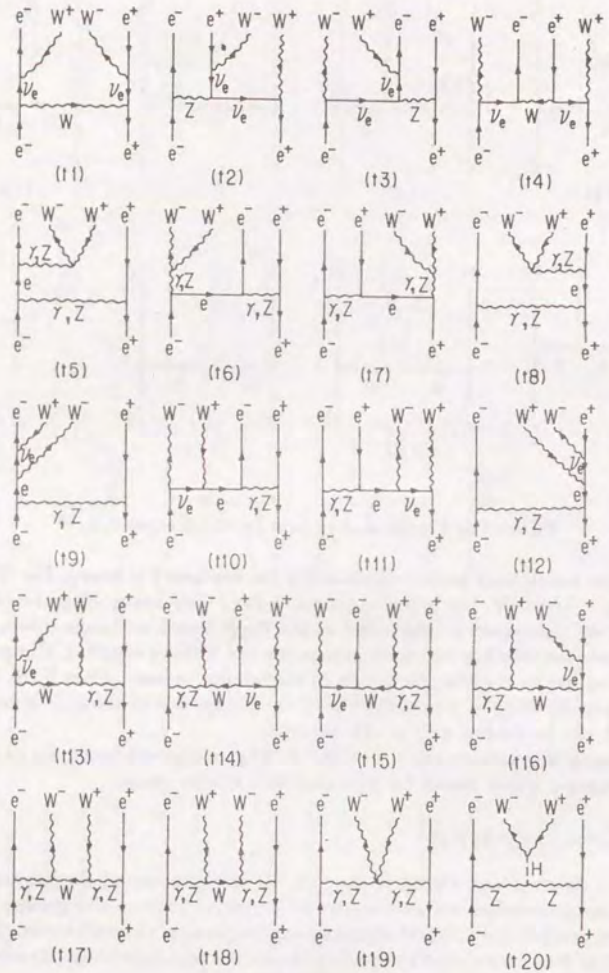


Figure 7.4: Feynman diagrams of the process $e^+e^- \to e^+e^-W^+W^-$.



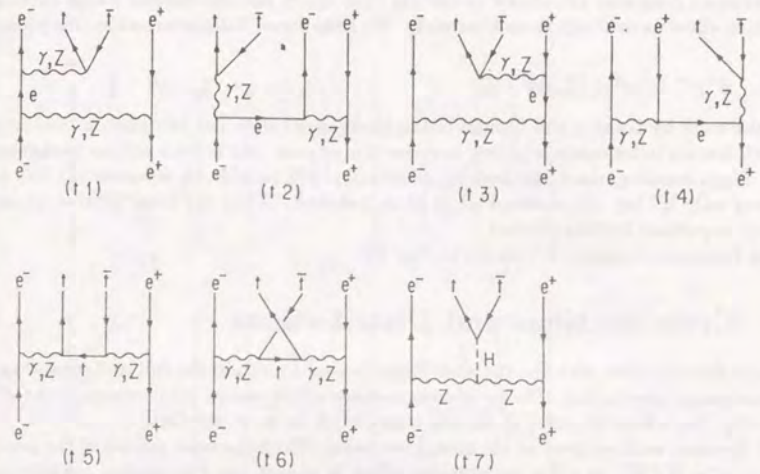


Figure 7.5: Feynman diagrams of the process $e^+e^- \to e^+e^-t\bar{t}$.

momentum of the $W^+W^-$ system.

This process has the Higgs boson contribution as well. We may be able to detect the effect by requiring double tagging on the forward electrons to select out the events with large momentum transfers of $|t| \sim O(m_Z^2)$. More study is necessary.

### 7.1.4 $e^+e^- \to e^+e^-t\bar{t}$

The Feynman diagrams are shown in Fig. 7.5. This process is the two-photon background to the final state $\nu_e\bar{\nu}_e t\bar{t}$, just as $e^+e^-W^+W^-$ is to $\nu_e\bar{\nu}_e W^+W^-$. The cross section of this process is not so huge compared to that of $e^+e^-W^+W^-$, and can be indeed rejected by applying the same type of cuts as that mentioned on $e^+e^-W^+W^-$.

### 7.1.5 $e^+e^- \to e^+e^-ZZ$

This process is the unique process which posseses the safe $m_H \to \infty$ limit among the processees discussed in this chapter. The $ZZ$ scattering can be indeed strongly coupled, however the amplitude does not blow up due to the duality of $s$-, $t$- and $u$-channels, where the amplitudes in these channels will sum up to a safe amplitude:

$$G_F s + G_F t + G_F u = 4G_F m_Z^2. \tag{7.8}$$

The Feynman diagrams are shown in the Fig. 7.6. They fall into several gauge invariant sets which allow us to study them separately. We have found little interests in this process.

### 7.1.6 $e^+e^- \to e^\pm\nu_e(\bar{\nu}_e)W^\mp Z$

After the work by Gunion and Tofighi-Niaki, background from the two-photon production of $W$'s is known to be safely rejected, however this process may serve a serious background to the Higgs hunting, since the hadron calorimetry will be able to separate the $W$- and $Z$-bosons only if they are comparable in their numbers. Thus the cross section at large angles is important for this process.

The Feynman diagrams are shown in Fig. 7.7.

## 7.2 Cross Sections and Distributions

We show first the case with the massless Higgs boson, to obtain the full understanding of the 'continuum' production. The total cross sections are shown vs. c.m. energy of the $e^+e^-$ in the Fig. 7.8, where the mass of the top quark is set to $m_t = 150$ GeV.

All the cross sections grow as the energy increases. The large cross section of the process $e^+e^- \to e^+e^-W^+W^-$ is quite remarkable, which is almost the two-photon contribution. Other processes have the cross sections of several tens of femto-barns, whose study requires the integrated luminosity of the order of $10 - 100$ fb$^{-1}$.

### 7.2.1 $e^+e^- \to \nu_e\bar{\nu}_eW^+W^-$, $\nu_e\bar{\nu}_eZZ$

As we did in the previous chapters, we show the angular distribution of the final state particles at first. The pseudo-rapidity distributions in the Fig. 7.9 of the process $e^+e^- \to \nu_e\bar{\nu}_eW^+W^-$ suggest that the process is completely a $W$-fusion type process, just like the $e^+e^- \to \nu_e\bar{\nu}_eZ$ as discussed in the Chap. 4. The distributions of the $\nu_e\bar{\nu}_eZZ$ final state are similar. The final neutrinos are emitted into the forward direction with recoil with a typical $p_T$ of $O(m_W)$ from $W$-emission, and the anti-neutrions into the backward direction similarly. The $W^+W^-$ system and $ZZ$ system are produced centrally. In $\nu_e\bar{\nu}_eW^+W^-$ final state, the $t$-channel $W$-bosons emitted from the beams collide to materialize into the on-shell states, where they exchange $\gamma$ or $Z$ both in $s$- and $t$-channel. To make the $t$-channel propagator factor as large as possible, the collision favours small angles, and the $W^-$ boson emitted from the initial $e^-$ beam will not be scattered much to appear mainly in the forward direction. The same applies to the $W^+$. Though the photon is exchanged in the $t$-channel, there does not appear the Coulomb pole which gives infinite cross section if present, since the $t$-channel $W$-bosons from the electrons are off-shell and the photon has to transfer energies to materialize the $W$'s.

In $\nu_e\bar{\nu}_eZZ$ final state, $W$-bosons emitted from fermion lines exchange $W$-boson in the $t$- and $u$-channel to materialize. This vector boson exchange in the $t$-channel again favours small angles to the beam direction where both forward and backward are equally 'small



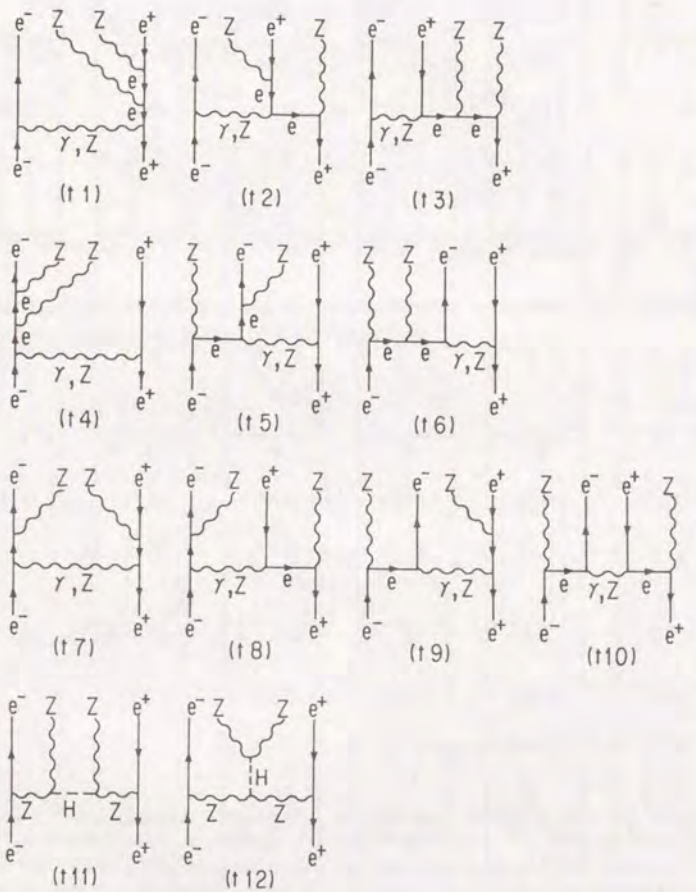


Figure 7.6: Feynman diagrams of the process $e^+e^- \to e^+e^-ZZ$.

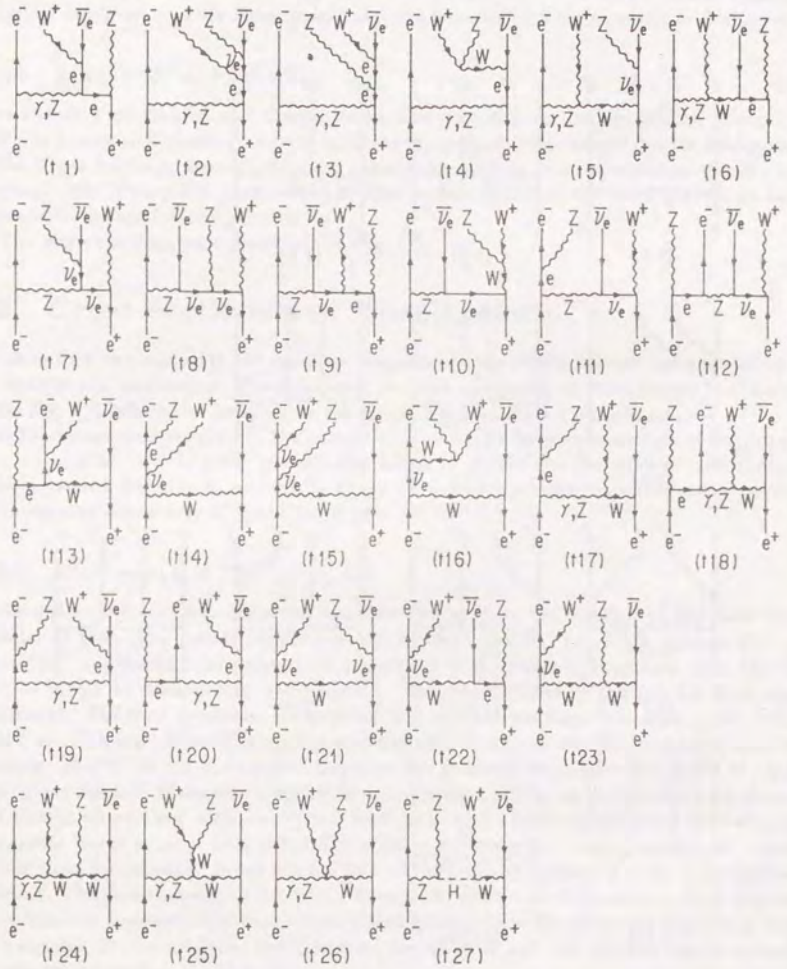


Figure 7.7: Feynman diagrams of the process $e^+e^- \to e^-\bar{\nu}_e W^+ Z$.



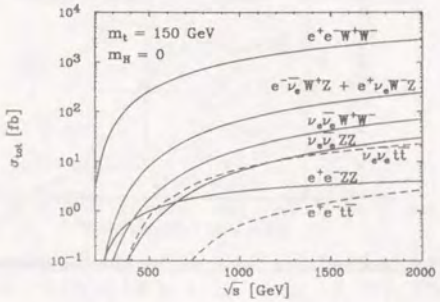


Figure 7.8: Total cross sections of the vector boson fusion processes, whith $m_H = 0$. The mass of the top quark is set $m_t = 150$ GeV throughout.

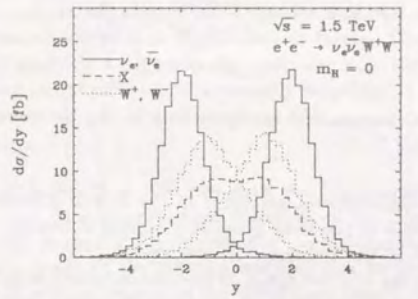


Figure 7.9: Pseudo-rapidity distribution of the final state particles in the process $e^+e^- \to \nu_e\bar{\nu}_e W^+W^-$, at c.m. energy of 1.5 TeV and $m_H = 0$. The symbol $X$ stands for the $W^+W^-$ system. Solid curve shows the distribution of neutrions, where the curve with peak at positive $y$ is that of $\nu_e$, and that at negative $y$ is of $\bar{\nu}_e$. The dashed curve is the distribution of $X$. The distribution of final $W$-bosons are shown by dotted lines, of which the one with a peak at positive $y$ belongs to $W^-$.

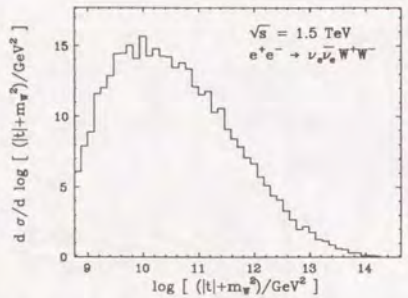


Figure 7.10: The distribution in the logarithm of the $t$-channel $W$-propagator.


Figure 7.11: Typical kinematical configurations in the processes (a) $e^+e^- \to \nu_e\bar{\nu}_e W^+W^-$ and (b) $e^+e^- \to \nu_e\bar{\nu}_e ZZ$.

angles' due to the simultaneous existence of the $t$- and $u$-channel exchanges. This is of course the consequence of the Bose symmetry of final $Z$-bosons.

The distribution of the $t$-channel $W$-propagator (Fig. 7.10) shows that the process is indeed analogous to the $e^+e^- \to \nu_e\bar{\nu}_e Z$, where the distribution in $\log(|t|+m_W^2)$ rises linearly first, where the $e^+e^- \to \nu_e\bar{\nu}_e H$ does not have the rising part. Thus in the continuum production with massless Higgs boson, the $t$-channel $W$-boson exchange is dominated by the transverse components.

The typical kinematical configurations are shown in Fig. 7.11.

Now we come to our main concern, the effect of the Higgs boson. We show the dependence of the total cross section to the mass of the Higgs boson in Fig. 7.12. As is evident from the figure, the effect of the Higgs boson is enormous, compared to the case of $e^+e^- \to W^+W^-Z$ or $ZZZ$. One very interesting point is that the $m_H = 0$ case and $m_H = \infty$ case is clearly different in the total cross section with 4 fb in $\nu_e\bar{\nu}_e W^+W^-$ and 2 fb



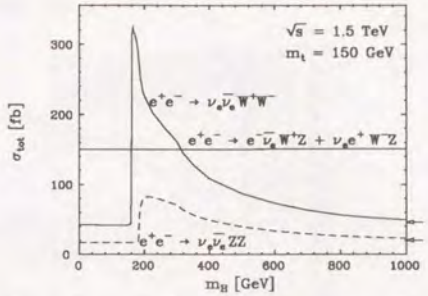


Figure 7.12: Higgs mass dependences of the total cross sections for three final states, $\nu_e\bar{\nu}_e W^+W^-$, $\nu_e\bar{\nu}_e ZZ$ and $e^\pm\nu_e(\bar{\nu}_e)W^\mp Z$ at c.m. energy 1.5 TeV. The values shown by the arrows are those of the case $m_H = \infty$.

in $\nu_e\bar{\nu}_e ZZ$ final state, which is the effect of the 'unitarity cancellation' [35].

Signals of the Higgs boson will be enhanced by applying cuts to require the $W$- or $Z$ bosons are produced at large angles. We show a scatter plot in the plane ($m_{WW}$, $\cos\theta_W$) in Fig. 7.13, for the case $m_H = 400$ GeV and $\sqrt{s} = 1.5$ TeV. The angle $\theta_W$ is defined in the laboratory frame. One observes the flat distribution from the Higgs boson signal and forward peak from the continuum scattering. Even in case of the strongly coupled Higgs sector, the non-perturbative nature will show itself in the $J = 0$ partial wave at first, which will also contribute to the flat distribution in the laboratory frame. Thus the study on the $J = 0$ partial wave made by applying a cut on $\cos\theta_W$, selecting only the large angle events will be important in studying the physics of the symmetry breaking.

### 7.2.2 $e^+e^- \to \nu_e\bar{\nu}_e t\bar{t}$

The process is again of the $W$-fusion type. We only show the Higgs mass dependence of the total cross section in Fig. 7.14. One observes that the effect of the Higgs boson exchange is large, much larger compared to that of the process $e^+e^- \to t\bar{t}Z$ discussed in the previous chapter. We expect that the study of the Yukawa coupling can be done in this process. Here again the cases $m_H = 0$ and $\infty$ (shown by the arrow) are clearly different, where the 'unitarity cancellation' is present.

The typical kinematical configuration is shown in Fig. 7.15.

### 7.2.3 $e^+e^- \to e^\pm\nu_e(\bar{\nu}_e)W^\mp Z$

We show the pseudo-rapidity distribution of the final state particles in Fig. 7.16. The wide plateau of the distribution comes from the $t$-channel photon exchange which we encountered in the process $e^+e^- \to e^-\bar{\nu}_e W^+$. In fact this process is completely analogous, if we replace

Figure 7.13: Scatter plot in the plane $(x,\ y) = (m_{WW},\ \cos\theta_W)$ at c.m. energy 1.5 TeV for the process $e^+e^- \to \nu_e\bar{\nu}_e W^+W^-$. The mass of the Higgs boson is set to $m_H = 400$ GeV. The unit for $x$-axis is TeV.

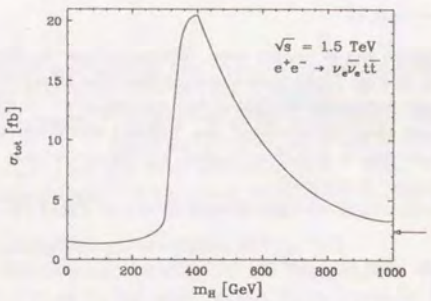


Figure 7.14: Higgs mass dependence of the total cross section at the c.m. energy of 1.5 TeV. Here the mass of the top quark is set $m_t = 150$ GeV.



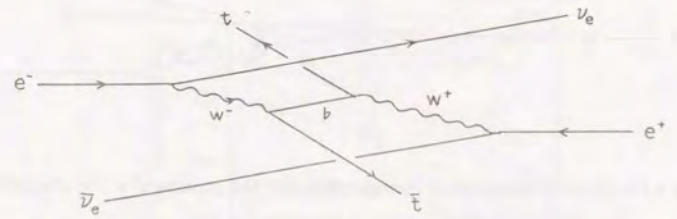


Figure 7.15: Typical kinematical configuration of the process $e^+e^- \to \nu_e\bar{\nu}_e t\bar{t}$.

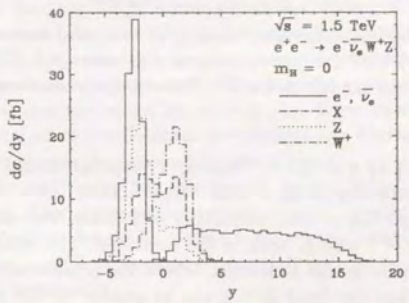


Figure 7.16: Pseudo-rapidity distribution of the process $e^+e^- \to e^\pm\nu(\bar{\nu})W^\mp Z$ at c.m. energy of 1.5 TeV with $m_H = 0$. The solid lines are for $e^-$ and $\bar{\nu}_e$, where the first one lies for positive $y$ and the latter for negative. The dashed line corresponds to $X$ which stands for the $W^+Z$ system. The curve for $W^+$ is shown by dash-dotted line which tends to favor positive $y$, and $Z$ (dotted curve) tends to favour negative $y$.

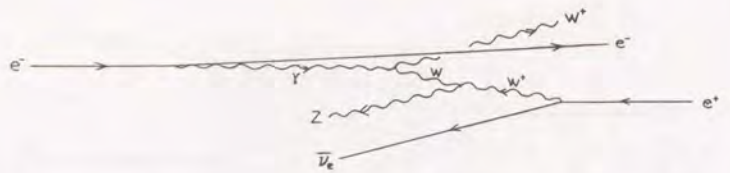


Figure 7.17: Typical kinematical configuration for the process $e^+e^- \to e^\pm\nu(\bar{\nu})W^\mp Z$.

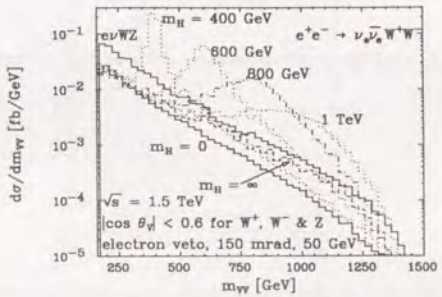


Figure 7.18: The invariant mass distributions of two weak bosons, in $e^+e^- \to \nu_e\bar{\nu}_e W^+W^-$ and $e^+e^- \to e^\pm\nu_e(\bar{\nu}_e)W^\mp Z$ for various $m_H$ at c.m. energy 1.5 TeV. Only the events with large angle weak bosons are selected while forward electrons are *veto*ed if $E_e > 50$ GeV *and* $\theta_e > 150$ mrad.

the $W^+Z$ system ($X$) by a single $W^+$ boson. This point should be clear by comparing the pseudo-rapidity distribution of the $e^-\bar{\nu}_e W^+$ final state.

We can understand this process pictorially as follows. The electron emits a photon, and the positron emits a $W^+$ boson, both in the $t$-channel. The photon and $W^+$ boson scatter by exchanging $W$-boson in the $t$-channel, where the photon will be transformed into $W^+$ and $W^+$ into $Z$. Thus the final $W^+$ tends to appear in the forward direction (positive pseudo-rapidity) and $Z$ in the backward direction (negative pseudo-rapidity).

The total cross section is almost independent on the mass of the Higgs boson (Fig. 7.12), since no resonance contribution appears in Feynman diagrams of Fig. 7.7, and it couples only to the $t$-channel $Z$-boson whose effective luminosity is very small due to the small $Zee$ coupling. Furthremore, if we *veto* the forward electron/positron, the $Z$-boson exchange can be neglected due to the small 'mass' of the $t$-channel vector boson, which makes the effect of the Higgs exchange completely negligible.

The important point here is that the total cross section of this process is not huge, only three-times as large as the cross section into $\nu_e\bar{\nu}_e W^+W^-$ with massless Higgs exchange whose



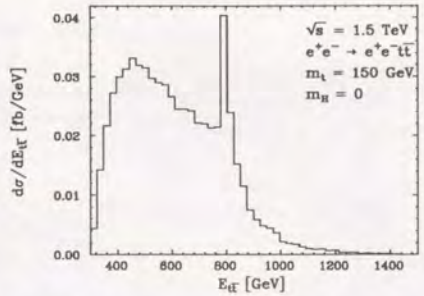


Figure 7.19: Distribution in $E_{t\bar{t}}$ in the process $e^+e^- \to e^+e^-t\bar{t}$.

case has the minimum cross section (Fig. 7.12). When we wish to separate $\nu_e\bar{\nu}_e W^+W^-$ final state, we cannot reject this process by a cut on the transverse momentum, since $p_T$ of $W^\pm Z$ system is of $O(m_W)$ due to the $t$-channel $W$-exchange. Pseudo-rapidities of the final vector bosons are comparable with those of $\nu_e\bar{\nu}_e W^+W^-$ as well. Thus the kinematical cuts will not be effective to drop this background. The only method we can think of so far is to separate $W$- and $Z$-bosons by calorimentric method. This requires that the numbers of $W$- and $Z$-bosons are comparable, unless the tail of their natural width will make the distinction completely obscure. Recall that the Higgs boson signal and strong $WW$-scattering signal always comes in $J = 0$ wave, which gives almost isotropic distribution in the laboratory frame as seen in the Fig. 7.13. After selecting large angle events only, the $\nu_e\bar{\nu}_e W^+W^-$ signal and $e^\pm\nu_e(\bar{\nu}_e)W^\mp Z$ background can be comparable. We show one example in Fig. 7.18, where $m_{WW}$ and $m_{WZ}$ distributions are presented for various $m_H$. Here, even the $m_H \to \infty$ case has S/N $\sim O(1)$! Studies including the detector simulations are necessary to see how well this distinction can be done in actual experimental situations.

If the Higgs sector is strongly coupled, the $J = 1$ partial wave of this process may become strongly interacting. The $\rho$-like vector resonance may appear in this process. To study the effects, forward electron should be tagged to select the events where the $Z$-boson is exchanged in the $t$-channel as well as photon. However, it may be to small to be observed due to the small effective $Z$-luminosity.

### 7.2.4 $e^+e^- \to e^+e^-W^+W^-$, $e^+e^-t\bar{t}$

Both processes are dominated by the two-photon singularities. However, as can be noticed from the Feynman diagrams of the process $e^+e^- \to e^+e^-t\bar{t}$, only the diagrams of Fig. 7.5(t5) and (t6) give the two-photon singularity while the other diagrams have the singularity with the same type as in the process $e^+e^- \to e^+e^-Z$. The coexistence of two types of singularities is most clearly exhibited in the energy distribution of the $t\bar{t}$ system ($E_{t\bar{t}}$) (Fig. 7.19), where the two-photon singularity gives a smooth, slowly dropping curve, while the $e^+e^-Z$ type

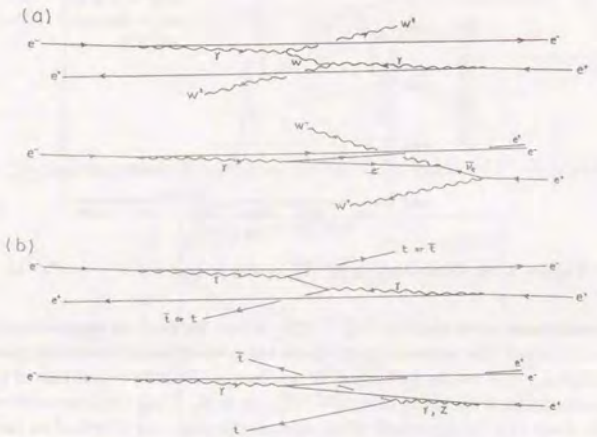


Figure 7.20: Typical kinematical configurations for the processes (a) $e^+e^- \to e^+e^-W^+W^-$ and (b) $e^+e^- \to e^+e^-t\bar{t}$. The first ones are the two-photon type processes, and others are the singularities similar to those of the process $e^+e^- \to e^+e^-Z$. The latter singularities appear also in the $CP$-conjugate kinematics.

singularity gives a sharp peak around $E_{t\bar{t}} \sim E_{\rm beam}$. This peak can be understood in the same way as $e^+e^-Z$, that the positron beam collides on the "sea" electron inside the electron beam to produce $t\bar{t}$ pair. The situation is just the same in the process $e^+e^- \to e^+e^-W^+W^-$, though the contribution from the $e^+e^-Z$ type singularity is much less than the two-photon contributions there.

Thus there are three typical kinematical configurations for both processes as shown in Fig. 7.20.

### 7.2.5 $e^+e^- \to e^+e^-ZZ$

The distributions of this process is well summarized in the scatter plot on the $(\log|t_1|, \log|t_2|)$ plane (Fig. 7.21), where $t_1$ and $t_2$ are the squared momentum transfers of the $e^-$ and $e^+$ respectively. One observes very similar structure to that of the process $e^+e^- \to e^+e^-Z$, where the horizontally spread band corresponds to the singularity where the positron collides on the "sea" electron to produce $ZZ$ pair, and the vertically spread band to the converse situation. One new feature which was absent in the $e^+e^-Z$ case is there is a small area where both $|t_1|$ and $|t_2|$ are of the order $m_Z^2$. This part comes from the $ZZ$ scattering process




Figure 7.21: Scatter plot on the $(\log|t_1|, \log|t_2|)$ plane for the process $e^+e^- \to e^+e^-ZZ$ at c.m. energy of 1.5 TeV. Higgs mass is set to $m_H = 0$.

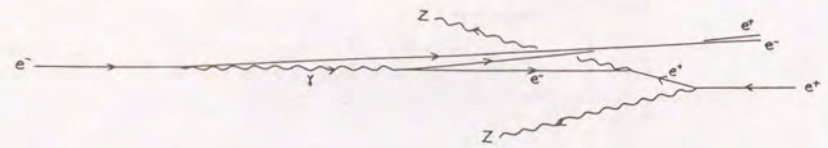


Figure 7.22: Typical configurations for the process $e^+e^- \to e^+e^-ZZ$.

where the Higgs boson is exchanged in all $s$-, $t$- and $u$-channels.

The typical configuraitions are shown in Fig. 7.22.



# Chapter 8

# Conclusions

We have calculated matrix elements of all the standard model processes that have significant cross sections at a TeV $e^+e^-$ collider up to and in the $\alpha^4$ order exactly in the tree level, by making use of a newly developed systematic method (HELAS) of evaluating helicity amplitudes numerically (Chap. 2). Typical distributions of all the final states have been discussed, with the emphasis to ***understand*** the dominant kinematical configurations of each process. Indeed, we have established an intuitive picture of all the final state configurations that were studied in this report, which should be useful when we go on to study event generations and to simulate real experiments.

In Chap. 3, we first discussed the order $\alpha^2$ vector boson pair production processes, $e^+e^- \to W^+W^-$, $ZZ$, $Z\gamma$ and $\gamma\gamma$, emphasizing the role of the collinear singularity due to the $t$-channel electron/neutrino exchange. Here we found a semi-quantitative method to measure the 'strength' of the singularity, by evaluating the minimum possible value of the denominator of the $t$-channel propagators. An interesting selection rule on the helicity of the vector bosons is found, and an explanation of the rule is given in App. C. Large Forward-Backward asymmetry is expected for the proccess $e^+e^- \to t\bar{t}$.

At the order $\alpha^3$ level, we first studied the single weak boson production processes (Chap. 4), $e^+e^- \to e^\pm\nu_e(\bar{\nu}_e)W^\pm, e^+e^-Z$ and $\nu_e\bar{\nu}_eZ$. The study on these processes were mainly motivated by our desire to understand the serious backgrounds from these large cross section processes in the Higgs hunting and for possible new physics dicoveries. However, the technique we developed to evaluate these cross sections exactly proved to be essential in dealing with the vector boson fusion processes of Chap. 7, because all the proto-types of the singularities we encounter later appeared already in Chap. 4, except for the well-known two-photon type singularities. Pseudo-rapidity distributions of the weak bosons were found to be effective in demonstrating the structure of these singularities. Long high-$p_T$ tails of $W$'s and $Z$'s assosiated with high-$p_T$ neutrinos will make serious backgrounds in the Higgs hunting if its mass is around the weak boson masses.

Real production of the Higgs boson was studied in Chap. 5. Only at relatively low energies and at high values of the $m_H/\sqrt{s}$ ratio the order $\alpha^2$ process $e^+e^- \to ZH$ leads to a larger cross section than that of the order $\alpha^3$ process $e^+e^- \to \nu_e\bar{\nu}_eH$.

The order $\alpha^3$ annihilation processes into triple weak bosons, $e^+e^- \to W^+W^-Z$ and

$ZZZ$, are found to be dominated by the initial state vector boson emissions (Chap. 6). The effectiveness of a longitudinally polarized electron beam was stressed, as a unique way to make the Higgs boson signal clear in these processes, which improves S/N ratio by a factor of 100. Even the difference of $m_H = 0$ and $\infty$ can be made significant if the electron beam is 100% right-handed. There is no similar way to single out the effect of the Yukawa couping in the $t\bar{t}Z$ final state, where the measurement of the top quark helicities seems to be essential to establish the signal. Another curiosity on the final state $W^+W^-Z$ is that all the ten Feynman diagrams of Fig. 6.1 without the Higgs boson exchange contribute to cancel each other to ensure the safe high-energy behavior, which makes this process sensitive to the gauge boson self-interactions.

In Chap. 7 we studied all the order $\alpha^4$ virtual vector boson fusion processes with a pair of outgoing leptons: $e^+e^- \to \nu_e\bar{\nu}_e(e^+e^-)W^+W^-$, $\nu_e\bar{\nu}_e(e^+e^-)ZZ$, $\nu_e\bar{\nu}_e(e^+e^-)t\bar{t}$, and $e^\pm\nu_e(\bar{\nu}_e)W^\mp Z$. A systematic way to obtain distributions of these vector boson fusion processes was established. The finding, that the cross section of the process $e^+e^- \to e^\pm\nu_e(\bar{\nu}_e)W^\mp Z$ is not too large to jeopatize the Higgs boson signal in the $\nu_e\bar{\nu}_eW^+W^-$ or $\nu_e\bar{\nu}_eZZ$ channels, is a good news for the Higgs hunters. Although the effect of $ZZ$ scatterings via a Higgs boson exchange can be observed on the scatter plot of the $e^+e^-ZZ$ final state, the production cross section is found to be too small to be of practical interests. We can distinguish between the two extreme limiting cases, $m_H \to \infty$ and $m_H = 0$, in the cross sections of all the $W$-fusion processes, where the 'unitarity' cancellation between the diagrams with and without a Higgs boson exchange is taking place at TeV energies. In particular, the effect of the Yukawa coupling is found to be surprizingly large in the $\nu_e\bar{\nu}_et\bar{t}$, even if the Higgs boson is very heavy.



# Acknowledgements

This work is initiated from the collaboration with K. Hagiwara and I. Watanabe, where we formulated our idea into the HELAS system. He expresses sincere thanks to them for their collaboration which is continuing further.

All the works presented here have been done in collaboration with the members of the JLC physics working group. S. Kawabata supplied us of a beautiful Monte Carlo integration package BASES25, modified for use on VAX computers for the author, without which this work could not been done. The author is in debt to A. Miyamoto for his help on the single weak boson production processes. He and K. Fujii taught the author the very basics of high-energy expeiments. K. Fujii helped him in making cross-checks of our results on $t\bar{t}Z$ production at the early stage of our work, which gave us confidence on the HELAS system. J. Kanzaki coded most of the amplitudes discussed in Chap 7 in the HELAS system, whose hard work enabled the author to study these processes with confidence. Y. Kurihara showed him the effectiveness of a cut on the $W$ angles in the laboratory frame to study the Higgs boson signal in the $W$-fusion processes. T. Tsukamoto spent much time with the author discussing on the production of $\nu_e\bar{\nu}_et\bar{t}$, which made the author to learn about the real experimental situation.

The author is especially grateful to K. Hagiwara and K. Hikasa, who have been teaching the author starting from the basics of the elementary paritcle physics, with great patience and efforts. J. Arafune, K. Hikasa, H. Kawai and Y. Sumino read the manuscript carefully, which improved the thesis drastically.

The author is grateful to all his colleagues in the laboratory of elementary particle physics, University of Tokyo, without whose help this thesis could not be completed. He is especially grateful to H. Kawai for encouragements on his style in research. He is also grateful to the members of the physics department at KEK, where the author spent most of the time this year.

Finally the author wishes to express his thanks to Natsuko, for her encouragements and patience.

# Appendix A

# HELAS

In this appendix, we briefly review the minimal contents of the helicity amplitude evaluation scheme, HELAS [17], in order to make the paper self-contained. In the HELAS system, an arbitrary tree-level Feynman diagram is evaluated numerically by CALLing a sequence of FORTRAN77 subroutines.

## A.1 Basic Idea

Let us first discuss the general characteristic of the tree-level diagrams. As notable from the terminology 'tree', they have a common structure. There may be many external lines, however, as they approach the center of the Feynman diagrams, the external lines meet to give an off-shell internal line, they meet again to make another internal lines, untill when all the lines meet at a single point.

The basic idea of HELAS is to begin with the external lines by giving the wavefunctions explicitly under fixed notation, and give rules to join the lines. One may suppose that there may be too many possiblities to give joining rules, however, it can be classified to a *finite* set in the renormalizable theories. We show all the possible rules in the renormalizable theories in the Tab. A.1.

Thus the whole package consists at least from two parts: wavefuctions and vertices. Then the amplitudes can be computed as follows. First, the external wave functions are evaluated as functions of the particle momenta and helicities. Second, off-shell scalar/spinor/vector ($S/F/V$) lines obtained from the external lines via renormalizable vertices are evaluated as functions of the external wave functions. This second step can be repeated to evaluate internal off-shell lines as functions of external off-shell lines, untill all the off-shell lines meet. We first present our notations for external fermion and vector boson wave functions, and then give the vertices which we need in this paper. We explain them separately in the following sections.



| input | output | interaction |
|---|---|---|
| $FF$ | $V$ | vector or axial vector couplings |
| | $S$ | Yukawa couplings |
| $FV$ | $F$ | vector or axial vector couplings |
| $FS$ | $F$ | Yukawa couplings |
| $VV$ | $V$ | Yang-Mills couplings |
| | $S$ | Higgs interaction |
| $VS$ | $V$ | Higgs interaction |
| $SS$ | $V$ | scalar gauge couplings (current) |
| | $S$ | scalar self-couplings |
| $VVV$ | $V$ | Yang-Mills couplings |
| $VVS$ | $S$ | scalar gauge couplings (seagull) |
| $VSS$ | $V$ | scalar gauge couplings (seagull) |
| $SSS$ | $S$ | scalar self-couplings |

Table A.1: List of the possible vertices in the renormalizable theories. All these vertices are incorporated in the HELAS system.

## A.2 Wavefunctions

An external fermion wave function is calculated in the Weyl basis of Ref. [15]:

$$\begin{aligned} |f\rangle_\alpha &\equiv |f(p_f,\sigma_f,S_f)\rangle_\alpha \\ &= \bar{S}_f\,\omega_{\alpha\sigma_f}(p_f)\,\chi_{\sigma_f}(p_f) \end{aligned} \tag{A.1}$$

for a fermion with its fermion number flowing-in to a diagram, and

$$\langle f|_\alpha = (|f\rangle_\alpha)^\dagger \tag{A.2}$$

for a fermion with a flowing-out fermion number. These states are depicted in Fig. 2.2a. The fermion four-momentum and helicity (in units of 1/2) are denoted by $p_f$ and $\sigma_f$, respectively, and the sign factor $S_f$ takes $+1$ if the fermion $f$ is a particle and $-1$ otherwise. We find it convenient to define momentum and helicity along the fermion number flow

$$\bar{p}_f = S_f p_f, \quad \bar{\sigma}_f = S_f \sigma_f. \tag{A.3}$$

The suffix $\alpha$ denotes the chirality of the spinor, $|f\rangle_\alpha$ being the non-vanishing two components of the eigen-four-spinor of the chirality projection operator

$$P_\alpha = \frac{1+\alpha\gamma_5}{2} \quad (\alpha = \pm 1), \tag{A.4}$$

in the Weyi (chiral) basis [15]. In this basis, the Dirac four-spinor is expressed as

$$\psi_f = \begin{pmatrix} |f\rangle_- \\ |f\rangle_+ \end{pmatrix} \tag{A.5}$$

where $\psi_f$ is either a $u$-spinor ($S_f = +1$) or a $v$-spinor ($S_f = -1$). The phase convention [15]

$$\bar{S}_f = \begin{cases} 1 & \text{for } S_f = +1 \\ \alpha\sigma_f & \text{for } S_f = -1 \end{cases} \tag{A.6}$$

fixes the relative phase between the spinors of a particle and its antiparticle (which is an unobservable phase if the particle number is conserved but is essential when dealing with Majorana particles [39]). The normalization factor

$$\omega_\pm(p) = (E \pm |p|)^{1/2} \tag{A.7}$$

fixes the large and small chirality component, and the helicity eigenspinor reads [15]

$$\begin{aligned} \chi_+(p) &= \frac{1}{\sqrt{2|p|(|p|+p_z)}} \begin{pmatrix} |p|+p_z \\ p_x + ip_y \end{pmatrix}, \\ \chi_-(p) &= \frac{1}{\sqrt{2|p|(|p|+p_z)}} \begin{pmatrix} -p_x + ip_y \\ |p|+p_z \end{pmatrix}, \end{aligned} \tag{A.8}$$

in an arbitrary reference frame. When a particle is moving along the negative $z$ axis ($-n_z$), the above expressions are ambiguous and we choose

$$\chi_+(-n_z) = \begin{pmatrix} 0 \\ -1 \end{pmatrix}, \quad \chi_-(-n_z) = \begin{pmatrix} 1 \\ 0 \end{pmatrix}, \tag{A.9}$$

by convention. A fermion spinor is thus specified uniquely by four indices, its four momentum ($p$), helicity ($\sigma_f$), chirality ($\alpha$), and the sign factor ($S_f$) which distinguishes between a particle and an antiparticle. In the massless limit, the spinor (A.1) simplifies to [16]

$$|f\rangle_\alpha \equiv |f(p_f, \sigma_f, S_f)\rangle_\alpha \xrightarrow{m_f \to 0} S_f \delta_{\alpha\sigma_f} \sqrt{2E_f} \chi_{\sigma_f}(p_f), \tag{A.10}$$

which exhibits the helicity selection rule (chirality conservation) for massless fermions.

In the actual program, the four complex components of each spinors and the four real components of its four-momentum $\bar{p}$ carried along the fermion number flow are combined to a single six-dimensional complex array.

An external vector boson wave function is expressed in the Cartesian basis [15,40] as

$$\begin{aligned} \epsilon^\mu(p, \lambda = 1) &= (|p|p_T)^{-1}(0, p_x p_z, p_y p_z, -p_T^2), \\ \epsilon^\mu(p, \lambda = 2) &= (p_T)^{-1}(0, -p_y, p_x, 0), \\ \epsilon^\mu(p, \lambda = 3) &= (E/m|p|)(|p|^2/E, p_x, p_y, p_z) \end{aligned} \tag{A.11}$$

for $p_V^\mu = (E, \boldsymbol{p}) = (E, p_x, p_y, p_z)$ and $p_T = (p_x^2 + p_y^2)^{1/2}$. Helicity eigen vectors are obtained from the above as

$$\begin{aligned} \epsilon^\mu(p, \lambda = \pm) &= \mp\frac{1}{\sqrt{2}}[\epsilon^\mu(p, \lambda = 1) \pm i\epsilon^\mu(p, \lambda = 2)], \\ \epsilon^\mu(p, \lambda = 0) &= \epsilon^\mu(p, \lambda = 3). \end{aligned} \tag{A.12}$$



In the limit of vanishing transverse momentum ($p_T = 0$), we define

$$\epsilon^\mu(p, \lambda = \pm) = \mp\frac{1}{\sqrt{2}}(0, 1, \pm\mathrm{sgn}(p_z)i, 0). \tag{A.13}$$

For a vector boson with momentum $p_V$, we introduce the *flowing-out* four momentum $\bar{p}_V$ as defined by

$$\bar{p}_V = S_V p_V, \tag{A.14}$$

where the sign factor $S_V$ takes $+1$ if the vector boson is outgoing and $-1$ if it is incoming. It is convernient to introduce an associated *flowing-out* polarization vector $\bar{\epsilon}_V^\mu$:

$$\begin{aligned} \bar{\epsilon}_V^\mu(p_V, \lambda_V, S_V = +) &= \epsilon_V^\mu(p_V, \lambda_V)^* \quad \text{(outgoing)}, \\ \bar{\epsilon}_V^\mu(p_V, \lambda_V, S_V = -) &= \epsilon_V^\mu(p_V, \lambda_V) \quad \text{(incoming)}. \end{aligned} \tag{A.15}$$

The polarization vectors with the above fixed notations are evaluated as the functions of the four-momentum and helicity, which forms a four-dimensional complex array. Then it is combined with the *flowing-out* four-momentum $\bar{p}_V$ to give a six-dimensional complex array. Then this six-dimensional array contains all the necessay information to be put into the vertices.

There is no notion of the *wavefunction* for the scalar particles, since it has only one component and no helicity. However, we can assign a complex *number* (or one-dimensional array) "1" as the *external wavefunction*, and can combine it with its *flowing-out* four-momentum to form a three-dimensional complex array. This treatment will be useful to deal with the off-shell scalar lines, which should carry the scalar emission amplitude and/or its propagator as a off-shell *wavefunction*, while it is just one complex number.

## A.3 Vertices

External fermion ($F$) and vector boson ($V$) wave function are now fixed, and we can calculate internal off-shell lines via the vertices $FV \to F$ (Fig. 2.2b,c) and $F\bar{F} \to V$ (Fig. 2.2d,e). We further need vertices where two vector boson fuse to give an off-shell vector $VV \to V$. However here it is often more useful to have the scalar product of the three weak bosons [17] (Fig. 2.3). The vertices of four vector bosons are treated in a special way, which will be described later briefly. The vertices containing the scalar particles are quite trivial.

The transitions $FV \to F$ and $F\bar{F} \to V$ occurs via the interaction Lagrangian

$$\mathcal{L} = -\sum_\alpha g_\alpha^{Vf'f} V_\mu \bar{\psi}_{f'} \gamma^\mu P_\alpha \psi_f. \tag{A.16}$$

Non-vanishing couplings in the standard model are

$$\begin{aligned} & g_\pm^{\gamma ff} = eQ_f, \\ & g_+^{Zff} = g_Z Q_f \sin^2\theta_W, \quad g_-^{Zff} = g_Z[T_{3f} - Q_f \sin^2\theta_W], \\ & g_-^{W\nu l} = g_-^{Wl\nu} = \tfrac{1}{\sqrt{2}} g_W, \\ & g_-^{Wu_i d_j} = (g_-^{Wd_j u_i})^* = \tfrac{1}{\sqrt{2}} g_W V_{ij}. \end{aligned} \tag{A.17}$$

where $e = \sqrt{4\pi\alpha}$ is the magnitude of the electron charge,

$$g_W = \frac{e}{\sin\theta_W}, \quad g_Z = \frac{e}{\sin\theta_W \cos\theta_W}, \tag{A.18}$$

and $V_{ij}$ denotes the Kobayashi-Maskawa matrix element [41] between the mass eigenstates $(u_1, u_2, u_3) = (u, c, t)$ and $(d_1, d_2, d_3) = (d, s, b)$.

An off-shell fermion line associated with the transition $FV \to F$ (Fig. 2.2b) is then expressed as

$$\begin{aligned} |V, f\rangle_\alpha &\equiv |V(p_V, \lambda_V, S_V), f(p_f, \sigma_f, S_f)\rangle_\alpha \\ &= g_{-\alpha}^{Vff}(\not{f})_{-\alpha}|f\rangle_{-\alpha}, \end{aligned} \tag{A.19}$$

if the fermion number is flowing-in to the diagram, and

$$\langle f, V|_\alpha = g_{-\alpha}^{Vff'}\langle f|_{-\alpha}(\not{f})_{-\alpha}, \tag{A.20}$$

if the fermion number is flowing-out. Here the use are made of the *flowing out* wave function (A.15) of the vector boson. Off-shell fermion lines including the propagator factor (solid blob in Fig. 2.2c) are expressed as

$$\begin{aligned} |f', V, f\rangle_\alpha &= D_{f'}(p_{f'}^2)[(\not{p}_{f'})_{-\alpha}|V, f\rangle_{-\alpha} + m_{f'}\,|V, f\rangle_\alpha], \\ \langle f, V, f'|_\alpha &= D_{f'}(p_{f'}^2)[\langle f, V|_{-\alpha}(\not{p}_{f'})_{-\alpha} + m_{f'}\langle f, V|_\alpha]. \end{aligned} \tag{A.21}$$

In the HELAS Feynman rules (Fig. 2.2), the solid blob denotes the propagator factor

$$D_a(p_a^2) = 1\Big/\left[p_a^2 - m_a^2 + im_a\Gamma_a\theta(p_a^2)\right], \tag{A.22}$$

while the cross symbol denotes that the line is truncated. The slashed quantities in (A.19-21) are $2 \times 2$ complex matrices as defined by

$$(\not{a})_\pm = \sigma_\pm^\mu a_\mu = \begin{pmatrix} a^0 \mp a^3 & \mp(a^1 - ia^2) \\ \mp(a^1 + ia^2) & a^0 \pm a^3 \end{pmatrix}, \tag{A.23}$$

where

$$\sigma_\pm^\mu = (1, \pm\sigma), \tag{A.24}$$

with $\sigma$ being the Pauli matrices. Off-shell two spinors (A.19–21) are easily evaluated by a successive multiplication of $2 \times 2$ matrices of the form (A.23) on the external spinors (A.1-2). It should be noted that the off-shell bra-spinor (A.20) is *not* in general the Hermitian conjugate of the off-shell ket-spinor (A.19). The off-shell spinors including the propagator factor (A.21) reduce to those of Ref. [16] in the massless fermion limit ($m_f = m_{f'} = 0$).

An off-shell vector line of Fig. 2.2d for the $F\bar{F} \to V$ transition is calculated as

$$\begin{aligned} \hat{J}^\mu(\langle f_2|V|f_1\rangle) &\equiv \hat{J}^\mu(\langle f_2(p_2, \sigma_2, S_2)|V|f_1(p_1, \sigma_1, S_1)\rangle) \\ &= \sum_\alpha g_\alpha^{Vf_2f_1}\langle f_2|_\alpha(\sigma^\mu)_\alpha|f_1\rangle_\alpha. \end{aligned} \tag{A.25}$$



The off-shell vector line including the propagator factor is then expressed as

$$J^\mu(\langle f_2|V|f_1\rangle) = -D_V(p_V^2)\left[\hat{J}^\mu(\langle f_2|V|f_1\rangle) - \theta(m_V^2)\sum_\alpha g_\alpha^{Vf_2f_1}\frac{p_V^\mu}{m_V^2}\langle f_2|_\alpha(\not{p}_V)_\alpha|f_1\rangle_\alpha\right], \tag{A.26}$$

in the unitary gauge. The latter term in the brace is absent for conserved currents. The unitarity gauge is found to be more suited [17] for studying consequences of a wider range of theories than the renormalizable gauges. The bispinor current $\langle f_2|_\alpha(\sigma^\mu)_\alpha|f_1\rangle_\alpha$ of (A.25) has a simple analytic expression in the current rest frame for a timelike current with $p_V^2 > (m_{f1} + m_{f2})^2$. In general, it is expressed in terms of the complex components of the two spinors

$$|\,f_1\rangle_\alpha = \begin{pmatrix} a_{1\alpha} \\ b_{1\alpha} \end{pmatrix}, \quad \langle f_2|_\alpha = (a_{2\alpha}, b_{2\alpha}), \tag{A.27}$$

as

$$\begin{aligned} &\langle f_2\,|_\alpha\,(\sigma^\mu)_\alpha\,|\,f_1\rangle_\alpha \\ &= [(a_{2\alpha}a_{1\alpha} + b_{2\alpha}b_{1\alpha}),\ \alpha(a_{2\alpha}b_{1\alpha} + b_{2\alpha}a_{1\alpha}),\ -i\alpha(a_{2\alpha}b_{1\alpha} - b_{2\alpha}a_{1\alpha}),\ \alpha(a_{2\alpha}a_{1\alpha} - b_{2\alpha}b_{1\alpha})], \end{aligned} \tag{A.28}$$

for a given chirality, $\alpha$.

The vertices $FV \to F$ (A.19–21) and $F\bar{F} \to V$ (A.25–26) can be applied succesively to generate more internal off-shell lines. For example, a successive application of the rules (A.19–21) give an off-shell fermion line with a multiple vector boson emission depicted as

$$\begin{aligned} |f_2, V_2, f_1, V_1, f\rangle_\alpha &\equiv |f_2, V_2, (|f_1, V_1, f\rangle)\rangle_\alpha, \\ \langle f, V_1, f_1, V_2, f_2|_\alpha &\equiv \langle(\langle f, V_1, f_2|), V_2, f_2|_\alpha. \end{aligned} \tag{A.29}$$

Also an internal off-shell vector line is obtained from an external and an off-shell fermion line as

$$\begin{aligned} \hat{J}^\mu(\langle f_3|\,V_2\,|f_2, V_1, f_1\rangle) &\equiv \sum_\alpha g_\alpha^{V_2f_3f_2}\langle f_3|_\alpha(\sigma^\mu)_\alpha|f_2, V_1, f_1\rangle_\alpha, \\ \hat{J}^\mu(\langle f_3, V_2, f_2|\,V_1\,|f_1\rangle) &\equiv \sum_\alpha g_\alpha^{V_1f_2f_1}\langle f_3, V_2, f_2|_\alpha(\sigma^\mu)_\alpha|f_1\rangle_\alpha. \end{aligned} \tag{A.30}$$

In Eqs. (A.29) and (A.30), off-shell spinors replace the external spinors of Eqs. (A.21) and (A.25), respectiverly. Likewise, a vector boson decay ($V \to f_1\bar{f}_2$) is obtained simply by a substitution

$$\epsilon_V^\mu(p_V, \lambda_V, S_V) \longrightarrow J^\mu(\langle f_2|V|f_1\rangle). \tag{A.31}$$

In ofer to close two off-shell fermion lines, we introduce the scalar product of two spinors,

$$\langle f_2|f_1\rangle \equiv \langle f_2|_+|f_1\rangle_- + \langle f_2|_-|f_1\rangle_+. \tag{A.32}$$

Here the spinor products in the r.h.s. are calculated in terms of the components of (A.27) as

$$\langle f_2|f_1\rangle = (a_{2+}a_{1-} + b_{2+}b_{1-}) + (a_{2-}a_{1+} + b_{2-}b_{1+}). \tag{A.33}$$

Two off-shell vector boson lines can be closed simply by the dot-product of two complex four-vectors.

Finally, the gauge boson three point vertex as depicted by the Feynman rule of Fig. 2.3 is expressed as

$$\Gamma_{WW3}\Big(W^-(\bar{p}_1), W^+(\bar{p}_2), W^3(\bar{p}_3)\Big) = g_W \Gamma\Big(W^-(\bar{p}_1), W^+(\bar{p}_2), W^3(\bar{p}_3)\Big) \tag{A.34}$$

with

$$\begin{aligned}\Gamma(V_a, V_b, V_c) &= [g_{\alpha\beta}(\bar{p}_a - \bar{p}_b)_\gamma + g_{\beta\gamma}(\bar{p}_b - \bar{p}_c)_\alpha + g_{\gamma\alpha}(\bar{p}_c - \bar{p}_a)_\beta]\, V_a^\alpha V_b^\beta V_c^\gamma \\ &= V_a{\cdot}V_b\,(\bar{p}_a - \bar{p}_b){\cdot}V_c + V_b{\cdot}V_c\,(\bar{p}_b - \bar{p}_c){\cdot}V_a + V_c{\cdot}V_a\,(\bar{p}_c - \bar{p}_a){\cdot}V_b \end{aligned} \tag{A.35}$$

where the four-vector $V_a^\mu$ is either a boson polarization vector or a current, with the *flowing-out* momentum $\bar{p}_a$;

$$V_a^\mu = \bar{\epsilon}^\mu(p_a, \lambda_a, S_a) \;\text{ or }\; J^\mu(\langle f_m|V_a|f_n\rangle). \tag{A.36}$$

This rule is to join three lines to make the single amplitude at the end of all the procedure. If we wish to continue by joining two vector boson lines to give a single vector boson line $VV \to V$, we make one free index in the expression $\Gamma(V_a, V_b, V_c)$ to give $J^\mu(V_a, V_b)$. The vector boson names are also defined by the *flowing-out* quantum numbers. With the substitution rule

$$W^3 = \cos\theta_W Z + \sin\theta_W A, \tag{A.37}$$

the two triple vector boson couplings of the standard model are

$$\begin{aligned} g_{\gamma WW} &= g_W \sin\theta_W = e, \\ g_{ZWW} &= g_W \cos\theta_W = e\,\cot\theta_W. \end{aligned} \tag{A.38}$$

We find that the numerical program can be made efficient by arranging the vertex function (A.35) as

$$\Gamma(V_a, V_b, V_c) = V_a{\cdot}V_b\,(\tilde{p}_a - \tilde{p}_b){\cdot}V_c + V_b{\cdot}V_c\,(\tilde{p}_b - \tilde{p}_c){\cdot}V_a + V_c{\cdot}V_a\,(\tilde{p}_c - \tilde{p}_a){\cdot}V_b, \tag{A.39}$$

with

$$\tilde{p}_i^\mu = \bar{p}_i^\mu - \frac{\bar{p}_i^0}{V_i^0} V_i^\mu \quad (i = a, b, c) \tag{A.40}$$

where the factors with $\bar{p}_i^0/V_i^0$ are introduced to avoid large numerical cancellations among the three terms of Eq. (A.35) when dealing with longitudinally polarized vector bosons or currents at very high energies.

The four-point coupling of the vector bosons require some care. Recall first that there come always three diagrams together once if the four-point coupling appears (see Fig. 2.4). One is the contact four-point coupling among the vector bosons, and the other two are $s$-, $t$- or $u$-channel vector boson exchange diagram with the three-point couplings. Since we expect severe cancellations among these diagrams, we have put these three diagrams together into the single vertex, which is written in the higher precision.



## A.4 Collinear Singularities

For many processes including the $t$-channel photon exchange or initial state photon emission, naive application of HELAS will break down due to severe numerical cancellations. For example in the process $e^+e^- \to e^-\bar{\nu}_e W^+$, the $t$-channel photon exchange determined the character of the whole distributions as we discussed in the Chap. 4. There a wide plateaux appeared in the pseudo-rapidity distribution of the final $e^-$, which goes up to a very forward region $1 - \cos\theta \sim 10^{-17}$. To require this accuray, we need the quadruple precision, which makes the CPU time enormously large.

To avoid this problem, we supply special subroutines to deal with the collinear singularities which include the $t$-channel photon exchange and initial state soft photon radiation.

First let us explain our treatment of the $t$-channel photon exchange. From the general framework of HELAS, all we need is the off-shell (though almost on-shell) wavefunction of the $t$-channel photon. From the HELAS Feynman rules described above, we need

$$J^\mu(\langle f_2|A|f_1\rangle) = -D_V(p_V^2)\hat{J}^\mu(\langle f_2|A|f_1\rangle), \tag{A.41}$$

with high degree of the numerical accuracy. The problem is two-fold. The denominator of the propagator factor $D_V$, and the matrix element $\hat{J}^\mu$.

From the standard notation of the Dirac spinors, we can write the current as

$$\hat{J}^\mu(\langle f_2|A|f_1\rangle) = (-e)\bar{u}(p, \sigma')\gamma^\mu u(k, \sigma), \tag{A.42}$$

for the $t$-channel photon emission from the electron current. Since the problem is limited to the case that the initial state is the electron (or positron, which will be discussed later) beam, we completely fix the frame in the followings. We take the four-momenta to be

$$\begin{aligned} k^\mu &= E(1,\ 0,\ 0,\ \beta) \\ p^\mu &= xE(1,\ \beta'\sin\theta\cos\phi,\ \beta'\sin\theta\sin\phi,\ \beta'\cos\theta), \end{aligned} \tag{A.43}$$

where

$$\begin{aligned} \beta &= \sqrt{1 - \frac{m_e^2}{E^2}}, \\ \beta' &= \sqrt{1 - \frac{m_e^2}{x^2E^2}}. \end{aligned} \tag{A.44}$$

Now we write down the expression explicitly.

For the helicity non-flip case $\sigma = \sigma'$, the truncated current reads

$$\hat{J}^\mu = (-e)\sqrt{x}(2E)\left(\cos\frac{\theta}{2},\ \sin\frac{\theta}{2}e^{-i\sigma\phi},\ i\sigma\sin\frac{\theta}{2}e^{-i\sigma\phi},\ \cos\frac{\theta}{2}\right), \tag{A.45}$$

where the terms of the order $O(m_e^2/E^2)$ are neglected. One can check the conservation of the current by contracting with the four-momentum of the photon

$$p_V^\mu = k^\mu - p^\mu$$

$$
\begin{aligned}
&= E(1-x,\ -x\beta'\sin\theta\cos\phi,\ -x\beta'\sin\theta\sin\phi,\ \beta - x\beta'\cos\theta) \\
&= E(1-x,\ -x\sin\theta\cos\phi,\ -x\sin\theta\sin\phi,\ 1-x\cos\theta) + O\left(\frac{m_e^2}{E}\right),
\end{aligned}
\tag{A.46}
$$

to the accuracy of the order $O(m_e^2/E^2)$.

Since the problem lies in the collinear limit $\cos\theta \to 1$, it is instructive to give the expression in the limit,

$$
\begin{aligned}
\hat{j}^\mu &= \sqrt{x}(2E)(1,\ 0,\ 0,\ 1), \\
p_V^\mu &= E(1-x,\ 0,\ 0,\ 1-x).
\end{aligned}
\tag{A.47}
$$

Here the truncated current is completely proportional to its four-momentum, or in other words, it is *pure gauge*! In analytic evaluatation of the amplitudes, the appearance of the pure gauge current does not cause any harm, however it requires the cancellation among the diagrams. For the numerical evaluation of the amplitudes, we wish to avoid the possible cancellations as much as we can. Since we can change the gauge of the photon freely as discussed in the Chap. 2, we subract a four-vector proportional to the four-momentum $p_V$ to make its largest component (zeroth component) vanish. Thus, the modified truncated current reads

$$
\begin{aligned}
\hat{j}^\mu - \hat{j}^0\frac{q^\mu}{q^0} &= (-e)\sqrt{x}(2E)\sin\frac{\theta}{2}\left(0,\ e^{-i\sigma\phi} + \frac{2x}{1-x}\cos^2\frac{\theta}{2}\cos\phi,\right. \\
&\qquad \left. i\sigma e^{-i\sigma\phi} + \frac{2x}{1-x}\cos^2\frac{\theta}{2}\sin\phi,\ -\frac{2x}{1-x}\cos\frac{\theta}{2}\sin\frac{\theta}{2}\right),
\end{aligned}
\tag{A.48}
$$

which has the safe vanishing limit in the $\cos\theta \to 1$ with the expected behaviour $\sim \sin(\theta/2)$. Note that the expression is safe *if* we knew the $\sin(\theta/2)$ with high accuracy, and $\cos\theta$ is not a suitable input here. Recall that we have to know $1-\cos\theta$ up to the accuracy of $10^{-17}$! Thus, we always take the set

$$
\sin\frac{\theta}{2}, \qquad\qquad \cos\frac{\theta}{2}
\tag{A.49}
$$

as the inputs of the current. This completes the treatment of the matrix element, which is now completely safe numerically.

Now comes the treatment of the photon propagator. If one may naively take the square from the expression of $p_V^\mu$ Eq. (A.46), we obtain a vanishing result. This is due the fact that we have neclected the terms of the order $O(m_e^2/E)$ in the expression. We have to go back to the original definition $p_V^\mu = k^\mu - p^\mu$ to compute

$$
\begin{aligned}
D_V(p_V^2)^{-1} &= (k-p)^2 \\
&= 2m_e^2 - 2k\cdot p \\
&= -x(2E^2)\beta\beta'(1-\cos\theta) - t_{\min}(x),
\end{aligned}
\tag{A.50}
$$



with the notation

$$
t_{\min}(x) = m_e^2\frac{(1-x)^2}{x} + O\left(\frac{m_e^4}{E}\right)
\tag{A.51}
$$

defined in App. B. Note that the relevant combination is again $1-\cos\theta$, which can be rewritten by

$$
1-\cos\theta = 2\sin^2\frac{\theta}{2},
\tag{A.52}
$$

which will be numerically safe once we adopt $\sin(\theta/2)$ as the input.

Combining the truncated current and the propagator factor, we have now a special purpose current $J^\mu$ for the $t$-channel photon exchange. The case for the positron current goes just analogously, using

$$
\begin{aligned}
k^\mu &= E(1,\ 0,\ 0,\ -\beta) \\
p^\mu &= xE(1,\ \sin\theta\cos\phi,\ \sin\theta\sin\phi,\ \cos\theta),
\end{aligned}
\tag{A.53}
$$

the helicity non-flip current reads

$$
\hat{j}^\mu = -(-e)\sqrt{x}(2E)\left(\sin\frac{\theta}{2}e^{-i\sigma\phi},\ \cos\frac{\theta}{2},\ -i\sigma\cos\frac{\theta}{2},\ -i\sigma e^{-i\sigma\phi}\right).
\tag{A.54}
$$

We obtain the similar expressions for the modified current by subracting a four-vector proportional to the photon four-momentum to make the zero-th component vanish. It can be worked out easily from the above expression.

We have discussed the helicity-conserving case so far. The helicity-flip currents are much more straight-forward to obtain, since there is no large pure gauge part. We give the expressions of the truncated currents below:

$$
\begin{aligned}
\hat{j}^\mu = (-e)\frac{m_e}{\sqrt{x}}\ &\left(-\sigma(1+x)\sin\frac{\theta}{2}e^{i\sigma\phi},\ \sigma(1-x)\cos\frac{\theta}{2},\right. \\
&\left. i(1-x)\cos\frac{\theta}{2},\ -\sigma(1-x)\sin\frac{\theta}{2}e^{i\sigma\phi}\right)
\end{aligned}
\tag{A.55}
$$

for the electron, and

$$
\begin{aligned}
\hat{j}^\mu = (-e)\frac{m_e}{\sqrt{x}}e^{i\sigma\phi}\ &\left(-\sigma(1+x)\cos\frac{\theta}{2}e^{-i\sigma\phi},\ \sigma(1-x)\sin\frac{\theta}{2},\right. \\
&\left. -i(1-x)\sin\frac{\theta}{2},\ \sigma(1-x)\cos\frac{\theta}{2}e^{-i\sigma\phi}\right)
\end{aligned}
\tag{A.56}
$$

for the positron current. Though they are proportional to the electon mass due to the helicity flip, they survive in the total cross section since the the small denominator of the $t$-channel photon propagator will become as small as $m_e^2(1-x)^2/x$.

The treatment of the $t$-channel photon is completed so far. The treatment of the collinear emission of the photon is much simpler. For the emission from the electron, we need the off-shell wavefunction of the electron after the emission of the photon:

$$U = \frac{1}{\not{q} - m_e}(e\gamma^\mu)\epsilon^*_\mu(p,\lambda)u(p,\sigma) \tag{A.57}$$

according to the HELAS Feynman rules. Again we separate the propagator factor and the matrix element to

$$\begin{aligned} U &= \frac{1}{q^2 - m_e^2}\hat{U}, \\ \hat{U} &= (\not{q} + m_e)(e\gamma^\mu)\epsilon^*_\mu(p,\lambda)u(p,\sigma). \end{aligned} \tag{A.58}$$

Here we adopt the notation similar to the photon case

$$\begin{aligned} k^\mu &= E(1,\ 0,\ 0,\ \beta), \\ p^\mu &= xE(1,\ \sin\theta\cos\phi,\ \sin\theta\sin\phi,\ \cos\theta), \\ q^\mu &= k^\mu - p^\mu. \end{aligned} \tag{A.59}$$

We give the relevant formulae for $\sigma = \pm$ separately. For $\sigma = +$,

$$\hat{U} = e\lambda\sqrt{E}\begin{bmatrix} m_e\begin{pmatrix} -\sin\theta(1+\frac{1}{2}x(1+\lambda)) \\ \frac{1}{2}xe^{i\phi}(1+\cos\theta)(1+\lambda) \end{pmatrix} \\ E\begin{pmatrix} \sin\theta(-2+x(1-\lambda)) \\ xe^{i\phi}(1-\lambda)(1-\cos\theta) \end{pmatrix} \end{bmatrix}, \tag{A.60}$$

and for $\sigma = -$,

$$\hat{U} = -e\lambda\sqrt{E}\begin{bmatrix} E\begin{pmatrix} xe^{-i\phi}(1+\lambda)(1-\cos\theta) \\ \sin\theta(2-x(1+\lambda)) \end{pmatrix} \\ m_e\begin{pmatrix} \frac{1}{2}xe^{-i\phi}(1-\lambda)(1+\cos\theta) \\ \sin\theta(1+\frac{1}{2}x(1-\lambda) \end{pmatrix} \end{bmatrix}. \tag{A.61}$$

The same is done on the positron spinor in the frame

$$\begin{aligned} k^\mu &= E(1,\ 0,\ 0,\ \beta), \\ p^\mu &= xE(1,\ \sin\theta\cos\phi,\ \sin\theta\sin\phi,\ \cos\theta), \\ q^\mu &= p^\mu - k^\mu, \end{aligned} \tag{A.62}$$

we compute the truncated spinors

$$\hat{V} = \bar{v}(k,\sigma)(e\gamma^\mu)\epsilon^*_\mu(p,\lambda)(\not{q} + m_e)\gamma^0, \tag{A.63}$$

where the last $\gamma^0$ is multiplied to be compatible with the HELAS notation which always has the negative chirality components in the first two entries.



The formulae read for $\sigma = +$,

$$\begin{aligned} \hat{V} = \ -e\lambda\sqrt{E}\ \Big[&E\left(\sin\theta(-2+x(1-\lambda)),\ -xe^{-i\phi}(1+\cos\theta)(1-\lambda)\right), \\ &m_e\left(\sin\theta(1+\frac{1}{2}x(1+\lambda)),\ \frac{x}{2}e^{-i\phi}(1-\cos\theta)(1+\lambda)\right)\Big]. \end{aligned} \tag{A.64}$$

and for $\sigma = -$,

$$\begin{aligned} \hat{V} = \ e\lambda\sqrt{E}\ \Big[&m_e\left(-\frac{x}{2}e^{i\phi}(1-\cos\theta)(1-\lambda),\ \sin\theta(1+\frac{x}{2}(1-\lambda)\right), \\ &E\left(x(1+\cos\theta)(1+\lambda)e^{i\phi},\ \sin\theta(-2+x(1+\lambda))\right)\Big]. \end{aligned} \tag{A.65}$$

The propagators should be treated separately just as in the case of the currents, and we use

$$q^2 - m_e^2 = -2xE^2\left(1 - \cos\theta + \frac{1}{2}\frac{m_e^2}{E^2}\cos\theta\right), \tag{A.66}$$

for the emission from the electron, and

$$q^2 - m_e^2 = -2xE^2\left(1 + \cos\theta - \frac{1}{2}\frac{m_e^2}{E^2}\cos\theta\right), \tag{A.67}$$

for the emission from the positron. Both have again safe expressions if we adopt the set $\cos(\theta/2)$ and $\sin(\theta/2)$ as the inputs.

## A.5 Some Simplifications

In terms of these subamplitudes, we can express complete helicity amplitudes of all processes in this paper in a compact form. Cross sections are then obtained by summing helicity amplitude squareds over all final state polarizations and by making an appropriate averaging for initial state polarizations.

For massless fermions, the summation over fermion polarization can be made very simple. In our notation, the chirality index ($\alpha$) is associated with an each fermion line and the summation over $\alpha$ is made either in each 'current' subamplitude (A.25-26) or in each bispinorial scalar product (A.32), for fixed external fermion helicities (the summation is of course absent for a current with definite chirality, as in the case of the charged current of the standard model). When all the fermion masses are neglected, the selection rule (A.10) fixes the external fermion helicities in terms of the chirality index associated with the fermion line. For instances, the bispinor current (A.26) reduces in the massless fermion limit to

$$J^\mu(\langle f_2|V|f_1\rangle) \xrightarrow{m_{f_1}=m_{f_2}=0} -\delta_{\sigma_1\sigma_2}g^{Vf_2f_1}_{\sigma_1}D_V(p_V^2)\langle f_2|_{\sigma_1}(\sigma^\mu)_{\sigma_1}|f_1\rangle_{\sigma_1}, \tag{A.68}$$

which is essentially the current employed in Ref. [16]. Therefore, in massless fermion limits, the chirality index is fixed uniquely by the external fermion helicities and the summation

over helicities can be restricted to those combinations of helicities which are consistent with the chirality selection rule along all the fermion lines.

There may appear further simplification in the massless fermion limit. Then the $V-A$ interaction of the charged current will be absent for the positive chirality fermion line. Hence many diagrams will drop for the certain helicity combinations. This fact will make the computor programs much faster.



# Appendix B

# Phase Space

Evaluation of single weak boson production and vector boson fusion cross sections in this paper requires the use of appropriate phase space variables to achieve a good numerical accuracy. We present in this appendix our choice of integration variables, which may be useful in a more general ground for processes with collinear singularities associated with colliding particles.

We treat all the single weak boson production processes

$$e^-(k_1)+e^+(k_2) \longrightarrow \begin{cases} e^-(p_1)+e^+(p_2)+X(p_X) \\ e^-(p_1)+\bar{\nu}_e(p_2)+X(p_X) \\ \nu_e(p_1)+e^+(p_2)+X(p_X) \\ \nu_e(p_1)+\bar{\nu}_e(p_2)+X(p_X) \\ \gamma(p_1)+\gamma(p_2)+X(p_X) \end{cases} \tag{B.1}$$

with a common set of kinematical variables. The state $X$ is either a single $W/Z$ state, pair of the $W/Z$ bosons or top quark, or their decay products, and hence does not necessarily have a fixed invariant mass. We paramatrize the four-momenta of the particles in the laboratory ($e^+e^-$ c.m.) frame:

$$\begin{aligned} k_1^\mu &= \frac{\sqrt{s}}{2}(1,0,0,\beta) \\ k_2^\mu &= \frac{\sqrt{s}}{2}(1,0,0,-\beta) \\ p_1^\mu &= \frac{\sqrt{s}}{2}x_1(1,\beta_1\sin\theta_1\cos\phi_1,\beta_1\sin\theta_1\sin\phi_1,\beta_1\cos\theta_1) \\ p_2^\mu &= \frac{\sqrt{s}}{2}x_2(1,\beta_2\sin\theta_2\cos\phi_2,\beta_2\sin\theta_2\sin\phi_2,\beta_2\cos\theta_2) \end{aligned} \tag{B.2}$$

with $\beta=(1-4m_e^2/s)^{1/2}$ and $\beta_i=(1-4m_i^2/sx_i^2)^{1/2}$, where $m_i$ is either $m_e$ or 0 depending on the processes in (B.1). In the following, we retain the electron mass only when its finite value affects the integrated cross sections in the $m_e^2/s\to 0$ limit.

The invariant phase space volume

$$\mathrm{d}\Phi = (2\pi)^4\delta^4(k_1+k_2-p_1-p_2-\sum_{i\epsilon X}p_i)\ \frac{\mathrm{d}^3p_1}{(2\pi)^3 2p_1^0}\ \frac{\mathrm{d}^3p_2}{(2\pi)^3 2p_2^0}\ \prod_{i\epsilon X}\frac{\mathrm{d}^3p_i}{(2\pi)^3 2p_i^0} \tag{B.3}$$

can be decomposed as

$$\mathrm{d}\Phi = \frac{\mathrm{d}^3p_1}{(2\pi)^3 2p_1^0}\ \frac{\mathrm{d}^3p_2}{(2\pi)^3 2p_2^0}\ \delta\left((k_1+k_2-p_1-p_2)^2-\hat{s}\right)\ \mathrm{d}\hat{s}\mathrm{d}\Phi_X \tag{B.4}$$

with

$$\mathrm{d}\Phi_X = (2\pi)^4\delta^4(k_1+k_2-p_1-p_2-\sum_{i\epsilon X}p_i)\ \prod_{i\epsilon X}\frac{\mathrm{d}^3p_i}{(2\pi)^3 2p_i^0} \tag{B.5}$$

The partial phase space $\mathrm{d}\Phi_X$ is simply

$$d\Phi_X = (2\pi)\ \delta(\hat{s}-m_X^2) \tag{B.6}$$

in the zero width approximation of the weak boson. When the decay

$$X(p_X) \longrightarrow f(p_3)+\bar{f}(p_4) \tag{B.7}$$

is incorporated, it is expressed most conveniently as

$$\mathrm{d}\Phi_X = \frac{1}{32\pi^2}\ \bar{\beta}\left(\frac{m_3^2}{\hat{s}},\frac{m_4^2}{\hat{s}}\right)\ \mathrm{d}\cos\hat{\theta}_3\mathrm{d}\hat{\phi}_3 \tag{B.8}$$

in the decaying $X$ rest frame with the two body phase space factor

$$\bar{\beta}(a,b) = [1-2(a+b)+(a-b)^2]^{1/2}. \tag{B.9}$$

The Breit-Wigner resonance is accounted for by a choice of variable

$$\mathrm{d}\hat{s} = \frac{(\hat{s}-m_X^2)^2+(m_X\Gamma_X)^2}{m_X\Gamma_X}\mathrm{d}\left(\tan^{-1}\frac{\hat{s}-m_X^2}{m_X\Gamma_X}\right). \tag{B.10}$$

The remaining $p_1$ and $p_2$ phase space volumes in (B.4) are parametrized in the laboratory frame (B.2) as

$$\mathrm{d}\Phi = \frac{s^2}{(4\pi)^6}\ \delta\left((k_1+k_2-p_1-p_2)^2-\hat{s}\right)x_1x_2\mathrm{d}x_1\mathrm{d}x_2\mathrm{d}\cos\theta_1\mathrm{d}\cos\theta_2\mathrm{d}\phi_1\mathrm{d}\phi_2\mathrm{d}\hat{s}\mathrm{d}\Phi_X \tag{B.11}$$

in the $m_e^2/s \to 0$ limit. Solving the delta function for $x_2$ gives

$$\mathrm{d}\Phi = \frac{s^2}{(4\pi)^6}\ \frac{x_1(1-x_1-\hat{s}/s)}{[1-x_1(1-\cos\theta_{12})/2]^2}\ \mathrm{d}x_1\mathrm{d}\cos\theta_1\mathrm{d}\cos\theta_2\mathrm{d}\phi_1\mathrm{d}\phi_2\mathrm{d}\hat{s}\mathrm{d}\Phi_X. \tag{B.12}$$



The angle $\theta_{12}$ is the opening angle between $\mathbf{p}_1$ and $\mathbf{p}_2$ in the laboratory frame (B.2) whose cosine is given below in Eq. (B.19). The collinear singularities at $\cos\theta_i = \pm 1$ are accounted for by introducing variables

$$y_i = \frac{1}{2}\log\left(\frac{1+\cos\theta_i+2\Delta_i^+}{1-\cos\theta_i+2\Delta_i^-}\right)\ \text{ for } i=1,2 \tag{B.13}$$

with a process dependent regulator $\Delta_i^{\pm}$ ;

$$\Delta_i^{\pm} = O\left(\frac{m_e^2}{s}\right) \tag{B.14}$$

for processes with a $t$-channel photon or electron propagator, and

$$\Delta_i^{\pm} = O\left(\frac{m_W^2}{s}\right) \tag{B.15}$$

when the initial $e^{\pm}$ emits a neutrino. When there appears no $t$- or $u$-channel singularity in the initial $e^{\pm}$ channel, the regulator $\Delta_i^{\pm}$ can take arbitrary positive numerical value of O(1) or larger.

The phase space volume takes its final form as

$$\mathrm{d}\Phi = \frac{s}{(4\pi)^6}\ \frac{x_1(1-x_1-\hat{s}/s)}{[1-x_1(1-\cos\theta_{12})/2]^2}\ \frac{1+\Delta_1^++\Delta_1^-}{\cosh^2 y_1}\ \frac{1+\Delta_2^++\Delta_2^-}{\cosh^2 y_2}\ \mathrm{d}x_1\mathrm{d}y_1\mathrm{d}y_2\mathrm{d}\phi_1\mathrm{d}\phi\mathrm{d}\hat{s}\mathrm{d}\Phi_X \tag{B.16}$$

with

$$\cos\theta_i = (1+\Delta_i^++\Delta_i^-)\tanh(y_i)-\Delta_i^++\Delta_i^- \quad \text{for } i=1,2, \tag{B.17}$$

$$\phi_2 = \phi_1+\phi, \tag{B.18}$$

$$\cos\theta_{12} = \cos\theta_1\cos\theta_2-\sin\theta_1\sin\theta_2\cos\phi, \tag{B.19}$$

$$x_2 = \frac{1-x_1-\hat{s}/s}{1-x_1(1-\cos\theta_{12})/2}. \tag{B.20}$$

The regulator factor $\Delta_i^{\pm}$ in Eq. (B.16) can be neglected when it is of the order of $m_e^2/s$, in accordance with our high energy approximation (B.11). The integration region is as follows:

$$(\sum_{i\epsilon X}m_i)^2 < \hat{s} < (\sqrt{s}-m_1-m_2)^2\ , \tag{B.21}$$

$$\frac{2m_1}{\sqrt{s}} < x_1 < 1+\frac{m_1^2}{s}-\frac{(\sqrt{\hat{s}}+m_2)^2}{s}\ , \tag{B.22}$$

$$-\frac{1}{2}\log\frac{1+\Delta_i^-}{\Delta_i^+} < y_i < \frac{1}{2}\log\frac{1+\Delta_i^+}{\Delta_i^-}\ \ for\ i=1,2\ , \tag{B.23}$$

$$0 < \phi_1, \phi < 2\pi. \tag{B.24}$$

The constraint

$$x_2 > \frac{2m_2}{\sqrt{s}} \tag{B.25}$$

should be imposed by hand because of the neglect of the electron mass in Eq. (B.20).

There are four comments in order. First, the numerical accuracy of the photon or electron propagator factor

$$\begin{aligned} t &= (k_1 - p_1)^2 \\ &= m_e^2 + m_1^2 - \frac{s}{2}x_1(1 - \beta\beta_1\cos\theta_1) \\ &= -\frac{s}{2}x_1\beta\beta_1(1 - \cos\theta_1) - t_{min}(x_1) \end{aligned} \tag{B.26}$$

with

$$\begin{aligned} t_{min}(x_1) &= \frac{s}{2}x_1(1 - \beta\beta_1) - m_e^2 - m_1^2 \\ &= m_e^2\left(\frac{2x_1}{1+\beta\beta_1} - 1\right) + m_1^2\left(\frac{1}{x_1}\frac{2\beta^2}{1+\beta\beta_1} - 1\right) \end{aligned} \tag{B.27}$$

requires a careful treatment in the collinear limit, $\cos\theta_1 = 1$. For instance, the minimum of the photon propagator factor in the process $e^-e^+ \to e^-e^+Z$ ($m_1 = m_e$) leads to the small ratio

$$\frac{t_{min}(x_1)}{s} = \frac{2m_e^2}{s}\left(\frac{x_1 + \beta^2/x_1}{1+\beta\beta_1} - 1\right) = \frac{m_e^2}{s}\frac{(1-x_1)^2}{x_1} + O\left(\frac{m_e^4}{s^2}\right), \tag{B.28}$$

which can become as small as $3 \times 10^{-19}$ at $\sqrt{s} = 2$ TeV for $x_1 \sim 1 - m_Z^2/s$, where the cross section is largest. A meaningful evaluation of the propagator factor (B.26) hence requires a cancellation of more than 20 digits in the difference $1 - \cos\theta_1$. For the electron propagator factor in the process $e^-e^+ \to \gamma\gamma Z$ ($m_1 = 0$), the relevant ratio is

$$\frac{t_{min}(x_1) + m_e^2}{s} = \frac{m_e^2}{s}\frac{2x_1}{1+\beta} = \frac{m_e^2}{s}x_1 + O\left(\frac{m_e^4}{s^2}\right), \tag{B.29}$$

which can also become very small for a soft photon ($x_1 << 1$). In order to avoid the huge numerical cancellation within the factor $1 \pm \cos\theta_i$ in the collinear limits ($\cos\theta_i = \mp 1$), we should evaluate these factors directly in terms of our integration variables $y_i$ as

$$\frac{1 \pm \cos\theta_i}{2} = \frac{1 + \Delta_i^+ + \Delta_i^-}{1 + \exp(\mp 2y_i)} - \Delta_i^{\pm}. \tag{B.30}$$

The above numerical factors are also used in the evaluation of the matrix elements associated with the $ee\gamma$ vertices [17].

Second, a statistical factor of 1/2! is required for two photons in the process $e^-e^+ \to \gamma\gamma Z$. We find it most convenient to restrict the phase space for kinematically distinct two photons by requiring either

$$\cos\theta_1 > \cos\theta_2 \tag{B.31}$$



or

$$x_1 > x_2. \tag{B.32}$$

The equivalence of the two results can be used to test the numerical program.

Third, we find it more efficient in the processes $e^-e^+ \to e^-e^+Z$ and $e^-e^+ \to \nu_e\bar{\nu}_eZ$ to interchange the role of $x_1$ and $x_2$ (and hence to choose $x_2$ as an integration variable) depending on the kinematics of the final lepton pair. We choose $x_1$ as an integration variable when the inequality

$$|(k_1 - p_1)^2| < |(k_2 - p_2)^2| \tag{B.33}$$

holds, and choose $x_2$ otherwise. This interchange makes the phase space volume respect manifestly the CP invariance of the processes.

Fourth, we list below for each process our optimal choice of the integration variables, $\Delta_1^{\pm}$ and $\Delta_2^{\pm}$, as well as the function $f(x_1)$ that parametrizes the $x_1$ integral

$$\mathrm{d}x_1 = \frac{1}{|f'(x_1)|}\mathrm{d}f(x_1). \tag{B.34}$$

For the process $e^-e^+ \to e^-e^+Z$, we find

$$\Delta_1^- = \frac{t_{min}(x_1)}{s} = \frac{m_e^2}{s}\frac{(1-x_1)^2}{x_1}, \tag{B.35}$$

$$\Delta_2^+ = \frac{t_{min}(x_2)}{s} = \frac{m_e^2}{s}\frac{(1-x_2)^2}{x_2}, \tag{B.36}$$

$$\Delta_1^+ = \Delta_2^- = \frac{m_e^2}{s}, \tag{B.37}$$

$$f(x_1) = \frac{1}{1-x_1}. \tag{B.38}$$

For the process $e^-e^+ \to e^-\bar{\nu}_eW^+$, a good choice is found to be

$$\Delta_1^- = \frac{t_{min}(x_1)}{s} = \frac{m_e^2}{s}\frac{(1-x_1)^2}{x_1}, \tag{B.39}$$

$$\Delta_2^+ = \frac{m_W^2}{s}, \tag{B.40}$$

$$\Delta_1^+ = \Delta_2^- = 1, \tag{B.41}$$

$$f(x_1) = \log(1-x_1). \tag{B.42}$$

Here the choice of $\Delta_1^+ = \Delta_2^- = 1$ is rather arbitrary, where any positive number in excess of unity is appropriate because of the absence of $t$- or $u$-channel singularity. The role of $x_1$ and $x_2$, and that of $\Delta_1^-$ and $\Delta_2^+$ should be interchanged for the CP conjugate process $e^-e^+ \to \nu_e e^+W^-$.

For the process $e^-e^+ \to \nu_e\bar{\nu}_e Z$, we find that the choice

$$\Delta_1^- = \Delta_2^+ = \frac{m_W^2}{s}, \tag{B.43}$$

$$\Delta_1^+ = \Delta_2^- = 1, \tag{B.44}$$

$$f(x_1) = \log(1-x_1), \tag{B.45}$$

is effective. Again, any large positive number works as well for $\Delta_1^+ = \Delta_2^-$.

Finally for the process $e^-e^+ \to \gamma\gamma Z$, we find that the choice

$$\Delta_1^- = \frac{m_e^2}{s}x_1, \tag{B.46}$$

$$\Delta_2^+ = \frac{m_e^2}{s}x_2, \tag{B.47}$$

$$\Delta_1^+ = \Delta_2^- = \frac{m_e^2}{s}, \tag{B.48}$$

$$f(x_1) = \log x_1, \tag{B.49}$$

makes an efficient integration. The integration region in this process depends on the final state cuts that we impose, since without a cut-off the integral is divergent. When the $Z$ boson energy ($E_Z$) in the Lab. frame is required to satisfy the condition

$$E_Z < E_{cut}, \tag{B.50}$$

the integration region of $x_1$ (see Eq. (B. 22)) is restricted to

$$\frac{\sqrt{s} - E_{cut} - \sqrt{E_{cut}^2 - m_Z^2}}{\sqrt{s}} < x_1 < \frac{\sqrt{s} - E_{cut} + \sqrt{E_{cut}^2 - m_Z^2}}{\sqrt{s}}. \tag{B.51}$$



# Appendix C

# Helicity Selection Rule

We explain the helicity selection rule for the collinear vector bosons emitted from the initial state fermion. We discuss the treatment of the off-shell wavefunctions first. Then we apply the technique to the relevant case.

Recall that the unitary gauge propagator of massive vector boson can be regarded as a sum over the possible intermediate state. Consider the case of the time-like momenum first. Then the unitary gauge propagator reads

$$\frac{i}{q^2 - m_V^2}\left(-g^{\mu\nu} + \frac{q^\mu q^\nu}{m_V^2}\right), \tag{C.1}$$

where $m_V$ is the mass of the vector boson and $q^\mu$ is its (timelike) four-momentum.

It is well-known that the projection operator on the transverse (in the four-dimensional sense) components can be written as a sum over the polarization vectors:

$$-g^{\mu\nu} + \frac{q^\mu q^\nu}{q^2} = \sum_{\lambda=-1}^{1} \epsilon^\mu(q,\,\lambda)\epsilon^{\nu *}(q,\,\lambda) \tag{C.2}$$

where the index $\lambda$ corresponds to the helicity. Using this decomposition, we can re-write the case of the unitarity gauge propagator similarly.

$$\begin{aligned} -g^{\mu\nu} + \frac{q^\mu q^\nu}{m_V^2} &= -g^{\mu\nu} + \frac{q^\mu q^\nu}{q^2} + \frac{q^2 - m_V^2}{m_V^2}\frac{q^\mu q^\nu}{q^2} \\ &= \sum_{\lambda=-1}^{1} \epsilon^\mu(q,\,\lambda)\epsilon^{\nu *}(q,\,\lambda) + \frac{q^2 - m_V^2}{m_V^2}\frac{q^\mu q^\nu}{q^2}, \end{aligned} \tag{C.3}$$

which leads to the observation that for off-shell massive vector boson there are *four* polarization state propagating, where one of them is the ***scalar*** polarization.

The case for the space-like four-momentum differs from the above decomposition only to add the factor $(-1)^{\lambda+1}$ to take account of the negative norm polarization vector.

We wish to have similar decomposition in the fermion case. The propagator of fermion field reads

$$\frac{i}{\not{p} - m_f} = \frac{i}{p^2 - m_f^2}(\not{p} + m_f), \tag{C.4}$$

where we wish to rewrite the last bracket as a sum over the intermediate states.

First recall that if we once fix the mass of the fermion $m_f$, the Dirac spinors are the functions of the three-momentum only, which we write

$$u(\vec{p},\ \sigma), \quad v(\vec{p},\ \sigma). \tag{C.5}$$

Here the four-momentum of the off-shell fermion is denoted as

$$p^\mu = (E,\ \vec{p}). \tag{C.6}$$

The explicit form of the spinors are defined in App. A. For later convenience, we define the on-shell energy computed from the three-momentum as

$$E_{\rm on} = \sqrt{|\vec{p}|^2 + m_f^2}, \tag{C.7}$$

where it may differ from the zero-th component of the four-momentum $E$.

From the famous technique by Casimir [14], the following identity is well-known:

$$\sum_{\sigma=\pm} u(\vec{p},\ \sigma)\bar{u}(\vec{p},\ \sigma) = \not{p}_{\rm on} + m_f = E_{\rm on}\gamma^0 - \vec{p}\cdot\vec{\gamma} + m_f, \tag{C.8}$$

$$\sum_{\sigma=\pm} v(\vec{p},\ \sigma)\bar{v}(\vec{p},\ \sigma) = \not{p}_{\rm on} - m_f = E_{\rm on}\gamma^0 - \vec{p}\cdot\vec{\gamma} - m_f, \tag{C.9}$$

for the Dirac spinors normalized as

$$\bar{u}(\vec{p},\ \sigma)u(\vec{p},\ \sigma) = -\bar{v}(\vec{p},\ \sigma)v(\vec{p},\ \sigma) = 2m_f. \tag{C.10}$$

We start from these identities to obtain the decomposition of $\not{p} + m_f$.

Now it should be trivial to obtain the identity

$$\begin{aligned}
&\frac{E+E_{\rm on}}{2E_{\rm on}}\sum_{\sigma=\pm} u(\vec{p},\ \sigma)\bar{u}(\vec{p},\ \sigma) + \frac{E-E_{\rm on}}{2E_{\rm on}}\sum_{\sigma=\pm} v(-\vec{p},\ \sigma)\bar{v}(-\vec{p},\ \sigma) \\
&= \frac{E+E_{\rm on}}{2E_{\rm on}}(E_{\rm on}\gamma^0 - \vec{p}\cdot\vec{\gamma} + m_f) + \frac{E-E_{\rm on}}{2E_{\rm on}}(E_{\rm on}\gamma^0 + \vec{p}\cdot\vec{\gamma} + m_f) \\
&= E\gamma^0 - \vec{p}\cdot\vec{\gamma} + m_f \\
&= \not{p} + m_f.
\end{aligned} \tag{C.11}$$

Thus we have obtained a very simple decomposition of the spinor propagator in terms of the intermediate states, although the decomposition is not Lorentz invariant. The lack of Lorentz invariance, however, does not cause any problems on the discussions in this appendix since we will dicuss the helicity selection rule which indeed depends on the frame.

The physical interpretation of our formula is very clear. Let us take the on-shell limit $E \to E_{\rm on}$, then the $v$-spinor part drops, recovering the identity (C.8). The other limit $E \to -E_{\rm on}$ will make the $u$-spinor part to drop giving the identity (C.9). Since the on-shell energy $E_{\rm on}$ is always positive, the $u$-spinor dominates in the formula if $E > 0$, and $v$-spinor



dominates if $E < 0$. Thus the off-shell spinor with positive energy can be regarded as *almost* fermion and with negative energy as *almost* anti-fermion.

Now we can discuss the collinear emission of a vector boson. Our strategy is to keep the electron mass only in the denominator of the propagator, however drop all the terms proportional to $m_e$ in the matrix element. Then our discussion can be universal to all vector bosons since the only difference lies in the denominator of the propagator which explicitly depends on the mass of the vector boson. What we wish to know is the difference between the helicity states of the vector bosons, and the propagator factor is common to all helicities. Thus we have to discuss the matrix element only.

From now on, we do not specify the vector boson nor the coupling constant. What we should know is the dependence on the helicity of the vector boson of the matrix element

$$\not{p}\not{\epsilon}(q,\ \lambda)u(k,\ \sigma) \tag{C.12}$$

where the propagator factor is dropped, and the mass of the electron (or neutrino) is neglected. One may wonder that the discussion will depend on the mass of the vector boson since the polarization vector has its four-momentum as the argument. However, if we concentrate on the transverse components, the dependence lies solely on the *space* momentum $\vec{q}$. So we can keep the universal character of our discussion. The dependence of the factor $\not{p}$ on the mass of the vector boson will be irrelevant as well, as shown in the followings.

The four-momenta are written down in the laboratory frame:

$$k = E(1,\ 0,\ 0,\ 1), \tag{C.13}$$

$$q = xE(1,\ \beta_V \sin\theta,\ 0,\ \beta_V\cos\theta), \tag{C.14}$$

$$p = E(1-x,\ -x\beta_V\sin\theta,\ 0,\ 1-x\beta_V\cos\theta). \tag{C.15}$$

Now we decompose the factor $\not{p}$ as the sum over the intermediate states

$$\not{p} = \sum_{\sigma'=\pm}\left(\frac{p^0+|\vec{p}|}{2|\vec{p}|}u(\vec{p},\ \sigma')\bar{u}(\vec{p},\ \sigma') + \frac{p^0-|\vec{p}|}{2|\vec{p}|}v(-\vec{p},\ \sigma')\bar{v}(-\vec{p},\ \sigma')\right), \tag{C.16}$$

where $|\vec{p}|$ corresponds to $E_{\rm on}$ in our formula eq. (C.11). Since we have neglected $m_e$, the chirality is conserved, and the wrong chirality helicity will drop from the above sum, giving

$$\begin{aligned}
&\not{p}\not{\epsilon}(q,\ \lambda)u(k,\ \sigma) \\
&= \left(\frac{p^0+|\vec{p}|}{2|\vec{p}|}u(\vec{p},\ \sigma)\bar{u}(\vec{p},\ \sigma) + \frac{p^0-|\vec{p}|}{2|\vec{p}|}v(-\vec{p},\ -\sigma)\bar{v}(-\vec{p},\ -\sigma)\right)\gamma_\mu\epsilon^\mu(q,\ \lambda)u(k,\ \sigma)
\end{aligned} \tag{C.17}$$

The dependence on the helicity of the vector boson is confined to the matrix elements

$$\bar{u}(\vec{p},\ \sigma)\not{\epsilon}(q,\ \lambda)u(k,\ \sigma), \tag{C.18}$$

and

$$\bar{v}(-\vec{p},\ -\sigma)\not{\epsilon}(q,\ \lambda)u(k,\ \sigma). \tag{C.19}$$

Thus we are lead to discuss the above matrix elements only, and see which $\lambda$ is dominating in the collinear region. Now we fix the helicity of the initial electron to be positive:

$$\sigma = + \tag{C.20}$$

without loosing the generality of the discussion. After straight-forward computation, we obtain

$$\bar{u}(\vec{p},\ +)\ \not{\varepsilon}(q,\ \lambda)u(k,\ +) = \frac{E}{\sqrt{2|\vec{p}|(|\vec{p}|+p_z)}}(-\sin\theta)[\sqrt{1-2x\cos\theta+x^2}+(1+\lambda x)], \tag{C.21}$$

and

$$\bar{v}(-\vec{p},\ -)\ \not{\varepsilon}(q,\ \lambda)u(k,\ +) = \frac{E}{\sqrt{2|\vec{p}|(|\vec{p}|-p_z)}}(-\sin\theta)[\sqrt{1-2x\cos\theta+x^2}-(1+\lambda x)]. \tag{C.22}$$

Note the factor $\sin\theta$ due to the angular momentum conservation.

Now we know the dependence on the helicity of the vector boson. If the vector boson is emitted soft ($x \sim 0$), then the dependence on the helicity drops due to the combination $\lambda x$. Thus there appears no selection rule if the vector boson is emitted softly, as in the case of the soft photon radiation. However, if the vector boson is emitted hard ($x \sim 1$), then the factor

$$\sqrt{1-2x\cos\theta+x^2} \sim |1-x| + \frac{x}{|1-x|}(1-\cos\theta) \tag{C.23}$$

in the collinear limit is small ($\sim |1-x|$), while the terms

$$1+\lambda x \tag{C.24}$$

will remain large *if* $\lambda = 1$. Thus the energetic vector boson emitted from the $\sigma = +$ electron favours $\lambda = +$, hence has the same sign helicity as the initial state electron has. This proves the helicity selection rule of the hard vector boson emission from the initial state. Since the massive vector boson favour to be energectic from the discussion in Chap. 6, the selection rule is very clear for the $W$- and $Z$-bosons.

We did not discuss the case of the massive vector boson with longitudinal polarization. We do not know how to discuss in a universal way to treat the longitudinal component, since it requires cancellation among the diagrams to satisfy the BRS identity (see Chap. 2). The only statement we can show here is that the longitudinal components do not seem to be favoured in collinear emission processes, however we do not know the reason at present.



# Bibliography


[1] Proceedings of the Workshop on Physics at Future Accelerators, CERN Yellow Report 87-07 (1987) Vol. I and II.

[2] C. Ahn et al., "Opportunities and Requirements for Experimentaion at a Very High Energy $e^+e^-$ Collider", SLAC Report SLAC-0329 (1988).

[3] Proceedings of the First Workshop on Japan Linear Collider (JLC), KEK, Oct. 24-25, 1989, KEK Report 90-2 (1990).

[4] Proceedings of the Second Workshop on Japan Linear Collider (JLC), KEK, Nov. 6–8, 1990, to appear in KEK Report (1991).

[5] T. Kinoshita *ed*, "Quantum Electrodynamics", World Scientific, Singapore, 1990.

[6] A. Sirlin, talk at the fifth Nishinomiya Yukawa Memorial Symposium, Nishinomiya, Oct., 1990.

[7] W. Marciano, G. Valencia and S. S. D. Willenbrock, Phys. Rev. F**40**, 1725 (1989).

[8] M. Drees, Int. J. Mod. Phys. A**4**, 3635 (1989).

[9] Y. Nambu and G. Jona-Lasinio, Phys. Rev. **122**, 345 (1961).

[10] Susskind and Farhi, Phys. Rep. **74**, 277 (1981).

[11] F. Abe *et al.*, ANL-HEP-PR-90-71, Aug., 1990.

[12] G. 't Hooft, Proceedings of Cargèse summer Institute 1975, p. 135.

[13] M. Claudson, E. Farhi and R. L. Jaffe, Phys. Rev. D**34**, 873 (1986).

[14] H B. G. Casimir, Helv. Phys. Acta **6**, 287 (1933).

[15] K. Hagiwara and D. Zeppenfeld, Nucl. Phys. **B274**, 1 (1986).

[16] K. Hagiwara and D. Zeppenfeld, Nucl. Phys. **B313**, 560 (1989).

[17] H. Murayama, I. Watanabe and K. Hagiwara, "HELAS: HELicity Amplitude Subroutines for Feymman diagram evaluations", to appear in KEK-Report.

[18] G.J. Gounaris, R. Kögerler and H. Neufeld, Phys. Rev. **D34**, 3257 (1986).

[19] C. Becchi, A. Rouet and B. Stora, Comm. Math. Phys. **42**, 127 (1975); Ann. Phys. **98**, 287 (1976)

[20] G.V. Borisov, V.N. Larin and F.F. Tikhonin, Z. Phys. **C41**, 287 (1988).

[21] S. Kawabata, Comp. Phys. Comm. **41**, 127 (1986).

[22] F. Iddir *et al.*, Phys. Rev. D**41**, 22 (1990).

[23] K. Hikasa, private communication.

[24] M. Böhm and T. Sack, Z. Phys. C**35**, 119 (1987).

[25] V. S. Fadin and V. A. Khoze, JETP Lett., **46**, 525 (1987); Sov. J. Phys. **48**, 309 (1988).

[26] M. J. Strassler and M. E. Peskin, SLAC-PUB-5308, Sept., 1990.

[27] K. Fujii, Y. Sumino., K. Hagiwara, H. Murayama and I. Watanabe, in preparation.

[28] K. Hagiwara, A. Miyamoto, H. Murayama and H. Iwasaki, in preparation.

[29] P. Salati and J. C. Wallet, Z. Phys. **C16**, 155 (1982);
O. Cheyette, Phys. Lett. **137B**, 431 (1984);
A.N. Kamal, J.N.Ng and H.C. Lee, Phys. Rev. **D24**, 2842 (1981);
A. Grau and J.A. Grifols, Nucl. Phys. **B233**, 375 (1984);
G. Altarelli, G. Martinelli, B. Mele and R. Rückl, Nucl. Phys. **B262**, 204 (1985);
E. Gabrielli, Mod. Phys. Lett. **A1**, 465 (1986);
M. Böhm and A. Rosado, Z. Phys. **C39**, 275 (1988); ibid. **C42**, 479 (1989);
U. Baur and D. Zeppenfeld, Nucl. Phys. **B325**, 253 (1989);
E. Yehudai, Phys. Rev. **D41**, 33 (1990).

[30] E. Gabrielli, Proceedings of the Workshop on Physics at Future Accelerators, CERN Yellow Report 87-07, Vol. II, p1 (1987).

[31] K. Hagiwara, H. Iwasaki, A. Miyamoto, H. Murayama and D. Zeppenfeld, UT-574, Dec., 1990.

[32] Yu. L. Dokshitzer, V. A. Khoze, A. H. Müller and S. I. Troyan, Rev. Mod. Phys., **60**, 373 (1988).

[33] E. Yehudai, Phys. Rev. **D42**, 771 (1990).

[34] P. R. Burchat, D. L. Burke and A. Petersen, Phys. Rev. **D38**, 2735 (1988).

[35] B.W. Lee, C. Quigg and H.B. Thacker, Phys. Rev. **D16**, 1519 (1977);



[36] V. Barger, T. Han and R. J. N. Phillips Phys. Rev. D**39**, 146 (1989).

[37] S. S. D. Willenbrock, Ann. Phys. **186**, 15 (1988).

[38] J. F. Gunion and A. Tofighi-Niaki, Phys. Rev. D**36**, 2671 (1987).

[39] H. Baer, K. Hagiwara and X. Tata, Phys. Rev. **D35**, 1598 (1987).

[40] K. Hagiwara, R.D. Peccei, D. Zeppenfeld and K. Hikasa, Nucl. Phys. **B282**, 253 (1987).

[41] M. Kobayashi and T. Maskawa, Prog. Theor. Phys. **49**, 652 (1973).

[42] K. Hagiwara, H. Iwasaki, H. Murayama and I. Watanabe, in preparation.